DESIGN AND DEVELOPMENT OF A PIEZOELECTRIC LINEAR ACTUATOR FOR SMART STRUCTURES

Jian Li

A Thesis

in

The Department

of

Mechanical and Industrial Engineering

Presented in Partial Fulfillment of the Requirements

for the Degree of Master of Applied Science at

Concordia University

Montreal, Quebec, Canada

May 2004

Your file Votre référence
ISBN: 0-612-94729-7
Our file Notre référence
ISBN: 0-612-94729-7

ABSTRACT

Design And Development Of A Piezoelectric Linear Actuator For Smart Structures

Jian Li

The objective of this research is to present a proof-of-concept design of an inchworm-type piezoelectric actuator with output of maximum displacement and force (or power) for shape control and vibration control of adaptive truss structures. The proposed inchworm actuator adopts "pusher" type with frictional clamping mechanisms and similar to most inchworm-type actuators it consists of three main components: two clamping or braking devices and expanding device. The central expanding device consists of a longitudinal PZT stack and a thin wall tube to provide extension-contraction motion and output force. The clamping device consists of the same tubular type PZT stack, a compliant mechanism to amplify the displacement of PZT stack, and a pre-load mechanism. The compliant mechanism consists of three flexure clamps with flexible hinges, two support rings with adjustable screws and two cover wafers, which integrate all three flexure clamps into a compliant frame. The two frictional clamping devices provide alternating braking forces when the moving shaft, which is pushed by expanding device, walks inside the PZT tubular stack and emulates an inchworm, summing small steps to achieve large displacements. Since the development of a robust clamping mechanism is essential to realize the high force capability, a considerable design effort has been focused on optimizing the clamping device to increase the output force. CATIA is used as a platform to model the whole actuator and ANSYS is used to analyze and optimize the performance of the actuator. The proposed design avoids the tight tolerance of the tube diameters, which most tubular inchworm-type actuators are required, since the moving shaft automatically keeps alignment with the central axis by six identical flexure clamps. Special design on support rings with the adjustment device and careful adjustment makes less clearance requirement between clamps and the moving shaft. The moving shaft of the actuator could also be replaced by one member of the truss structures for vibration suppression and position control purposes. In the proposed actuator the flexure clamps can also be easily replaced to outfit different dynamic characteristics. The

complete design of the proposed actuator has been performed using the finite element analysis. The simulation result confirms that the output force of 74 Newton and incremental displacement in each step of 8 micron can be achieved using the proposed actuator. A prototype of actuator has been fabricated and static tests have been performed to validate the simulation results.

ACKNOWLEDGMENTS

I would like first to thank my research supervisors, Dr. Ramin Sedaghati, and Dr. Javad Dargahi for their guidance, understanding, and encouragements throughout this work.

I would also like to thank the colleagues, faculty and staff of CONCAVE Research Center and Machine shop of Mechanical Engineering Department, for their contributions to this study.

I am grateful to the team of Sensor Technology Ltd, in particular, Dr. David Waechter for their cooperation in the PZT stacks fabrication and tests.

I am deeply thankful to my family in P.R. China, particularly, my beloved mother and I send a ray of love and blessing to my father who pasted away five months ago. I dedicate this thesis to my father for memory.

Finally, I wish to express my heartfelt thank to my wife and my daughter for their love, support and encouragement without which I would not have been able to complete this thesis.

TABLE OF CONTENTS

LIST OF FIGURES

LIST OF TABLES

LIST OF SYMBOLS

$[\,]$	matrix
$[\,]^{-1}$	inverse matrix
$[\,]^{t}$	transpose matrix
$\{\,\}$	vector
$\{\,\}^{t}$	vector transposed
μ	friction coefficient between clamps and shaft
ε	permittivity of the medium (IEEE std)
ε_o	permittivity of vacuum $8.854 * 10^{-12}$ F/m (IEEE std)
δ_o	displacement of PZT stack with zero load when applied voltage
δ_{offset}	zero points offset of PZT stack with constant force
δ_s	displacement of PZT stack with spring load when applied volage
σ_a	von Misses amplitude stress
σ_{a0}	effective von Misses amplitude stress at zero mean stress
σ_m	von Misses mean stress
A	cross section area of PZT stack
AA	arm angle of clamp
AL	arm length of clamp
AT	arm thickness of clamp
c	elastic stiffness
C	Capacitance
CF	clamping force of compliant mechanism
CL	clearance between clamp contact area and the shaft
d	piezoelectric charge constant (IEEE std)

d.a.	displacement amplification factor
D	electric displacement (charge Q per unit area) (IEEE std)
e	piezoelectric constant (IEEE std)
E	electric field strength (IEEE std)
ETOT	Total potential energy in the elements of clamp when it is deflecting
F_b	blocked force of PZT stack
F_{eff}	the effective force a PZT stack can generate
F_p	Pre-load force
g	piezoelectric voltage constant (IEEE std)
hp	thickness of piezoelectric material
HF	holding force of clamping device at – 200 V (HF = CF* μ)
k	electromechanical coupling coefficient (IEEE std)
K	relative dielectric constant
K_e	stiffness of extension tube
K_p	PZT stack stiffness
K_s	pre-load spring system stiffness
K_x	output stiffness of half-clamp (K_x = NormalF0/ range)
K_{xc}	output stiffness of compliant mechanism (K_{xc} =6 K_x)
K_y	input stiffness of half-clamp
K_{yc}	axial stiffness of compliant mechanism (K_{yc}=3/2 K_y)
K_{yfix}	Input stiffness of half-clamp when contact area is fixed
K_{yfree}	Input stiffness of half-clamp when contact area is free
K_w	stiffness of spring washers set
L	length of PZT stack
M	mass

n	number of layers of PZT stack
$N_{s.f.}$	safety factor
ND	notch diameter of clamp
NormalF0	normal force acting on the shaft (clamping force)
NT	notch thickness of clamp
OF	output force of inchworm actuator (OF = HF/2)
PF	the maximum input pressure force of compliant mechanism
R	stress ratio
Range	free displacement of the contact area in the x direction
s	mechanical compliance (IEEE std)
S	mechanical strain (IEEE std)
S_e	component endurance limit
S_{ut}	ultimate tensile stress
SMAXFIX	Maximum stress on the clamp when contact area fixed
SMAXFREE	Maximum stress on the clamp when contact area is free
t_c	layer thickness of PZT stack
T	mechanical stress (IEEE std)
V	applied voltage
Y	elasticity modulus (IEEE std)

Subscripts

i , j	i = 1 ~ 3 , j = 1 ~ 3 element index of matrix associated with directions

Superscripts

D	constant charge density elasticity measurement (open circuit)
E	constant electric field strength elasticity measurement (short circuit)
S	constant strain dielectric measurement (mechanically clamped)
T	constant stress dielectric measurement (mechanically free)

CHAPTER 1 INTRODUCTION

1.1 Introduction

The high performance requirements of advanced future space systems have motivated a new approach to structural concept, namely, adaptive structures. Among many kinds of adaptive structures, adaptive variable geometry truss structure attracts many research and applications such as vibration suppression [1, 2], shape control [3] or dimensional stability [4] and in-space assembly or deployment[5]. An adaptive truss structure can be formed through the use of active members, which include actuators and sensors [6]. Since the performance of active members will decide the feasibility of adaptive structure, design and fabrication of better active members will continuously be part of the focus in adaptive structure's research. There are many types of actuators , which can be embedded, in adaptive structures. Among them, inchworm-type actuator is attractive due to its large displacement, high resolution and accurately position maintaining ability. Since the 1980s with the development of smart materials and solid-state actuators, especially piezoelectric actuators, the actuators will be more compact, more powerful, and quicker responses. In the next sections, after introducing some basic concepts and background, the scope of research and objective of thesis based on literature survey of inchworm actuators have been provided. The approach and contribution of thesis are also presented.

1.2 Adaptive structures and actuators

Structures, which are able to sense, respond, and control their own characteristics and states by using sensors, actuators and controllers are termed adaptive structures or smart structures or intelligent structures. In adaptive structures, the sensors monitor the state of the structure constantly, and the actuators act according to the judgment and commands of

controller when environment changes in order to keep the structure in the best or desired conditions. These new structures can be applied to vibration suppression, shape control, noise attenuation, damage monitoring and many other fields[7].

Since the actuators play a critical role in adaptive structure technology and, in many cases, they constitute the limiting factor, design and improvement of actuators have recently attracted many researchers in the adaptive structure's community. An actuator is defined as the transducers capable of transferring an input energy into a mechanical output energy (displacement / force). The actuators are mainly used as positioners, which can adjust positions, or motors which can drive objects dynamically, or dampers which can suppress vibrations. Conventionally, the actuators were typically driven by air pressure, oil pressure, or electricity. To miniaturize the actuator size, electrically-controlled types are preferred in general. The displacement and generative force characteristics of conventional actuators from a viewpoint of micro-controlled types are summarized in Table 1.1 [8]. For convenience, the specifications of piezoelectric actuators, which will be introduced later in detail, are also included in the table.

Because of the structural complexity, as well as the size and weight of conventional actuator, it is rather difficult to produce an actuator with sufficient energy efficiency by using conventional methods. As a result, the applications of adaptive structure had been limited. The adaptive structure methods had not taken a breakthrough until the 1980s when smart materials became widely available and offered completely new possibilities. Compared with classical structural materials, which are entirely described by their elastic constants relating stress and strain, and their thermal expansion coefficient relating the strain to the temperature, smart materials are materials where strain can also be generated by different mechanisms involving temperature, electric field or magnetic field etc as a result of some coupling in their constitutive equations[9].

Table 1.1 Displacement characteristics of conventional actuators [8]

Drive Source	Name	Displacement Range	Displacement Accuracy	Generative Force	Response Speed
Air Pressure	Air pressure motor	Rotation	—	5 kgm	10 sec
	Air pressure cylinder	100 mm	100 μm	10^{-2} kg /mm^2	10 sec
Oil pressure	Oil pressure motor	Rotation	—	10 kgm	1 sec
	Oil pressure cylinder	1000 mm	10 μm	10 kg/mm^2	1 sec
Electricity	AC Servo motor	Rotation	—	3 kgm	100 msec
	DC Servo motor	Rotation	—	20 kgm	10 msec
	Step Motor	1000 mm	10 μm	30 kg	100 msec
	Voice Coil Motor	1 mm	0.1 μm	30 kg	1 msec
	Peizoelectric actuator	0.1 mm	0.01 μm	3 kg/mm^2	0.1 m sec

With the appearance and the development of smart materials, which will be introduced in Chapter 2, many kinds of solid-state actuators have been developed. Among these solid-state actuators, piezoelectric actuators have been highly accepted. The discussion of actuator systems and the criteria for comparing the potential offered by the various options can be reduced to two principal technical points: the conversion efficiency with which energy from the reservoir can be converted into useful mechanical energy and the mechanical impedance matching versatility offered by the actuator technology. Piezoelectric actuators function similar to a capacitance, which consumes small electric power. Moreover the solid-state piezoceramic combined with different mechanical design features which can easily

achieve desired mechanical impedance. Considering this, the piezoelectric actuator has apparent advantages on both of aforementioned technical aspects.

Fig 1.1 shows the design classification of piezoceramic actuators. Simple devices can directly use the strain induced in a ceramic longitudinally or transversely in the applied electric field strength. A simple disc and a multiplayer type belong to the former, and a cylinder (simple cylinder, separate cylinder, honeycomb) type belongs to the later. Complex devices do not use the induced strain directly, but use the magnified displacement through a spatial magnification mechanism (unimorph, bimorph, moonie, hinge lever) or through a time- accumulation mechanism (inchworm).

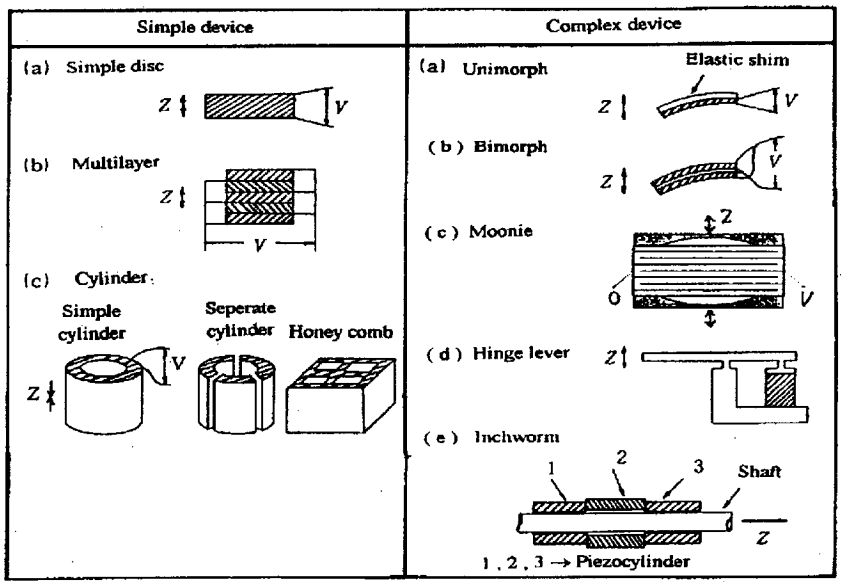

Figure 1.1 Structure of piezoceramic actuators [8]

Among all the above mentioned solid state actuators, only the inchworm-type actuator can produce both large displacement from 1mm to 600mm by accumulating small steps with respect to time and high resolution per step from 0.1μm to 10μm by controlling the applied voltages or currents while maintaining the relative large output force. Therefore, the inchworm-type actuator is very attractive in design and development of adaptive variable

geometry truss structures for both position and vibration control. The reported studies and patents relevant to inchworm-type actuators are reviewed in the next section in order to appreciate the state of the art in this field and to formulate the scope of this research dissertation.

1.3 Summary of inchworm-type actuator techniques

In order to fully understand all kinds of inchworm-type actuators introduced in the literature survey in the next section, the summary of inchworm-type actuator techniques will be presented first.

Two types of linear piezoelectric actuators with long strokes namely the piezoelectric ultrasonic motor [10] and the quasi-static inchworm are the most common linear actuators used in smart structures.. The piezoelectric ultrasonic motor uses inverse piezoelectric effect to excite two orthogonal vibration modes of an oscillator with high frequency, so that the surface points of the oscillator perform an elliptical motion[11]. By pressing the oscillator against a slider, frictional forces between the oscillator and the slider occur, and the oscillator drives the slider quickly[12, 13]. Since ultrasonic motors have high moving speed but low output forces, the quasi-static inchworm actuators will be the main concern due to their relatively high force, high displacement and high energy density.

The inchworm technique is based on the simple concept of incrementally summing the relatively small displacements produced by piezoelectric elements to generate large displacements. A typical inchworm-type linear motor has three major components: two clamping devices and one extending device. Generally there are three kinds of inchworm-type actuators[14]. The first can be referred to as a "walker" configuration, in which both extending device and clamping devices move with a shaft along the desired path of the actuation. The second basic configuration can be called the "pusher", in which the extending

and clamping devices remain stationary while the shaft appears to be pushed along the path of actuation. The third is so-called hybrid "walker-pusher", in which either the extending device or clamping devices moves along the path of actuation while the other device remains stationary.

By using piezoelectric elements or magnetostrictive elements into the clamping mechanism and the extensional mechanism, the high versatility of the inchworm design can be achieved. Although magnetostrictive material can produce larger displacement than piezoelectric material, however they require driving coils, which normally reduce the energy efficiency and cause magnetic fields, which may affect the electric control circuits. Considering this in following survey , much attention has been paid on piezoelectric elements used in clamping and extensional devices.

The extensional mechanism and clamping mechanism can be classified as direct motion and amplified motion. As piezoelectric material can only produce very small strain (<0.02%), the PZT stack actuators that consist of many thin PZT wafers glued together were often utilized in direct motion, which can produce large force (1000N ~30000N) but still low displacement. Such low displacement of direct motion produced by piezoelectric elements will require very tight manufacturing tolerances and thus not suitable on the basis of manufacturability and cost effectiveness. In contrast, amplified motion, which uses mechanical linkage by using flexure hinge or compliant mechanism, amplifies the small displacement produced by PZT stack. This compliant mechanism (amplifier) enlarges the displacement induced by PZT stack driver however it reduces the output force of PZT stack and the stiffness of extension or clamping devices.

For clamping system, there are basically two types of actuations. One is called gripping, in which the clamps grip the shaft or the guide track when the voltage is applied on PZT stacks. Another is called releasing, in which the clamps release the shaft or the guide

track when voltage is acted. The advantage of releasing type clamping device is that the clamps can grip the shaft or track under the preload spring force when the power is off. For gripping principle, there are also two different features. The most common one is the frictional clamp, in which the push force induced by the PZT stacks is transferred to the output through the friction generated between the stationary parts and the moving parts. Thus, in order to increase the output force, normal forces and friction coefficients between the clamps and housing should be increased. Another gripping feature is non-frictional clamp including ratchet and microrige, in which the ratchet will transmit loads between the clamps and the housing and output force can be increased significantly.

1.4 State of the arts regarding the piezoelectric inchworm actuators

Since the sixties of the last century, there were many research and patents concerning inchworm actuator, however the research has been trending toward two directions: one is up-sizing in space structures, precision machine tools, which involves large output force and long stroke; another is down-sizing in MEMS [15]and piezoelectric ultrasonic motor[16]. Since our main interest is in large space truss structures, the literature survey was naturally limited to the meso-scale or large-scale, high displacement and high output force inchworm actuator driven by smart material especially by piezoelectric element.

Stibitz [17] perhaps is the first one to design an actuator by using inchworm principle. The design, presented in 1964, used three stationary frictional segments for extending and clamping by pushing a shaft. Although the actuator employed magnetic field to produce clamping and cumulative linear motions in micro- inch range, it was a valuable exploration that paved the way for the next generation of the inchworm actuators. Hsu et al.[18] introduced the first patented piezoceramic inchworm in 1966. Locher [19] designed a hybrid "walker-pusher" piezoelectric inchworm with an accuracy of 13 microns in 1967 and Brisbane [20]

developed the first example of a piezoelectric "walker" motor with an increment step size down to 5 microns in 1968. The inchworm presented by Galutva [21] in 1972 was the first to use the stacked piezoelectric actuator to increase the actuation length. The piezoelectric stacked elements were used both to create the forward motion and to directly clamp the walls of the guide channel.

The most important and the first "pusher" type piezoelectric inchworm design was introduced by Bizzigotti [22] and May [23] in 1975. The commercial products produced by Burleigh Instruments[24] based on these patents lasted over 30 years. The term "Inchworm" was firstly used to describe their incremental linear motors. The first piezoelectric inchworm by using releasing type clamping device was presented by O'Neill and Foster [25] in 1980. This "walker" type inchworm actuator used two clamping disks coupled with two slotted cups that pushed against the outer cylinder when zero voltage was applied. When the disks were actuated, the cups released from the cylinder walls and the piezoelectric stack extended. Fujimoto [26] presented a "walker" type piezoelectric motor in 1988. The most important idea in this design was using structural flexures to create its clamping mechanisms. The amplified displacement allowed more flexibility of the machining tolerances.

Takahara et al.[27] developed a "pusher" type piezoelectric inchworm actuator for adaptive truss structures in 1989, which had two gripping type clamping parts with flexible hinge mechanisms and one extending device. One clamping part is constructed with three clamp arms, three piezoelectric stacks and one clamping part base. The extending device located in the middle and consisted of two piezoelectric stacks and a center flange. Although the displacement of clamp arm end could be amplified 10 times, the arm clamping force could be reduced 10 times with respect to piezoelectric driving force. Sekine et al.[28] developed another "walker" type piezoelectric inchworm actuator for the adaptive control of flexible truss structures in 1990. The actuator had two functional modes: shape adjustment

mode and vibration control mode. The actuator was composed of two clamping mechanisms, one linear- driving mechanism, an outer cylinder, pre-load mechanisms and an eddy-current proximity sensor. When there is no input voltage applied to the piezoelectric stacks, the eight grips are activated by the pre-load mechanisms and clamp the outer cylinder. The actuator has proved to function well under the shape adjustment mode, however due to the limited output force produced by the friction forces of grip levers and the nonlinear activation generated by the complexity of mechanisms at high frequencies, the actuator did not perform satisfactory under the vibration control mode and the vibration suppression were restricted to 200N and 20 Hz. Shibuta et al. [29] presented another piezoelectric actuator in 1992, which was a kind of piezoelectric stack pusher, to increase the abilities of vibration suppression.

Some other researchers presented several inchworm actuators by using flexure structures and pre-loaded devices to amplify displacements of piezoelectric stacks and to protect piezoelectric stacks from bending or shearing stress during the operation, such as Zhang and Zhu [30] in 1994, Henderson and fasick[31], Newton et al. [32] in 1998, Galante et al. [33], Canfield et al. [34], Roberts[35] in 1999 and Kim et al.[36] in 2002. Although flexure structures amplifies the displacements of clamping and extending devices, the generated output force reduces if the frictional type clamping devices are used. In order to increase the normal force produced by clamping mechanisms, some configurations that utilize direct motion of piezoelectric stacks have been presented by different researchers such as Frank et al. [37] in 1999 and Vaughan [38] in 2001.

Most of piezoelectric inchworm actuators are using frictional clamp to produce output force that relies on normal forces and friction coefficient to transmit loads between the moving part and the stationary parts. Therefore, the force output of inchworm actuators, whose range is between 3 Newtons to 200 Newtons are very limited because of the inadequate clamping mechanisms, even the PZT stack can produce as large as 3,000 to

10,000 Newtons. In order to overcome this inherent problem, some researchers explored other clamping mechanism instead of frictional clamping in order to transfer the force produced by PZT stacks efficiently. Murata [39] presented a "pusher" type piezoelectric inchworm motor in 1990, which used a linear gear rack with extremely small pitch to push a shaft. Although the method proved to be ineffective, it was still a major study. Lee and Esashi[40] proposed a small inchworm in 1995, which was only 15 mm in length. The design used micro-scaled etching techniques of silicon wafer material to create an electrostatic linear actuator, but the force output was still too small which was only in millinewton range. Carman et al.[41] presented inchworm-type actuator called Mesoscale Actuator Device, which is based on the typical inchworm-type motor with the exception that mechanical locking MEMS ridges were used to replace the traditional frictional clamping mechanisms. Park et al.[42] improved the design using the same MEMS ridges concept presented by Carman in 2001. The static result was satisfactory showing that the device could push a 450 N at low frequency, but this is proved to be not the case in the dynamic loading test in which the actuator could generate only 10 N.

1.5 Summary of the literature review

For convenience, Table 1.2 summarizes the performances of typical inchworm actuators mentioned above. The values of velocity would depend on the input frequencies. The holding forces are the maximum static forces that the actuators could resist before any slippage can occur. The linear driving force is the dynamic driving force available for moving a load as the motor or shaft moves along its guide rail. The linear driving forces would reduce steeply when working frequencies increase.

It can be seen from Table 1.2 that the actuator presented by Park et al.[42] has the maximum holding force of 450 N and no slippage since the MEMS ridges have been

employed in the clamping system. Although its dynamic characteristics were not as good as its static ones and the stroke was less then 6 mm due to its structure, it is still a promising inchworm actuator. The different components of this actuator have been shown in Figure 1.2.

Table 1.2 Comparison of different inchworm actuator performance parameters

Designer	Velocity without load (mm/s)	Holding force (N)	Linear driving force (N)	Frequency range (Hz)	Supply voltage (Volt)	Year	Type
Hsu[18]	6.3 – 38			60 - 400		1966	Hybrid
Brisbane[20]	50					1968	Walker
Burleigh[24]	2		15		1000	1975	Pusher
Takahara[27]	0.29		9.3	33	100	1989	Pusher
Sekine [28]	1.3	200	100	0 - 100	100	1990	Walker
Newton[32]	0.22	50	2.5	0 - 500	400	1997	Pusher
Zheng [30]	1.6		200			1997	Walker
Galante [33]	6	200	40	0 - 1000	124	1999	Hybrid
Roberts[35]	0.073	45	22	4.5	100	1999	Walker
Frank[37]	1	350	130	0-150	124	1999	Pusher
Park[42]	0.33	450	10	0- 30	200	2000	Pusher
Vaughan[38]	5	170	90	50	130	2001	Walker
Kim[36]	0.925		9	20	130	2002	Pusher

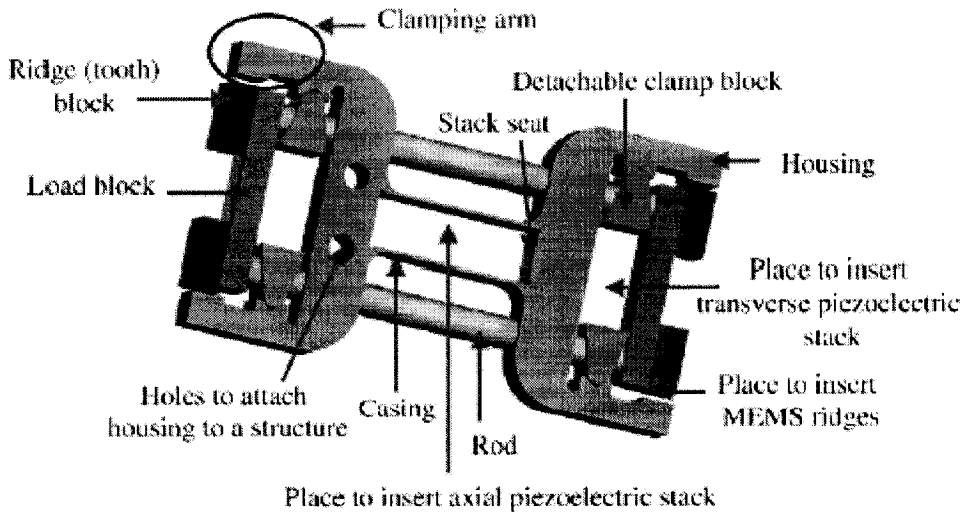

Figure 1.2 Inchworm actuator proposed by Park et al. (2001) [42]

The actuator proposed by Zheng and Zhu[30] shown in Figure 1.3 has the largest driving force of 200 N, which makes it suitable for many vibration suppression applications. The value of claimed driving force is probably from the theoretic result since the errors induced by dimensional accuracy of clamps and guideway caused some problems. The proposed elastic single piece flexure frame design is valuable however the tight tolerance of the wall and the flexure frame mechanism are very difficult to achieve.

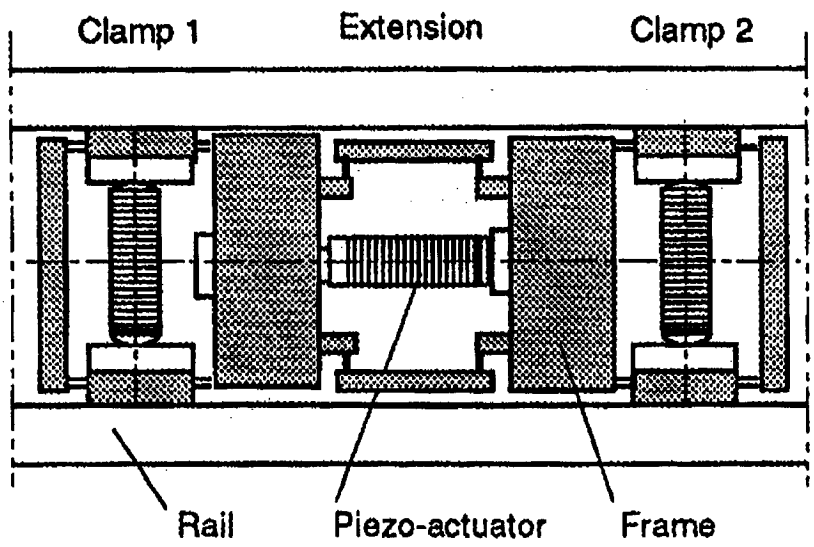

Figure 1.3 Inchworm actuator proposed by Zhang and Zhu (1994) [30]

Examination of Table 1.2 reveals that inchworm actuator presented by Frank et al.[37] shown in Figure 1.4 is superior based on the static and dynamic characteristics. However since it utilizes piezoceramic stacks directly to clamp a shaft, any clearance between the clamp and the shaft will result in a significant loss of potential clamping force. The same problem has also been observed in the actuator proposed by Vaughan [38]

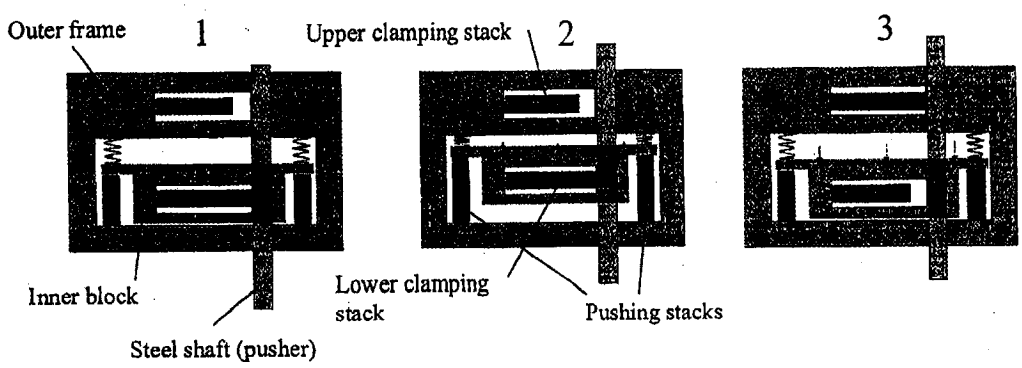

Figure 1.4 Inchworm actuator proposed by Frank et al. (1999) [37]

In comparison the design proposed by Galante et al.[33] has been found to be more practical although its linear driving force was lower than that of Frank[37] and Zheng[30].

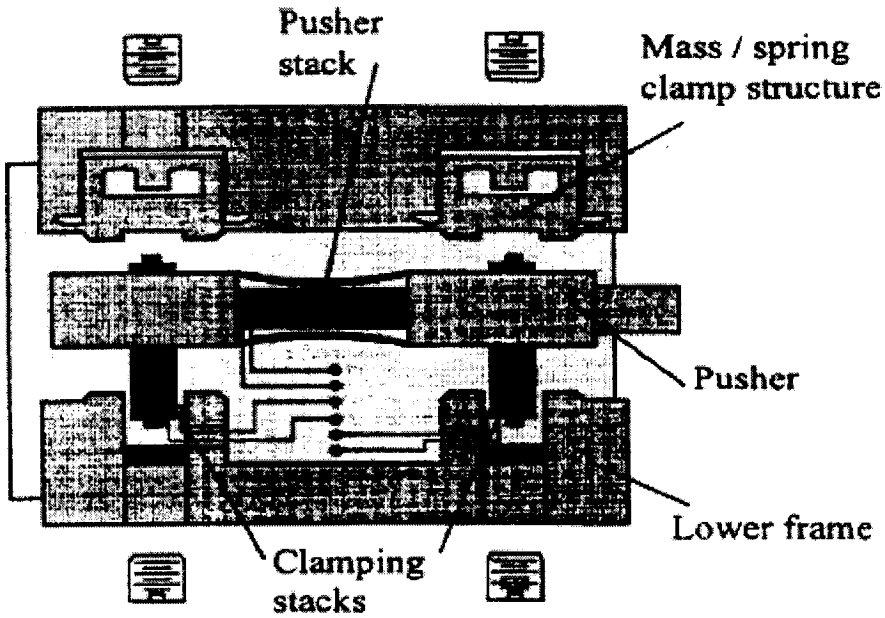

Figure 1.5 Inchworm actuator proposed by Glalante et al. (1999)[33]

The cylinder shape inchworm actuator presented by Sekine et al.[28] shown in Figure 1.6 also demonstrated very good holding and linear driving forces, however the structure was more complex and costly in comparison to the those addressed previously.

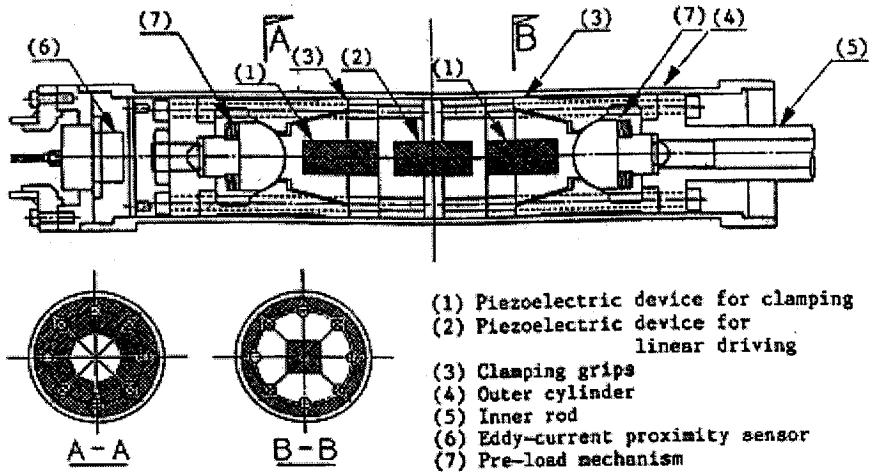

Figure 1.6 Inchworm actuator proposed by Sekine et al. (1990)[28]

1.6 Present study

It can be realized that although many inchworm-type actuator designs including many patents have been proposed in the past forty years, their performance, especially the holding and the linear driving forces are found to be not satisfactory in order to be effectively used in vibration suppression applications. The only commercial product is produced by Burleigh Instruments Ltd[24]; and its driving force is only 15 N. Therefore, most of such actuators were used in position control.

The objective of this research is to present a proof-of-concept design of a high load, high resolution, high speed, unlimited travel range and practicable inchworm-type linear piezoelectric actuator which could be used in adaptive variable geometry truss structure for both position and vibration control. Since the development of a robust clamping mechanism

is essential to realize the high force capability, a considerable design effort has been focused on optimizing the clamping device to increase the output force. CATIA is used as a platform to model the whole actuator and ANSYS is used to analyze and optimize the performance of the actuator. A prototype of the actuator has also been fabricated and extensive experimental study has been conducted to validate the analytical simulations.

The main contributions of the this research study has been summarized as follows:

- The flexure frame clamps has been optimized to increase the output force and to limit the maximum stress using parametric design module of ANSYS. A parametric finite element model of the flexure frame clamps has been developed.
- The proposed design avoids the tight tolerances of the tube diameters. Most of the parts have only normal tolerances which can be easily fabricated in our university machine shop.
- The moving shaft automatically keeps alignment with the central axis by six identical flexure clamps.
- Special design on support rings with the adjustment device and carefully adjustment make the zero clearance possible between the clamps and the moving shaft, which will increase the clamping force greatly.
- The moving shaft of the actuator could also be replaced by one element of the truss structures for vibration suppression and position control purposes.
- The changeable flexure clamps and the pre-load system provide a way to improve the dynamic characteristics of this concept design by experiment and the FEA in the future.

1.7 Thesis organization

The present thesis contains six chapters. Chapter 1 introduces the problem under investigation and the motivation. After defining basic concepts of adaptive structures and actuators, a historical perspective to the field of inchworm piezoelectric actuator is presented with the most important and relevant contributions to the field to date. The chapter concludes by identifying the most important and relevant contributions of the present study and the layout of the monogram.

Chapter 2 introduces the smart materials especially the PZT materials. The electrical mechanical coupled equations are presented, which are the basis of finite element analysis to simulate the performances of inchworm actuator. Material selection and transformations of material parameters are also discussed.

Chapter 3 introduces the basic technique to design an inchworm actuator including the concept of flexure structure. Then, the concept design including main components and subassembly are presented. Three-dimensional solid models of components and assemblies using CATIA are displayed.

Chapter 4 presents the results of finite element analysis of the key parts by using ANASYS. The optimization method, process and the results of flexure clamps are also presented. Finally the working procedure simulation of the designed inchworm actuator by FEM has been demonstrated.

Chapter 5 is devoted to an introduction of prototype assembly and the experiment configuration. Test results including PZT stacks, brake device, extension device and the pre-load systems are discussed. Comparisons of the experiment and the simulation are also presented.

Finally, Chapter 6 summarizes the results of this research and conclusions of development of this novel inchworm-type linear piezoelectric actuator. Future work to improve the proposed actuator has also been presented.

CHAPTER 2 PIEZOELECTRIC MATERIAL

2.1 Introduction

Since the Eighties, there has been an ever-increasing interest in the adaptive structure. This is partly due to the impact of advances in materials technology. With the appearance and the advances of "smart material", it became feasible to develop a new generation of actuators, solid state actuators, which are more compact with high energy densities, larger actuating forces with excellent positioning accuracy and quicker response with good dynamic properties. These new solid-state actuators normally consist of smart materials and mechanical linkages. The performances of these actuators mainly depend on the type of smart material, which is used in actuator. Understanding smart materials and choosing the proper material for the actuator is a key factor to develop a high performance actuator.

2.2 Smart material

Upon reviewing the abundance of literature on the adaptive structures, one can find many different terms about smart materials, such as intelligent materials, adaptive materials, and active materials, which are often used interchangeably. The term smart material generally designates a material that changes one or more of its properties in response to an external stimulus. These materials have the ability to change the shape, stiffness, position, natural frequency, damping friction, fluid flow rate, and other mechanical characteristics of adaptive structures in response to changes in temperature, electric field strength, or magnetic field. Four of the most widely used smart materials nowadays are piezoelectric Pb (Zr, Ti) O_3 (PZT), magnetostrictive (Tb, Dy) Fe_2 (Terfenol-D), electrostrictive Pb (Mg, Nb) O_3 and shape memory alloy NiTi (SMA) [43]. For the sake of comparison, these materials are tabulated in Table 2.1.

Table 2.1 Comparison of four types of smart materials [8]

	Thermal Dilatation	Magneto-striction	Peizostriction	Electrostriction
Strain ($\Delta l / l$)	$10^{-5} \sim 10^{-3}$	$10^{-5} \sim 10^{-3}$	$10^{-4} \sim 10^{-2}$	$10^{-9} \sim 10^{-5}$
Hysteresis	Small	Large	Large	Small
Aging	Small	Small	Large	Small
Response	sec	nsec ~ μsec	msec	μsec
Drive power	Heat	Magnetic coil	Electric field	Electric field

Shape Memory Alloys (SMA) which can induce strain by temperature are best suited to one-way tasks such as deployment. In any case, they can be used only at low frequency and for low precision application, mainly due to the difficulty of cooling process. The best known SMA is the NITINOL. Magnetostrictive materials can be used as load carrying elements (in compression alone) and also as high precision positioner, however they require a driving coil. The best known magnetostrictive material is the TERFENOL-D. On the contrary, piezoelectric and electrostrictive materials can be induced by an electric field strength, and relatively large strain can be obtained. Hence, they are considered the most promising smart material and they can be used as actuators as well as sensors.

There are two broad classes of piezoelectric materials used in adaptive structures: ceramics and polymers. The piezopolymers are used mostly as sensors. The best known is the polyvinylidene fluoride (PVDF or PVF2). Piezoceramics are used extensively as actuators and sensors, for a wide range of frequency including ultrasonic applications, piezoelectric stacks and the great potential usage of collocated actuator/ sensor pairs in adaptive structures.

They are well suited for high precision in the nanometer (1nm=10^{-9} m) and vibration control. The best known piezoceramic is the Lead Zirconate Titanate (PZT).

2.3 Piezoelectric material

PZT material is the most widely used piezoelectric material because of its wide bandwidth, fast electromechanical response, relatively low power requirements and high generative forces. The most important property of PZT material is its piezoelectric characteristics. The piezoelectricity can be considered a generalized transformer between the structural states (stress and strain) and the electrical states (charge and voltage). It was first discovered by J. and P. Curie in 1880. The characteristic that certain crystalline materials would develop an electric charge proportional to a mechanical strain and stress has been used to develop sensor. The converse phenomenon, a geometric strain deformation proportional to an applied voltage, has been used in the development of actuators. The early history of piezoelectric crystals can be found in the fundamental book written by Cady[44].

PZT ceramics are fabricated from pressed and fired powders and can therefore be made in a wide variety of shapes and sizes. The permanent dipole moments in the piezoelectric material are introduced by heating the material beyond its Curie temperature, applying a large electric field strength, and cooling the structure to the operating temperature. This process leaves a permanent charge density on the cooled material and is called "poling" treatment. Figure 2.1 shows the explanatory result of polarization. If a voltage of the same polarity as the poling voltage is applied to a ceramic element, in the direction of the poling voltage, the element will lengthen and its lateral dimension will become smaller. If a voltage of polarity opposite that of the poling voltage is applied, the element will become shorter and broader. This is basically actuation characteristic of piezoelectric materials in which electrical energy is converted into mechanical energy.

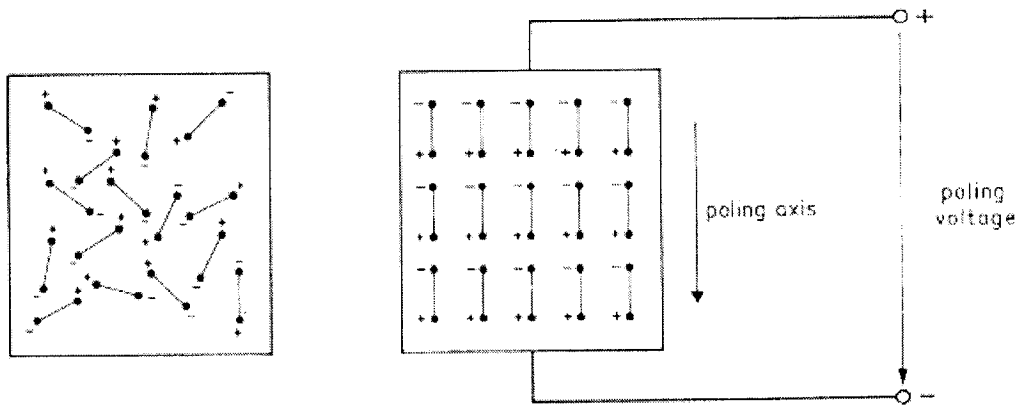

Figure 2.1 Polarization of piezoelectric ceramics [45]

2.4 Piezoelectric coefficients

Jaffe and Cook [46] introduced the piezoelectric effect in ceramics and the definition of terms and the electromechanical coupling constitutive relation. The properties of a piezoelectric ceramic are defined by the piezoelectric, dielectric, and elastic coefficients[47]. These piezoelectric coefficients provide the relationship between electrical and mechanical quantities. They will be introduced briefly as follow.

2.4.1 Definitions of piezoelectric material constants

Before introducing the electromechanical coupling constitutive equations, definitions of piezoelectric material constants have to be defined according to the IEEE standard. Since the constants in piezoelectric materials depend on boundary conditions and the directions of electric field strength, displacement, stress and strain, one superscript defining the boundary conditions and two subscripts defining the directions of respond and the applied loads are

used to better define the piezoelectric material constants. These notations are summarized as follow:

Superscript T: free condition (constant stress T=0)

Superscript E: short circuit (constant field E=0)

Superscript D: open circuit (constant displacement)

Superscript S: clamped condition (constant strain S=0)

The main piezoelectric material constants are

ε: permittivity of the medium (IEEE std) Farads/meter

g: piezoelectric voltage constant (IEEE std) Volt meter/Newton or meter^2/Coulombs

d: piezoelectric charge constant (IEEE std) Coulombs/Newton or meter/Volt

e: piezoelectric constant (IEEE std) Coulombs/meter^2

For ε, the first subscript gives the direction of the electric of displacement; the second indicates the direction of the electric field strength.

For g and d, the first subscript refers to direction of the electric field strength or displacement, and the second subscript gives the direction of the mechanical stress or strain.

For e, the first subscript gives the direction of stress; the second indicates the direction of the electric field strength.

In the definitions of constants, not all superscripts and subscripts are used just for simplification and clearness. Their matrix formats will be presented in Section 2.5.

The permittivity of the medium, ε, relates the electric displacement, D, and the electric field strength, E, through the following equation:

$$D=\varepsilon E \tag{2-1}$$

It is noted that the electric field strength is related to the applied voltage, V, and thickness of piezoelectric material, hp, and can be written as :

$$E=V/hp \tag{2-2}$$

By direct piezoelectric effect, the applied stress creates an electric charge, which is proportional to the force. By converse effect, an applied electric field strength produces a proportional strain (expansion or contraction depending on polarity).

The relationship between the applied stress, T, and electric displacement, D, can be explained as:

$$D = d\,T \tag{2-3}$$

where as explained before d is the piezoelectric charge constant. Also the generated strain, S, due to the applied electric field strength, E, can be described using the constant d as:

$$S = d\,E \tag{2-4}$$

It is noted that in Eq. (2-3) the unit of piezoelectric constant d is Coulombs/Newton while in Eq. (2-4), it is expressed in meters/Volt. Considering Eqs. (2-3) and (2-4), the piezoelectric constant can be described as:

$$d = D/T = S/E \tag{2-5}$$

The relationship between the generated electric field strength and applied stress or strain and electric displacement can also be described using the piezoelectric voltage constant, g, as:

$$E = -\,g\,T \text{ or } S = g\,D \tag{2-6}$$

Considering Eq. (2-6), the piezoelectric voltage constant g can be written as:

$$g = -\,E/T = S/D \tag{2-7}$$

Now substituting Eqs. (2-1), and (2-4) into (2-7), the relationship among piezoelectric voltage constant g, piezoelectric constant d and the permittivity ε^T can be written as:

$$g=d/\varepsilon^T \quad (2\text{-}8)$$

It is noted that for actuating purposes high constant d is desirable while for sensing purposes high g is suitable.

The piezoelectric constant, e can also be used to relate the applied stress, T, to the electric field strength, E, as:

$$T= - e E \quad (2\text{-}9)$$

Electromechanical coupling coefficient, k, provides ratio of the electrical and mechanical energy of the piezo-element, which is an indicator of the converting effectiveness.

k^2 = mechanical energy stored / electrical energy applied (2-10)

or

k^2 = electrical energy stored / mechanical energy applied (2-11)

$$k^2 = - d^2 / (s^E \varepsilon^T) \quad (2\text{-}12)$$

or

$$k^2/(1-k^2) = (g^2 \varepsilon^T) / s^D \quad (2\text{-}13)$$

The relative dielectric constant, K, is the ratio between the permittivity ε and that of free space ε_o. It is frequently referred to simply as the dielectric constant.

$$K=\varepsilon / \varepsilon_o \quad (2\text{-}14)$$

The relationship between the coefficient k and constant K can be described as:

$$K^S= K^T (1 - k^2) \quad (2\text{-}15)$$

where $\varepsilon_o = 8.854 * 10^{-12}$ F/m

2.5 Electromechanical constitutive equations for linear materials

For linear materials, by using piezoelectric constants and combining them with the relationships between stress and strain in the traditional solid mechanics, the electromechanical constitutive equations can be written as follow:

$$\{S\}=[s^E]\{T\}+[d]\{E\} \tag{2-17}$$

$$\{D\}=[d]^t\{T\} +[\varepsilon^T]\{E\} \tag{2-18}$$

where s^E denotes the compliance of the medium under the short circuit boundary condition and s=1/Y where Y is the elastic modulus. Symbol $[\ ]^t$ means transpose of a matrix.

These coupled electromechanical equations provide the strain S and electric displacement D when stress and the electric field strength are applied on the medium simultaneously. The Eqs. (2-17) and (2-18) establishes the interaction between the electrical and mechanical behavior of the medium and describe the direct and converse piezoelectric effect, respectively. It is noted that the material properties $[s^E]$, [d], and $[\varepsilon^T]$ are in a matrix form and strain {S}, stress {T}, electric field strength {E}, and electric displacement {D} are in vector format.

By choosing different independent variables, the Eqs. (2-17) and (2-18) can be transferred to the different formats. The following format is adopted by ANSYS [48] :

$$\{T\}= [c^E] \{S\} - [e] \{E\} \tag{2-19}$$

$$\{D\}= [e]^t\{S\} + [\varepsilon^S] \{E\} \tag{2-20}$$

where $[c^E] = [s^E]^{-1}$ is the stiffness matrix evaluated at constant electric field strength, i.e. short circuit, $[\varepsilon^S]$ is the permittivity matrix under the constant strain, i.e. mechanically clamped boundary condition, and [e] is piezoelectric constant matrix.

2.6 Boundary conditions

It should be pointed out that there are significant effects of the electric boundary conditions (such as short circuit or open-circuit) on the mechanical properties and mechanical boundary conditions (such as clamped or free) on dielectric permittivity of a PZT material.

For example, by applying a compressive force with electrically connected electrodes on PZT stack (short circuit) the charge induced by the deformation at the upper and lower surface can flow through the connection and thus the potential on the electrodes is maintained. On the other hand, by applying the same force with disconnected electrodes (open circuit), the charge induced by the compressive deformation accumulates on the electrodes. The accumulated charges create an electric field, which provoke a force opposite to the external one. This results in a smaller deformation and consequently the apparent stiffness of the piezoelectric will be larger. For instance in PZT ceramics the stiffness with open circuit can be 20 – 40 % larger than that with short- circuited electrodes. Similar to electric boundary conditions, the dielectric permittivity of a piezoelectric stack, measured in clamped or free mechanical conditions, will show significant differences. Therefore, it is crucial to exactly specify both electrical and mechanical boundary conditions when using electromechanical constitutive equations or piezoelectric material constants.

Using Eqs. (2-17) to (2-20), some useful relationships can be established between different boundary conditions. Multiplying both sides of Eq. (2-17) by inverse of $[s^E]$, we can obtain the following relation for stress field $\{T\}$:

$$\{T\}=[s^E]^{-1}\{S\}-[s^E]^{-1}[d]\{E\} \tag{2-21}$$

Comparing Eqs. (2-19) and (2-21), we may have:

$$[c^E]=[s^E]^{-1} \tag{2-22}$$

and

$$[e]= [s^E]^{-1}[d] = [c^E][d] \tag{2-23}$$

which provides the relationship between constant matrices [e] and [d].

Now substituting Eq. (2-21) into Eq. (2-18) will yield:

$$\{D\}=[d]^t [s^E]^{-1}\{S\}+([\varepsilon^T] - [d]^t[s^E]^{-1}[d])\{E\} \quad (2\text{-}24)$$

Comparing Eq. (2-24) with Eq. (2-20), we may find the following relationship between the permittivities of the PZT in clamped and free mechanical boundary conditions:

$$[\varepsilon^S]= [\varepsilon^T] - [d]^t[s^E]^{-1}[d] \quad (2\text{-}25)$$

or

$$[\varepsilon^S]= [\varepsilon^T] (1-k^2) \quad (2\text{-}26)$$

In a similar way the relation between the stiffness in short-circuit and open-circuit conditions can be derived [45]:

$$[s^D] = [s^E] (1-k^2) \quad (2\text{-}27)$$

2.7 Conversion of piezoelectric material matrix

Although the PZT ceramic itself is initially isotropic, this isotropy is not maintained in the presence of electric field. Therefore, the elastic, dielectric and piezoelectric properties are orientation-dependent in piezoelectric materials. Consequently, each constant generally has two subscripts that indicate the directions of the two related quantities. The direction of positive polarization is usually considered to be the Z-axis of a rectangular coordinate system of X, Y, and Z axes. Direction X, Y, and Z is usually represented by the subscript 1, 2, and 3, respectively, and moment about these axes is represented by the subscript 4, 5, and6, respectively as shown in Figure 2.2.

Unfortunately this index system which is based on IEEE standards [49] is slightly different from the index system adopted in solid mechanics. This difference can be easily realized from Figure 2.2. Most published papers and also manufacturer-supplied data are

based on the IEEE standard. Thus the stress vector {T}, strain vector {S}, and the material data matrices have to be transferred from IEEE standards to Solid Mechanics system in order to supply correct data into ANSYS. In other words the order of six components X, Y, Z,YZ, XZ, XY have to be changed to X,Y, Z, XY,YZ, XZ.

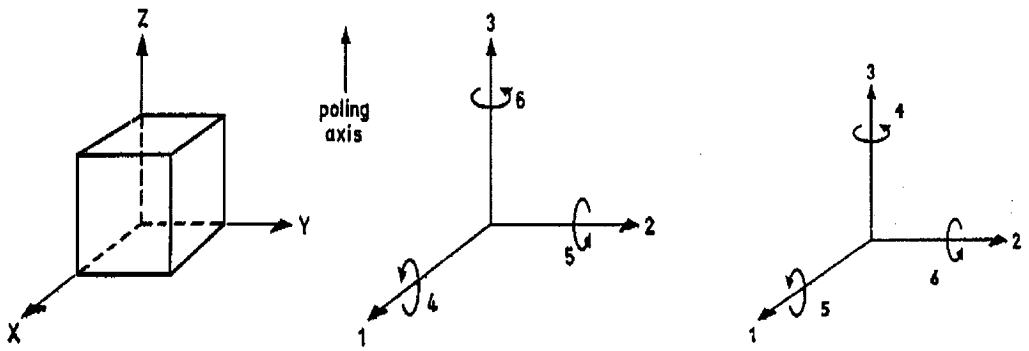

Notation of IEEE Notation of Solid Mechanics

Figure 2.2 Notations of axes in two different systems

Since poled ceramics normally have cylindrical symmetry because of their planar isotropy, therefore when Z axis (3 direction) has been selected as poling axis, X and Y axes (2 and 3 directions) can be arbitrarily chosen in the plane normal to poling axis. Then the independent material constants will be reduced, such as $d_{31}=d_{32}$, $d_{24}=d_{15}$, $e_{31}=e_{32}$, $e_{24}=e_{15}$, $\varepsilon_{11}=\varepsilon_{22}$, $s^{E}_{11}=s^{E}_{22}$.

2.8 Piezoelectric material data for ANSYS

ANSYS is a powerful commercial general-purpose finite element analysis software capable of electro-mechanical multidisciplinary analysis. ANSYS performs piezoelectric analysis using the direct-coupled analysis method. Before analysis of the piezoelectric model, the material properties such as permittivity (or dielectric constants), the piezoelectric and

elastic coefficient matrices have to be specified accurately. Since the manufacturer supplied data based on the IEEE standard normally are different from the data based on solid mechanics, proper adjustment should be undertaken. The piezoelectric material input data fed to the ANSYS can be obtained by making the following adjustment:

For piezoelectric matrix

- IEEE constants [e_{61}, e_{62}, e_{63}] would be input as the ANSYS xy row
- IEEE constants [e_{41}, e_{42}, e_{43}] would be input as the ANSYS yz row
- IEEE constants [e_{51}, e_{52}, e_{53}] would be input as the ANSYS xz row

For elastic coefficient matrix

- IEEE terms [c_{61}, c_{62}, c_{63}, c_{66}] would be input as the ANSYS xy row
- IEEE terms [c_{41}, c_{42}, c_{43}, c_{46}, c_{44}] would be input as the ANSYS yz row
- IEEE terms [c_{51}, c_{52}, c_{53}, c_{56}, c_{54}, c_{55}] would be input as the xz row

For permittivity matrix, i.e. dielectric constants, most manufacturers list only relative dielectric constant at constant stress, i.e. K^T, but ANSYS requires the permittivity matrix at constant strain, i.e. $[\varepsilon^S]$. Considering Eqs. 2-25 and 2-14, this matrix can be obtained from the following equation:

$$[\varepsilon^S] = \varepsilon_o [K^T] - [d]^t [s^E]^t [d] \tag{2-28}$$

After using transversely isotropic property of piezoelectric material to remove dependent constants and assuming that Z or 3 axis is poling axis, and the plane normal to 3 axis is transversely isotropic, the ANSYS piezoelectric material data transferred from IEEE standard data can be summarized as follows. Piezoelectric Constant Matrix:

$$[e]= [s^E]^{-1}[d] = [c^E]\,[d] = \begin{vmatrix} 0 & 0 & e_{31} \\ 0 & 0 & e_{31} \\ 0 & 0 & e_{33} \\ 0 & 0 & 0 \\ 0 & e_{15} & 0 \\ e_{15} & 0 & 0 \end{vmatrix} \tag{2-29}$$

$$[d]^t = \begin{vmatrix} 0 & 0 & 0 & 0 & 0 & d_{15} \\ 0 & 0 & 0 & 0 & d_{15} & 0 \\ d_{31} & d_{31} & d_{33} & 0 & 0 & 0 \end{vmatrix} \tag{2-30}$$

Compliance / Stiffness Matrix:

$$[s^E] = [c^E]^{-1} = \begin{vmatrix} s_{11}^E & s_{12}^E & s_{13}^E & 0 & 0 & 0 \\ & s_{11}^E & s_{13}^E & 0 & 0 & 0 \\ & & s_{33}^E & 0 & 0 & 0 \\ & & & s_{66}^E & 0 & 0 \\ & & & & s_{44}^E & 0 \\ & & & & & s_{44}^E \end{vmatrix} \tag{2-31}$$

where $s_{66}^E = 2(s_{11}^E - s_{12}^E)$ (2-32)

Permittivity Matrix:

$$[\varepsilon^S] = \varepsilon_o \begin{vmatrix} K_{11}^T & 0 & 0 \\ & K_{11}^T & 0 \\ & & K_{33}^T \end{vmatrix} - [d]^t\,[s^E]^{-1}[d] \tag{2-33}$$

It is noted that for a two-dimensional model, these matrices are modified and reduced further. In the 2D system, the Y-direction is the "polarization" direction and requires a 90-degree transformation of 3D matrices mentioned above, which switches the y and z

directions. The rows and columns representing "xz" and "yz" terms are finally deleted from these matrices, leaving the proper input for a 2D system.

A program file has been developed in MATLAB (Appendix A) in order to convert the published material data into the format required for the ANSYS 2D or 3D models.

2.9 Material selection

A wide variety of piezoelectric materials are currently available. There are several companies which can supply different kinds of PZT ceramics, such as Polytec PI [50], Morgan Advanced Ceramics [51], APC International Ltd [52], Sensor Technology Ltd [53] and others. After comparing the specifications of several PZT materials, BM532 produced by Sensor Technology Ltd has been chosen as driving element, which has high piezoelectric charge constants d_{33} and other suitable properties. It was also decided to order the PZT stack from Sensor Technology Ltd due to its expertise in this field and short delivery time.

BM532 belongs to "soft" piezoelectric materials, which are characterized by large electromechanical coupling factors, large piezoelectric constants, high permittivity, large dielectric constants, high dielectric losses, low mechanical quality factors, and poor linearity. "Hard" ceramics have characteristics generally in opposite of those of soft ceramics, which shows a wide linear drive region but relatively small strain magnitude. Since PZT material will be working at low frequency region and larger displacement will be desired in this design, "soft" piezoelectric BM532 has been chosen. The specification of BM532 is listed in Appendix B. The closely matched properties of PZT products from different companies are also listed in Table 2.2

Table 2.2 Comparison of closely related PZT materials from different companies [53]

Sensor Technology	Channel	EDO	Keramos	Matroc-Morgan	Navy
BM300	-	-	-	-	-
BM400	5400	EC-64		PZT-4	Type-I
BM500	5500	EC-65	-	PZT-5A	Type-II
BM527	5600	EC-70		PZT-5J	Type-V
BM532	5700	EC-76	-	PZT-5H	Type-VI
BM740				PZT-7A	
BM800	5800	EC-69	-	PZT-8	Type-III
BM900			K81		
BM920	-	-	K83	-	-
BM940			K85		

2.10 Summary

A brief introduction of smart materials has been presented in this chapter. Among these smart materials, piezoelectric ceramic material such as PZT has been discussed due to its relatively good electrical and mechanical exchangeable properties. The characteristics and electrical – mechanical coefficients of PZT material were then introduced in detail. Since the electrical and mechanical boundary conditions have significant effects on the performances of piezoelectric material, they should be clearly identified during the test and simulation of PZT stacks. The electromechanical constitutive equation for PZT material was presented in matrix style and the conversion of piezoelectric material matrix was provided in order to nourish correct PZT material property into ANSYS software. This is because different coordinate systems have been adopted by manufacturers (IEEE standard) and solid mechanics. Piezoelectric BM 532 material has finally chosen as driving element for this research due to its large piezoelectric constants. This chapter provides a basis for the following two chapters about PZT stack design and finite element analysis of electrical – mechanical coupling equations.

CHAPTER 3 PROTOTYPE DESIGN

3.1 Introduction

The main objective of this research is to design a solid-state actuator which could be used as an active element with large stroke and suitable output force in shape control and vibration suppression of the truss space structures. Therefore, maximum displacement with controllable step and maximum output force of actuator will be desired. As concluded in the Chapter 1, inchworm-type actuator would best fit this objective.

In this chapter, the concept design and detailed design of a novel inchworm-type actuator and its subassembly will be introduced. CATIA V5 [54] is used as a platform to model the whole actuator and its all components and assemblies. The three-dimensional model of actuator constructed by CATIA V5 software will greatly help to realize and visualize different components and assembly modeling before manufacturing, to check the interferences of the assembly, to draft 2D drawings, to modify the design according to the analysis and even to build FEA model in ANSYS. Any changes in the design could be updated at any stage. In fact, design, analysis, and revision have been cycled in the actuator design process. Most analyses and design optimization tasks have been accomplished using finite element method, which will be addressed in Chapter 4. Two-dimensional drawings of all the parts and assemblies are attached in Appendix C.

3.2 Concept design

The prototype inchworm actuator will adopt "pusher" type and make use of frictional clamping mechanism. It is cylindrical in shape and consists of left and right clamping devices separated by a central expanding device. When fully assembled, the actuator has a diameter of 52mm and measures 275 mm in length, which could be compared with the design

proposed by K. Sekine [28] which has a diameter of 54 mm and a total length of 250 (Figure 1.6). The central expanding device consists of a longitudinal PZT stack and a thin wall tube to provide extension-contraction motion and output force. The clamping device consists of the same type PZT stack, a pre-load mechanism, three flexure arms with flexible hinges and a supporting ring with adjustable screws, which integrates three arms into a frame and connects PZT stack with it. The similar two frictional clamping devices provide alternating braking forces when the moving shaft, which is pushed by the expanding device, walks inside the PZT tubular stack and emulates an inchworm, summing small steps to achieve large displacements. Stainless steel is chosen for nearly all the parts since it has relatively low coefficient of thermal expansion and offers relatively high strength and stiffness.

The proposed design avoids the tight tolerance of the tube diameters, which most tubular inchworm-type actuators are required[28 35]. Meanwhile, the moving shaft automatically keeps alignment with the central axis by six identical flexure arms. Special design on support rings with the adjustment device and careful adjustment makes the zero clearance possible between arms and the moving shaft. The moving shaft of the actuator could also be replaced by one element of the truss structures for vibration suppression and position control purposes. In the proposed actuator, the flexure arms can be easily replaced to outfit different dynamic characteristics. The whole actuator model, the exploded view and the configuration of the different components in the actuator are shown in Figures 3.1-3.3, respectively. The fabricated prototype is also presented in Figure 3.4.

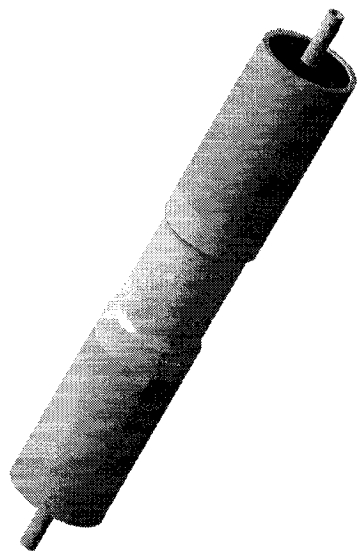

Figure 3.1 Model of piezoelectric inchworm-type actuator

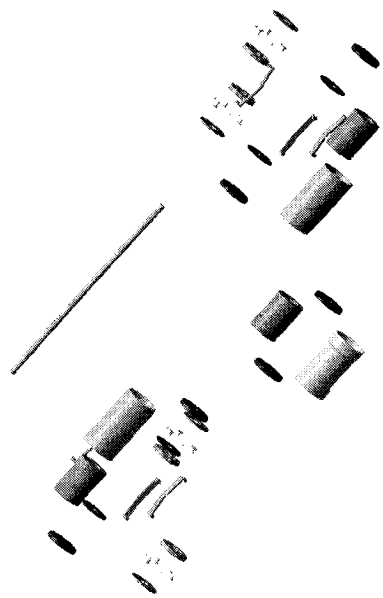

Figure 3.2 Exploded view of the actuator

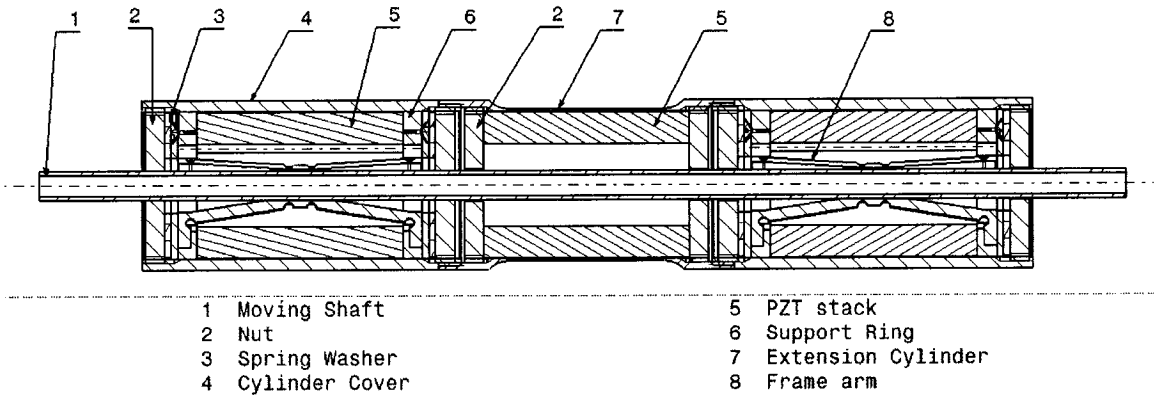

Figure 3.3 Actuator configuration

Figure 3.4 Prototype of the actuator

3.3 PZT stack design

One of the key components in the piezoelectric inchworm actuator is PZT stack. The characteristics of PZT stack have a crucial effect on the performance of the actuator. As

mentioned in Section 2.9 in Chapter 2 , soft material BM532 piezoelectric ceramic has been selected.

From Figure 1.1, it can be realized that the strain induced in a PZT material by applied voltage is very small, thus to increase the longitudinal displacement multiplayer type actuator, piezoelectric stack has been used. Since the amount of deformation in axial dimension is proportional to the applied electric field strength and the d_{33} coefficient of the material, therefore, a high electric field strength is required for large movements. However, low voltage power supplies are cheaper, safer and more readily available and, to achieve a high field from a low voltage, the ceramic layer thickness requires to be as thin as possible. The stacking of such thin layers, to form a multi-layer structure, yields a device which generates large strains at relatively low applied voltages. Piezoelectric stack consists of thin layers of piezoelectric ceramic material electrically connected in parallel. All these thin ceramic are bonded together through epoxy glue. The net positive displacement is the sum of the strain of the individual layers. The thickness of the individual layer determines the maximum operating voltage for the actuator. The stack is capable of microns of expansion, kiloNewtons of force, and tens of microseconds of response time. Figure 3.5 shows the displacement of PZT stack when the external electric voltage is applied.

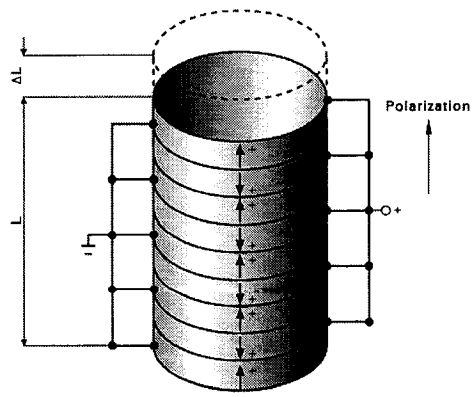

Figure 3.5 Displacement of PZT stack when external electric voltage is applied [55]

3.3.1 Basic dimensional design

The displacement, operating voltage range, stiffness and load capability of the PZT stack are the most important parameters which are required to be specified accurately in order to design a reliable PZT stack. In order to accommodate the three frame arms into the PZT tube, a simple configuration of PZT stack would be cylindrical. The length of the tubular PZT stack depends on the requirement of axial deflection of PZT stack and its cross-sectional area depends on the maximum design output force expected by the PZT stack. Before designing the size of PZT stack, therefore, three kinds of displacement and the concept of blocked force have to be introduced.

3.3.2 The free displacement of PZT stack

The free displacement of PZT stack, in absence of any force along the stack axis, is a function of the applied electric field strength, E, the piezoelectric material and the length of the PZT stack. Figure 3.6 shows the three load conditions: Case (a) demonstrates the free displacement versus the applied voltage of a typical PZT stack. Case (b) and Case (c) presents spring load and constant load conditions, which will be introduced in the next section.

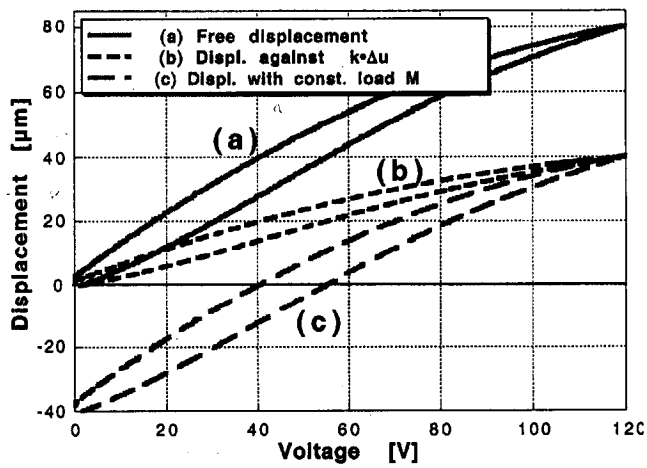

Figure 3.6Comparison among different load conditions [55]

As explained in Section 2.3, the material properties can be identified by the piezoelectric strain coefficients d_{ij}. These coefficients describe the relationship between the applied electrical field and the produced mechanical strain. Using Eq. 2-4, the free displacement of PZT stack can be estimated by the following equation:

$$\delta_o = d_{33}(\pm E)\ t_c\ n \qquad (3\text{-}1)$$

where δ_o is the free displacement with no external force applied, E is the applied electric field strength, t_c is the layer thickness, n is the number of active layers and d_{33} is piezoelectric charge constant, i.e. the ratio of strain in axial direction to the electric field strength applied in the axial direction.

It has to be pointed out that Eq. 3-1 does not include the effect of hysteresis, which is based on the crystalline polarization effects and molecular friction. In fact, the absolute displacement generated by an open loop PZT stack depends on the applied electric field strength and the piezo gain, which is related to the residue polarization. Since the residue polarization, and therefore, the piezo gain is affected by the electric field strength applied to the piezo, thus its deflection depends on whether it was previously operated at a higher or a lower voltage (and some other effects). Therefore, the relation between the displacement and the electric field strength depends on the history of the PZT stack displacements. A typical hysteresis curve for the PZT stack is demonstrated in Figure 3.7. Hysteresis is typically on the order of 10 to 15 % of the commanded motion. Since the displacement of PZT stack is so small, for example, about 2 micron deviation could be existed when a 20 micron free displacement produced by PZT stack and the position repeatability is still on the order of only 2 μm. Classical motor driven by leadscrew positioners will hardly beat this repeatability. To simplify the problem, hysteresis will be not considered in this design.

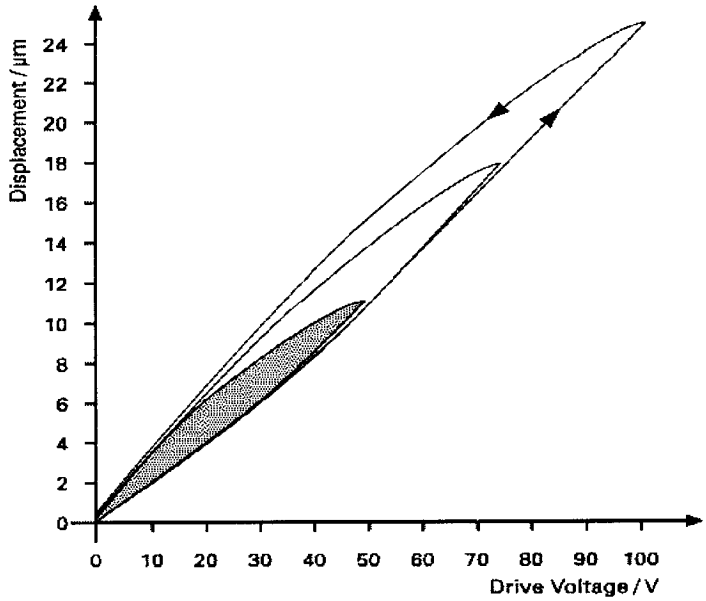

Figure 3.7 Typical Hysteresis phenomenon realized in PZT stack [55]

3.3.3 The displacement of PZT stack with loads

Since the PZT stack will be working under some pre-pressure spring load in this design, the displacement of PZT stack with spring load is apparently more important. In a quasi-static situations, i.e. no inertial forces, the displacement δ_s increases with the applied voltage V and a growing counter spring force $K_s^* \delta_s$ is exerted against the stack. Thus, the maximum extension of the stack will be naturally smaller than that of free displacement.

Generally, there are two basic situations where a PZT stack actuator has to counteract an external force. One is when the PZT stack is counteracting with the preloaded spring and the other when the PZT stack is under constant external load. The maximum or final displacement versus the applied voltage for these two situations are shown in Figure 3.6 (b) and (c), respectively. Figures 3.8 (b) and (c) also demonstrates a schematic representation of these cases. It is obvious from Figure 3.8 (b) that the opposite force is proportional to the displacement with a spring constant K_s (proportional preload), whereas in Figure 3.8 (c), the

load is constant with value M (constant preload). The difference is that the load changes or remains constant during the motion process.

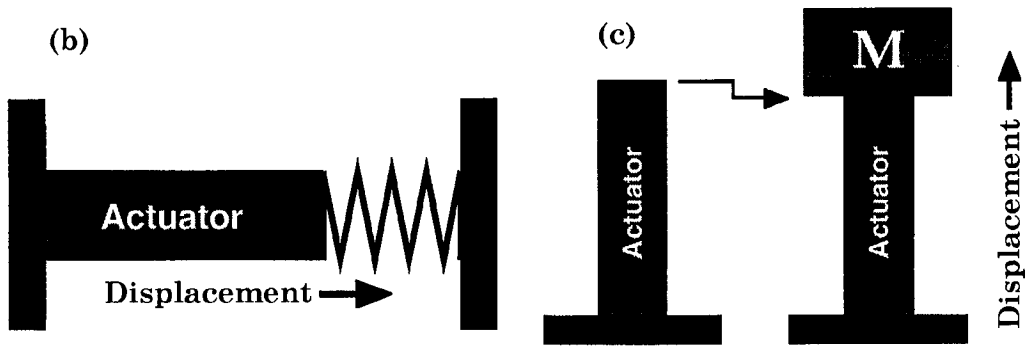

(b) Displacement with a spring load **(c) Displacement with a constant load M**

Figure 3.8 Displacement of PZT stack actuator with end loadings

For the case (b), the total available displacement can be related to the spring stiffness through the following equation:

$$\delta_s = \delta_o (K_p/(K_p+K_s)) \quad (3\text{-}2)$$

and the lost displacement caused by the external spring can be obtained from:

$$\delta_d = \delta_o - \delta_s = \delta_o (1-(K_p/(K_p+K_s)) \quad (3\text{-}3)$$

where

δ_s : displacement of PZT stack with spring load under applied voltage

δ_o : displacement of PZT stack with zero applied load under applied voltage

δ_d : the lost displacement caused by the external spring

K_p : PZT stack stiffness

K_s: spring stiffness

For case (c), the mass is installed on the PZT stack which applies a force of F=M*g (M: mass, g: acceleration due to gravity). If this force is within the specified load limit of PZT stack, full displacement can be obtained at full operating voltage. The zero point offset with constant force can be obtained from:

$$\delta_{offset}=F/K_p \qquad (3\text{-}4)$$

It should be noted that the poling process of Piezo ceramics leaves a residual strain in the material, which depends on the magnitude of polarization. The polarization is affected by both the drive voltage and external forces. When an external force is applied to poled Piezo ceramics, the dimensional change depends on the stiffness of the ceramic material and the change of the residual strain (caused by the polarization change). The equation 3-4 is only valid for small forces and small signal conditions. For larger forces, an additional term describing the influence of the polarization changes, should be superimposed on the stiffness K_p.

3.3.4 The blocked force

The blocked force is the maximum force, which the PZT stack can generate. Basically at maximum force generation, displacement is zero, while at full displacement, no force can be generated. The blocked force depends on the stiffness and maximum displacement of PZT stack and can be formulated as:

$$F_b=K_p * \delta_o=(d_{33}/s^E_{33})\, E\, A \qquad (3\text{-}5)$$

where F_b is the blocked force and s^E_{33} is the compliance of PZT material in axial direction under the short circuit boundary condition. Other notations have been defined previously in Eqs. (3-1) and (3-2).

Considering Eq. (3-3), an effective force generated by the PZT stack under spring loading can be described by:

$$F_{eff} = K_p * \delta_d = K_p * \delta o \left(1-(K_p/(K_p+K_s)) \right) \quad (3\text{-}6)$$

3.3.5 BM 532 stack design

From preliminary analysis on the frame arm in Section 3.5, and the finite element analysis of the compliant mechanism in Section 4.3, the amplification factor of compliant mechanism have been found to be about 5.6. In order to satisfy a general tolerance of fabrication and assembly, minimum 10 μm displacement under at least 1500 N spring pre-load is necessary for the PZT stack. Therefore, the load conditions of designed PZT stack combines the aforementioned (b) and (c) cases in Section 3.3.3 , ie. 1500 N constant force and a spring load with K_p stiffness.

According to the similar size of PZT stack, suppose the stiffness of PZT stack K_p is 500 N/μm [52]. Then using Eq. 3-4 the zero point offset with constant 1500 N force would be 3 μm. When designing preloaded Piezo systems, the stiffness of the preload spring should be less than 1/10 of the Piezo stiffness in order to achieve higher free displacement. Thus in the preliminary design, the K_s has been set to $K_s=(1/10)*K_p$. Now using Eq.3-2, if we set δ_s at 10 μm, then the free displacement δ_o should be at least 11 μm. Therefore, the total free displacement of PZT stack should be about 14 μm.

The designed PZT stack actuator consists of many thin ceramic wafers, which are electrically connected in parallel and bonded together using epoxy glue. Because the electric field strength limit for BM532 is about 400V/mm, the thickness of each ceramic wafer is 0.02 inch (0.508mm) for 200 V. The thickness of shims and glue between each ceramic wafer

is 0.003 inch (0.0762 mm). Considering the above discussion and after extensive study considering the cost, manufacturability, efficiency and accuracy, the following final dimensions of PZT stack have been selected:

- The number of active ceramic wafers is 107.
- The number of inactive ceramic wafers is two for insulation at top and bottom.
- The number of shims and glue layers is 108.
- The total length of PZT stack= 107*0.02+2*0.02+108*0.003=2.5 (inch) =63.5 (mm)
- The inside diameter is 1 inch (25.4mm)
- The outside diameter is 1.75 inch (44.45 mm)

To make sure that the frame arms which will be accommodated inside the tubular PZT stack will not conflict with each other, the internal wiring is used where connections are parallel to the axis of cylinder and separated by 120 degrees. It is noted that the internal tab and wiring envelope should be less than 0.1 inch (2.5mm).

The model of PZT stack and its fabricated prototype are shown in Figures 3.9 and 3.10, respectively.

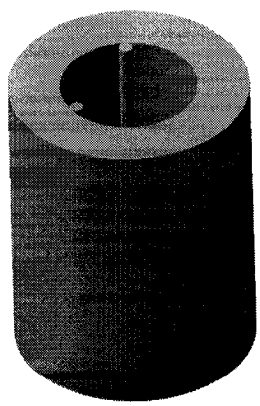

Figure 3.9 Model of PZT stack

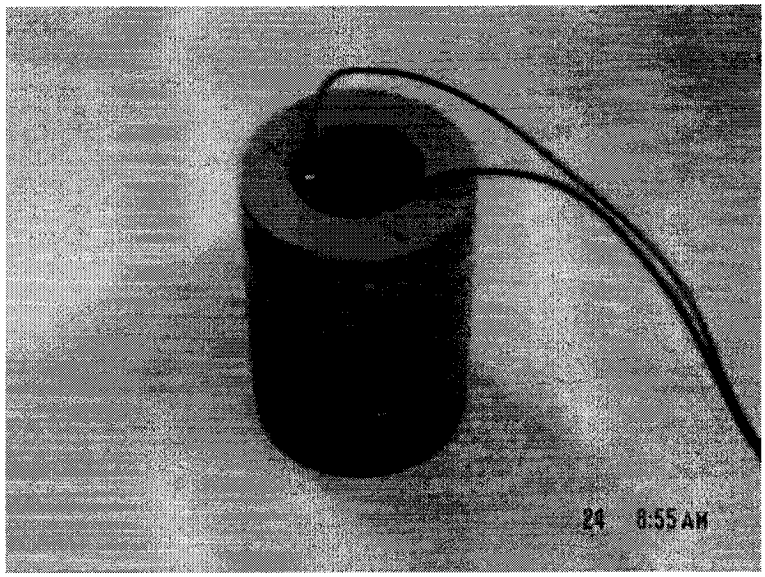

Figure 3.10 Prototype of PZT stack

Now using Eqs. 3-1 and 3-5, the preliminary free displacement with no external force and blocked force of the PZT stack when it is under 200 voltage can be found as:

$$\delta_o = d_{33}(\pm E)\ t_c\ n = \pm 13.5\mu m \qquad (3\text{-}7)$$

$$F_b = d_{33}/s^E_{33})\ E\ A = 13009\ N \qquad (3\text{-}8)$$

where $d_{33}=630 * 10^{-12}$ C/N ; $t_c = 0.508*10^{-3}$ m ; n=107 ; $s^E_{33}=20.0 * 10^{-12}$ m^2/N ;

$E=Volt/ t_c = \pm 200V/0.508mm=\pm 393701V/m$; $A=1.049*10^{-3}$ m^2

Now the stiffness of the PZT stack can be calculated using:

$$K_p=F_b/\delta_o=964\ N/\mu m \qquad (3\text{-}9)$$

The capacitance of the PZT stack can also be obtained from:

$$C = n\ A\ (K^T_{33})\ \varepsilon_o/\ t_c = 6.358\ \mu F \qquad (3\text{-}10)$$

where the relative dielectric constant is $K^T_{33}=3250$ and the permittivity of vacuum is $\varepsilon_o= 8.854 *10^{-12}$ F/m.

Considering Eqs. 3-3, 3-4 and 3-6, the effective force that the proposed PZT stack can generate is

$$F_{eff} = K_p * (\delta_o - \delta s - \delta_{offset}) = 964 * (13.5 - 1 - 3) = 9158 \text{ N} \quad (3\text{-}11)$$

It is noted that:

- The free displacement calculated by Eq. 3-7 does not consider the electrical-mechanical coupling effects produced by PZT material. The more accurate result considering piezoelectric coupling effects will be obtained in Chapter 4.
- The blocked force calculated by Eq. 3- 8 is under the short circuit boundary condition and one-dimensional defection. The more accurate and general result using finite element analysis will be introduced in Chapter 4.
- Epoxy glue has an effect on total stiffness of the PZT stack, which has not been considered here, in fact the real stiffness of PZT stack with epoxy glue, would be smaller than that of without epoxy glue which depends on technology process of PZT stack fabrication.

For the sake of simplicity, manufacturability and cost, all three PZT stacks used in braking and extension devices are decided to be identical.

3.4 Compliant mechanisms design

Since the displacement of PZT stack is still very small (about 13 μm), an efficient and novel compliant mechanism has been designed in order to amplify the PZT displacement. Compliant mechanisms are devices that attain motion by means of elastic deformation of flexible members and flexible hinges.[56] Besides the efficiency and wear-resistance advantages, compliant mechanisms can virtually eliminate the backlash, which is particularly

important due to extremely small displacement generated directly by the PZT stack. The loss of even a few micrometers can have a severe detrimental effect on the performance of the actuator. Another advantage of the compliant mechanism is that the flexible hinges may prevent potential damage caused by possible bending moments or shear forces. It is noted that due to the fragility of PZT ceramics, they cannot stand large pulling and shear stresses. Moreover, an important characteristic of compliant mechanism is its capability to store high strain energy. This stored energy is similar to the potential energy in a deflected spring, and the effects of springs may be integrated into a compliant mechanisms design. To summarize using the compliant mechanism, the energy can be properly stored and then released in an appropriate time or in a different way. Compliant mechanism commonly used in the linear piezoelectric actuators can be divided into two general categories: lever type and frame type devices. Lever type devices (see Figure 1.1 (d) hinge lever), which rely on the ratio of distances between pivots and high transverse lever stiffness to produce displacement amplification, are relatively common due to the their simplicity, although highly efficient designs are difficult to achieve. Takahara [27] designed a clamp arm by using levers and flexible hinge. Although the displacement amplification factor could be as high as 10, the clamping force is found to be small, which resulted in a lower output force of actuator (9.3 N). Frames (quasi pin-jointed) mostly rely on the longitudinal stiffness of their constituent members rather than transverse stiffness, potentially yielding more compact design and large clamping force. Thus, the frame type amplifier design has been chosen for the proposed compliant mechanism.

In proposed novel design, the compliant mechanism consists of three flexure clamps with flexible hinges, two support rings and two cover wafers, which integrate all three flexure clamps into a frame. Figure 3.11 shows the proposed model of the compliant mechanism and Figure 3.12 presents the photo of the fabricated prototype. The compliant mechanism lodged

into tubular PZT stack is also presented in Figure 3.13. Using this compliant mechanism, the axial displacement generated by the PZT stack will be amplified and then simultaneously transferred to the transverse displacements of the clamp centers. Using this unique feature, the tubular PZT stack is also guarded by the flexible hinges of the compliant mechanism from tilting due to the shear forces, which may cause significant damage to the PZT stack. The amplification factor of displacement depends on the geometry of the clamps, and the force transformation ability is decided by the stiffness of the compliant mechanism. The stainless steel 304 has been used for all components of compliant mechanism in order to obtain relatively larger stiffness.

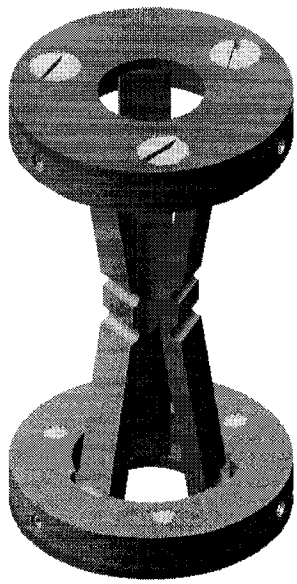

Figure 3.11 Compliant mechanism with three clamps

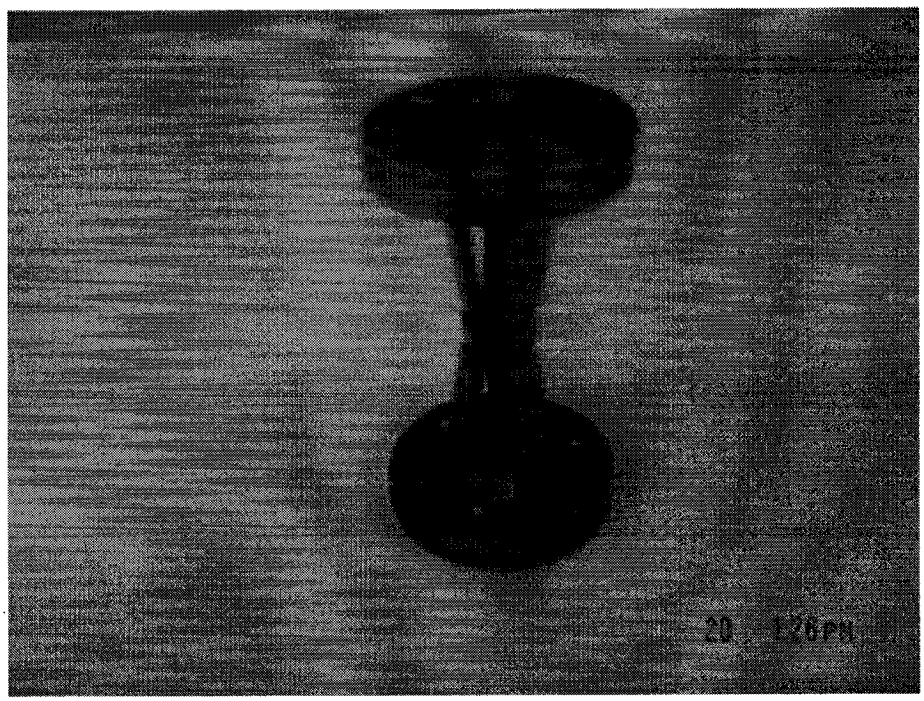

Figure 3.12 Prototype of compliant mechanism

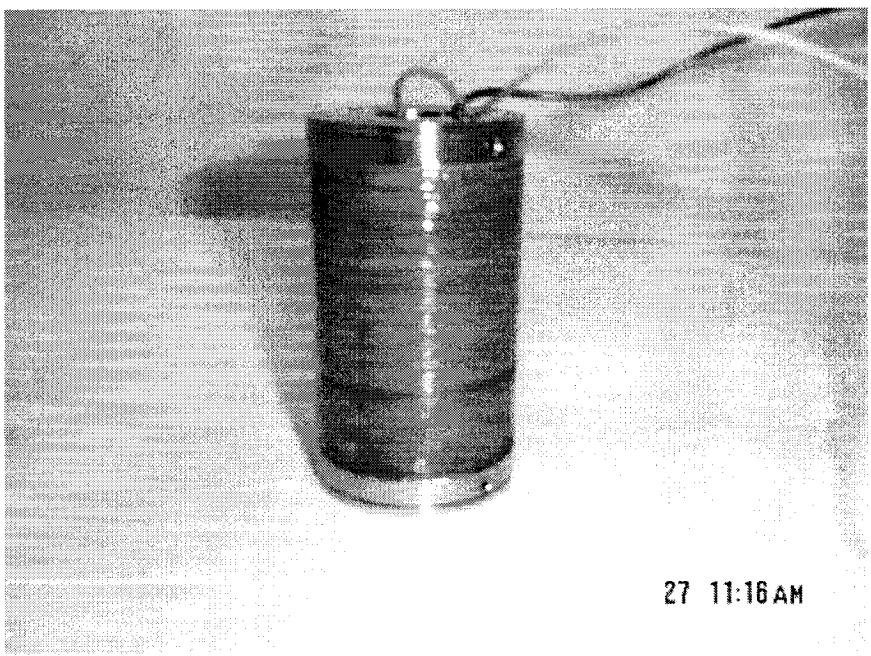

Figure 3.13 Compliant mechanism with tubular PZT stack

3.5 Flexure clamp design

The objective of the flexure clamp design is to obtain the maximum clamping force with suitable displacement amplification by optimizing the force/displacement characteristics of clamping arms and long lifetime by minimizing the stress. The flexure clamps must be also very stiff in the pushing direction to transfer force generated by the PZT stack, however they should be soft enough in other degrees of freedom in order to avoid possible damage to the ceramics. Before elaborating on the flexure clamp design, it is important to introduce the concept of the flexible hinge.

3.5.1 Flexible hinges

Functionally, an ideal flexure hinge allows limited relative rotation of the rigid adjoining members while prohibiting any other types of motion. The typical flexure hinge consists of one or two cutouts that are machined in a blank material. Flexible hinges have several advantages over the classical rotational joints, including no friction losses, no need for lubrication, no hysteresis, compactness, capacity to be utilized in small-scale applications, ease of fabrication, virtually no assembly, and no required maintenance.

When frame type amplifying linkage topology is adopted (see Section 3.4), the geometrical profile of the hinges plays an important role in the overall efficiency of the actuator and thus has to be properly design optimized. Paros and Weisbord [57] developed analytical methods to design circular and right circular hinges and presented the design equations, in an exact and simplified format, to calculate the compliances (spring rates) of single-axis and two-axis circular cutout constant cross-section flexure hinges. Xu and King [58] performed static finite element analysis of circular, corner-filleted and elliptic flexure hinges. The results revealed that the corner-filleted flexure is the most accurate one in terms of motion; the elliptic flexure generates less stress for the same displacement, while the right

circular flexure is the stiffest one. Lobontiu et al.[59] researched the symmetric conic-section flexure hinges based on the closed-form compliance equation and concluded that the elliptic, parabolic and hyperbolic flexure hinges (in this order) are more compliant than the circular ones for large length to-thickness ratios. The hyperbolic flexures perform the best in terms of preserving the center of rotation position. Since the right circular hinge profile is the most common profile used in flexure-hinged displacement amplifiers due to its simplicity and high stiffness, the right circular hinge profile flexible frame design has been utilized in the design of flexible frame mechanism.

3.5.2 Displacement amplification of flexure clamp

Some compromise has to be considered for the design of flexure clamp. The larger displacement amplification allows better compensation for manufacturing tolerances and larger clearance between the moving shaft and the clamping concave surfaces, but the achievable clamping force and the stiffness are reduced linearly and quadratically with the displacement amplification factor, respectively. In order to achieve the sufficient clamping force, an intermediate and reasonable displacement amplification factor is adopted. A special design of adjustment device on the support ring has been proposed to compensate the manufacturing tolerance and thermal expansion or contraction, which will be introduced in Section 3.6.

The length of the flexure clamp is decided by the length of PZT stack. As preliminary estimation, the linkages are considered to be rigid bodies as shown in Figure 3.14. Thus the transverse displacement can be related to the axis displacement using:

$$dy = (x/y)\, dx \qquad (3\text{-}12)$$

Considering the arm angle of 9 °, the ideal kinematics' amplification factor will be

$$dy/dx = \text{ctan}(9^{\circ}) = 6.3 \qquad (3\text{-}13)$$

In reality the clamping arm will bend causing the amplification factor to reduce. The result obtained from FEA calculation (Chapter 4) has confirmed the amplification factor of 5.7

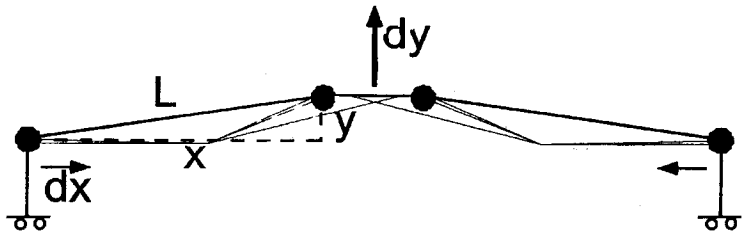

Figure 3.14 Ideal amplification factor of clamping arm

3.5.3 Final design of flexure clamp

An extensive design optimization procedure to find the optimum topology of the clamping arm has been carried out in order to increase the clamping force while limiting the maximum stress using the parametric design module of ANSYS, which will be presented in detail in Chapter 4. The proposed optimum configuration of the flexure clamp can amplify the displacement and effectively transfer the force produced by PZT stack in order to obtain the maximum output force. In order to increase the contact surface between clamping arms and center shaft, a concave profile has been cut out of the center part of the flexure clamp. The diameter of concave is the same as that of the center shaft. The width of the clamping

arms should be as large as possible. The final model of one clamping arm has been shown in Figure 3.15. Figure 3.16 demonstrates the upper view installation of the three clamping arms.

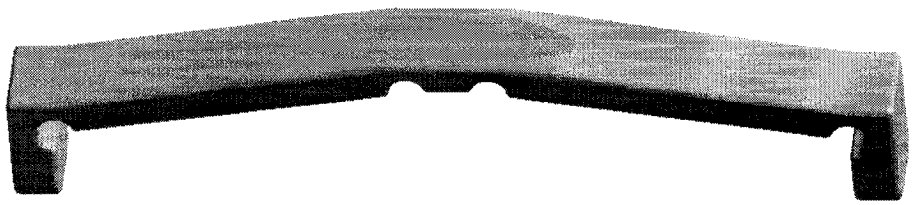

Figure 3.15 Model of the clamping arms

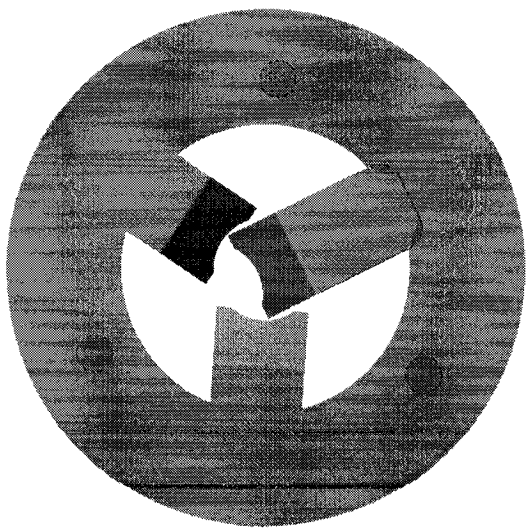

Figure 3.16 The clamping arms installation

3.6 Supporting ring design

The designed supporting rings have two distinct functionalities. One is to integrate three clamping arms into a compliant mechanism and keep two ends of clamping arms by using cover wafers. Another is to adjust the positions of clamping arms using the adjusting screws along the radial direction of supporting ring. With this provision, it is possible to significantly reduce the manufacturing and assembly tolerances. The proposed adjustable clamping arms are not only to reduce the cost of manufacturing prototype but also to assure that the actuator functions well in a tight assembly tolerance. From literature review, it has been realized that some of the inchworm-type actuators could not function as expected mainly due to their imperfect manufacturing tolerances since the displacements of PZT stacks are very small.

The exploded view of the supporting ring assembly has been shown in Figure 3.17. As shown in the figure cover wafer is connected to the supporting ring through three-countersunk screws.

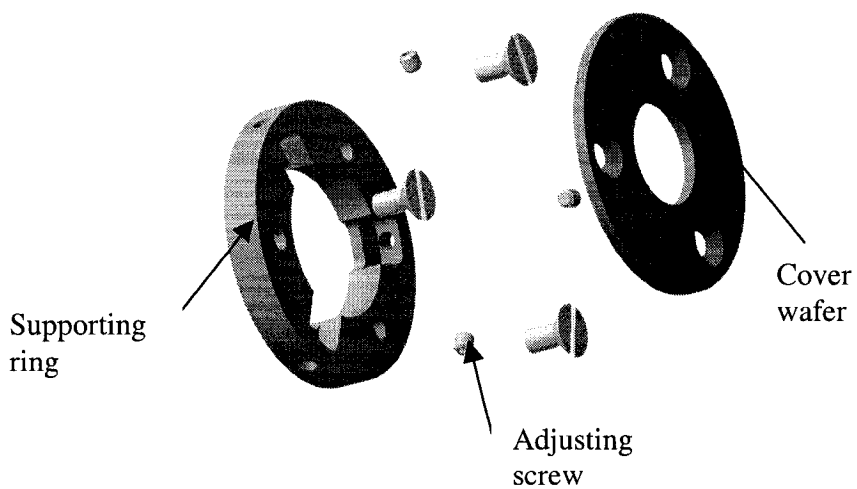

Figure 3.17 Exploded view of supporting ring assembly

3.7 Break assembly design

The break assembly consists of a tubular PZT stack (Figures 3.9 and 3.10), a compliant mechanism (Figures 3.11 and 3.12), and a pre-load mechanism, which includes a cylinder with two end nuts and Belleville spring washers. When there is no voltage applied on PZT stack or –200 voltages applied on PZT stack, the clamping arms will grip the center shaft under pre-load pressure produced by Belleville spring washers. Since PZT stack will contract under –200 voltages, the holding force will be almost double compared with no power. The compressive spring preload eliminates clearance between PZT stack and compliant mechanism, inherently compensates for temperature changes and wear and creates a reliable holding force when power is removed. The pre-compressive load is also important to prevent damage of PZT stack due to pulling force since the piezoelectric material cannot withstand large extension and shear stresses although it has high compressive resistance. After completing whole brake assembly design, a clash examination has to be conducted to examine that all dimensions of parts and assembly method are correct. Figure 3.18 demonstrates an example to examine whether the three clamping arms contact with center shaft. The brake assembly model and its fabricated prototype are shown in Figure 3.19, and the exploded view of brake assembly is shown in Figure 3.20.

Figure 3.18 Clash examination of three clamping arms with shaft

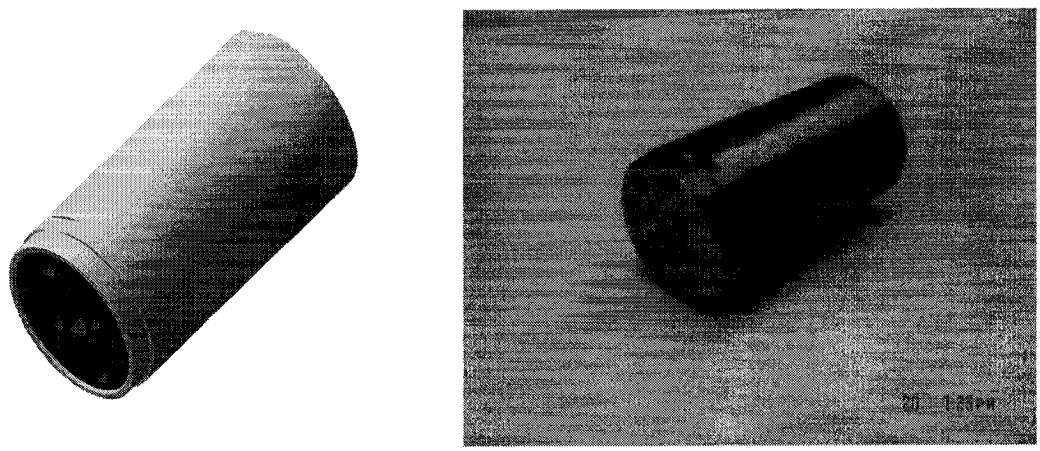

Figure 3.19 Prototype of brake assembly

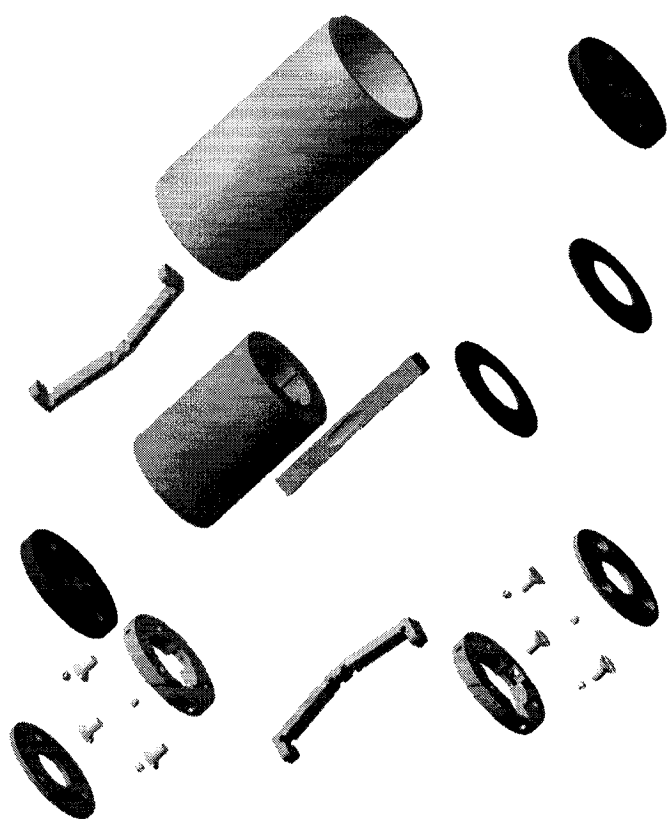

Figure 3.20 Exploded view of brake assembly

3.8 Pre-load spring system design

Since Belleville spring washers are especially suited for high loads in small spaces, they have been selected in the pre-load mechanism. By combining them in varying sequence as shown in Figure 3.21, the numerous load-carrying possibilities can be obtained. Typical load-deflection curves for three characteristic proportions of washers are shown in Figure 3.22. The dimensions and characteristics of Belleville Spring Washers, which could be used in the prototype of braking assembly, are listed in Table 3.1. By controlling the numbers and configuration of spring washers and the rotation angle of end nut, the stiffness of spring set and defined pre-load could be applied on the braking assembly. In this design, since the blocked force of PZT stack produced by Sensor Technology Ltd. are lower than of requested block force obtained from simulation (due to problem in assembling of the thin wafers), B1750-057 Belleville spring washers, which has lower stiffness, are used instead of B1750-085.

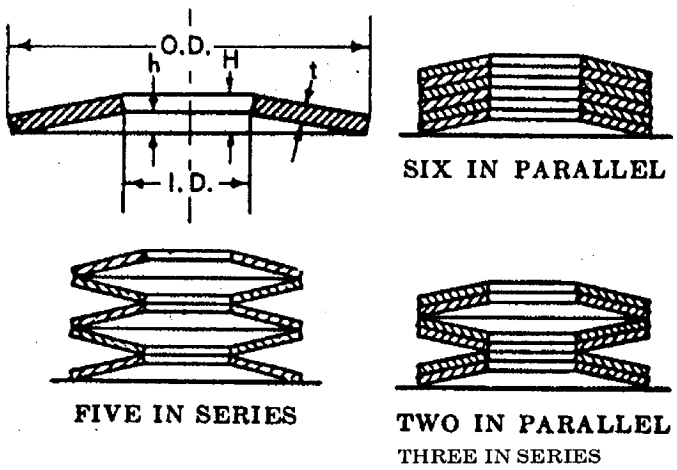

Figure 3.21 Different arrangements of spring wafers [60]

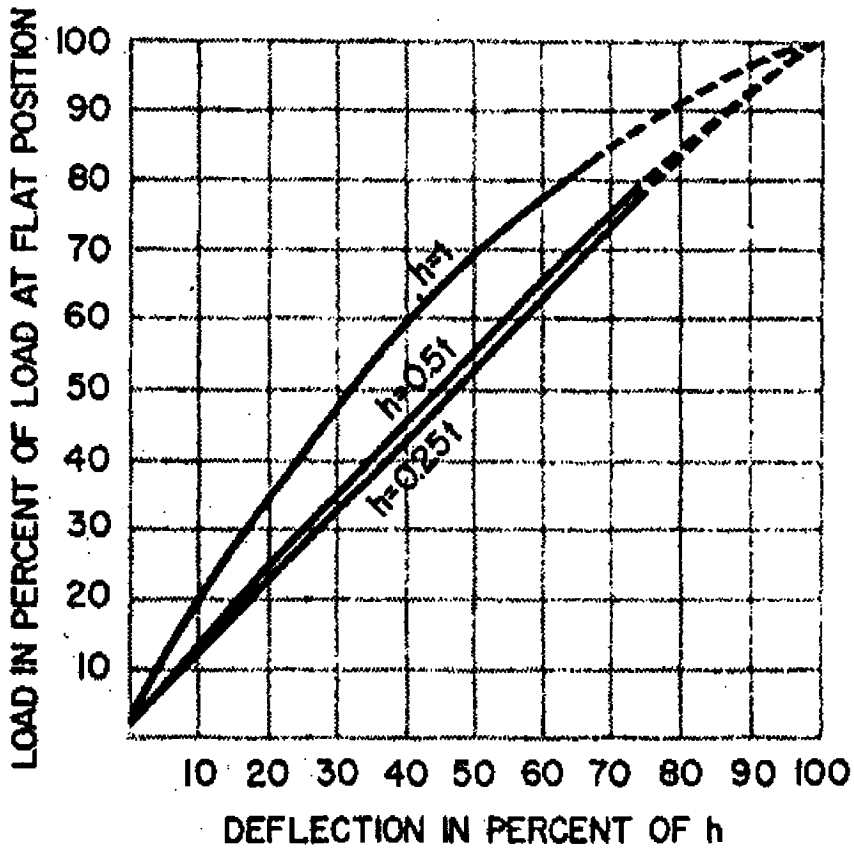

Figure 3.22 Load-deflection curves of Belleville spring washers [60]

Table 3.1 The dimensions and characteristics of Belleville spring washers [60]

CATALOG NUMBER	Minimum I.D. (mm)	Maximum O.D. (mm)	Stock thickness, t (mm)	H (approx) (mm)	H_1 (mm)	P_1 (N)	P (N)
B1750-057	22.5	44.45	1.45	2.90	2.16	1802-2202	2891
B1750-085	22.35	44.45	2.16	3.25	2.69	3643-4453	7251

Note: P_1 is the load at H_1

P is the load calculated at flat position

h=H-t

From examination of the curves in Figure 3.22, it can be realized that the stiffness of spring washer is not a constant when h=t, however the curve between 10 to 40 deflection in percent of h can be approximated as linear line, where the stiffness is about 2658 N/mm for B1750-057 . Since the thread pitch of the nut is 1 mm, when the axial displacement of nut is 0.145mm to 0.58mm, the relevant rotation angle of nut is 52 ° to 209 ° .

The cylinder should contain the compliant mechanism with tubular PZT stack and the pre-load system. It should be considered when designing the end nut how the wires of PZT stacks could go through the nuts and how a large torque could be applied on the nut. Four holes are designed for these applications.

In order to reduce the deflections of cylinder and nuts under large pre-compressive load, stainless steel 304 has been used in the prototype.

3.9 Extension assembly design

The extension assembly consists of a tubular PZT stack, a thin wall aluminum cylinder and two nuts. Figure 3.23 shows the model and prototype of extension assembly.

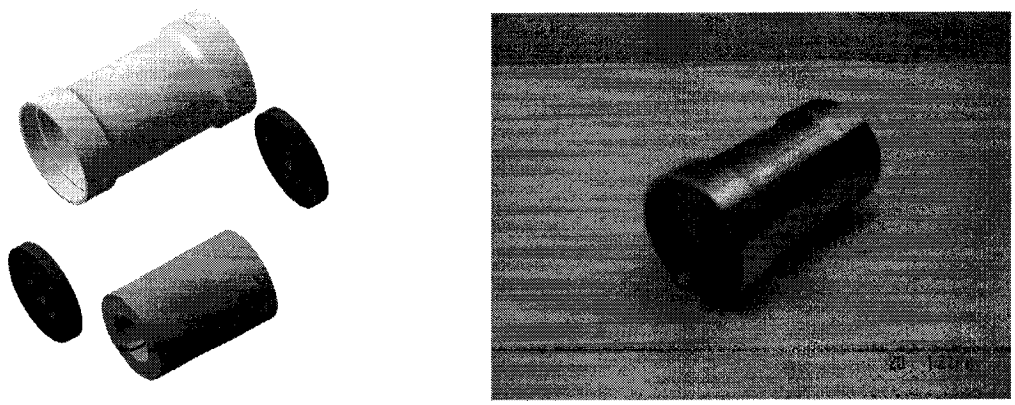

Figure 3.23 Extension assembly and its Prototype

The thickness of cylinder wall has been decided by FEA, which will be presented in Chapter 4. In order to increase the displacement of each step of inchworm actuator, the thickness of cylinder should be as thin as possible. However it should have enough bending and extension stiffness in order to prevent buckling. The extension cylinder also supplies the necessary pre-load on the PZT stack. The material of extension cylinder is selected to be Aluminum 6061.

3.10 Summary

The concept and detailed design of inchworm-type actuator were presented in this chapter. The actuator consists of three main subassemblies, which includes two clamping devices and one extension device. The clamping device consists of a tubular PZT stack, a compliant mechanism with flexible hinges and a pre-load mechanism. The central expanding device consists of a tubular PZT stack and a thin-walled aluminum cylinder to provide extension-contraction motion. Since PZT stacks were applied as driven element for clamping devices and extension device, the design of PZT stack considering the pre-load force was presented in detail. The main achievement is the compliant mechanism design, which includes three identical clamping arms and two supporting rings. The compliant mechanism amplifies the displacement produced by PZT stack and clamps the shaft by friction. By using adjusting screws located at supporting ring, the clamping arms could be adjusted to reduce the clearance between the clamping arms and the shaft. The whole actuator, its subassemblies and components were modeled in 3D by using CATIA, and the interference checking has been conducted before manufacturing. All the drawings of designs have been attached in Appendix C. The design optimization of the clamping arm and the finite element simulation will be introduced in the next chapter.

CHAPTER 4 FINITE ELEMENT MODEL AND ANALYSIS

4.1 Introduction

Finite element method (FEM) has been becoming more and more important since the 1970s with the development of computer technology. It is the most useful and powerful tool for engineers and scientists to analyze and optimize the engineering structures before the prototype fabrication and experiments. The concurrent engineering concept is based on the digital simulation using computer including computer-aided design (CAD), computer-aided engineering (CAE), computer-aided manufacturing (CAM), and product data management (PDM). There are several kinds of integrated software to realize concurrent engineering object such as CATIA, PRO/ENGINEER, UNIGRAPHICS, I-DEAS. Each of these software packages can perform simple finite element analysis (FEA), however for more elaborated and professional FEA, MSC_NASTRAN and ANSYS are the suitable choices. Since ANSYS has special elements and functions in its library of elements to perform multidisciplinary analysis involving electrical and mechanical coupling such as piezoelectric analysis, ANSYS has been selected to carry out the finite element analysis of the total actuator and the optimization of its flexible clamps.

As mentioned in Chapter 1, the working principle of the inchworm-type actuator is based on the three piezoelectric elements that contract and expand in a well-defined order and thus drive a shaft linearly. The stroke of one single cycle is limited by the length and the maximum piezoelectric strain of the central device, while the clamping force of the clamping devices and the coefficient of friction between them and the shaft determine the holding and thrust force of the actuator. The no-load velocity is limited by the step size and the maximum operational frequency. Using FEA, the extensive stress analysis and design optimization have been carried out in order to improve the design before the prototype is fabricated.

In order to simplify the problem, some assumptions have to be made when using FEA to analyze the components of piezoelectric inchworm-type actuator.

- Linear properties: All the analysis will be linear analysis although piezoelectric material BM532 has some hysteresis (about 8-12%) in its displacement / voltage.
- The epoxy glue layers and the metal shims between each PZT ceramic wafers in the PZT stacks will not be considered in the PZT stack finite element model.
- Quasi-static analysis: As a preliminary design, all analysis will be quasi-static which means that inertial forces and damping will be neglected.
- Room constant temperature: Normally piezoelectric materials properties are temperature dependent, this dependency will introduce another discipline (thermal) which makes the analysis (electrical-mechanical–thermal coupling analysis) much more complex. In this study, by using a material with low coefficient of thermal expansion such as stainless steel, accommodating pre-load spring wafers and designing adjustable support ring, the effects of thermal deflection will be reduced. Thus, thermal effect will not be considered.
- Rigid boundary conditions: Since the contact stiffness of components are high compared with flexure clamps, they will be treated as rigid boundaries.

4.2 Flexible clamp analysis and optimization

Since the development of a robust clamping mechanism is essential to realize the high force capability, a considerable design effort has been focused on optimizing the clamping device to increase the output force and ANSYS has been used to analyze and optimize the performance of the flexible clamps. Since a two-dimensional model will represent a substantial time saving over a three dimensional one, first a 2D parameterized FEA model has been created in order to find the optimum geometry and the sensitivities of

the involved parameters. This 2D model will also provide a basis platform to better realize and also verify the later established 3D model. Based on the 2D model, a complex 3D parameterized FEA model of the flexible clamping mechanism has been built in order to perform the detailed stress analysis and to accurately obtain the optimized parameters of the flexible clamp. The material of clamp is stainless steel 304 , which has the following material properties[61]:

Modulus of Elasticity E=193 GPa ;

Poisson's ratio $\gamma = 0.29$;

Yield Tensile Strength= 215 MPa;

Ultimate Tensile Strength = 505 MPa ;

4.2.1 Two dimensional analysis

As a preliminary investigation, a 2D parameterized model has been built which includes all possible design parameters. Due to the symmetry of the clamp, only one half–model (Figure 4.1) has been used for the design optimization using the finite element method. The design parameters considered in this investigation are shown in the Figure 4.1. It is noted that the thickness in Z direction is 8 mm.

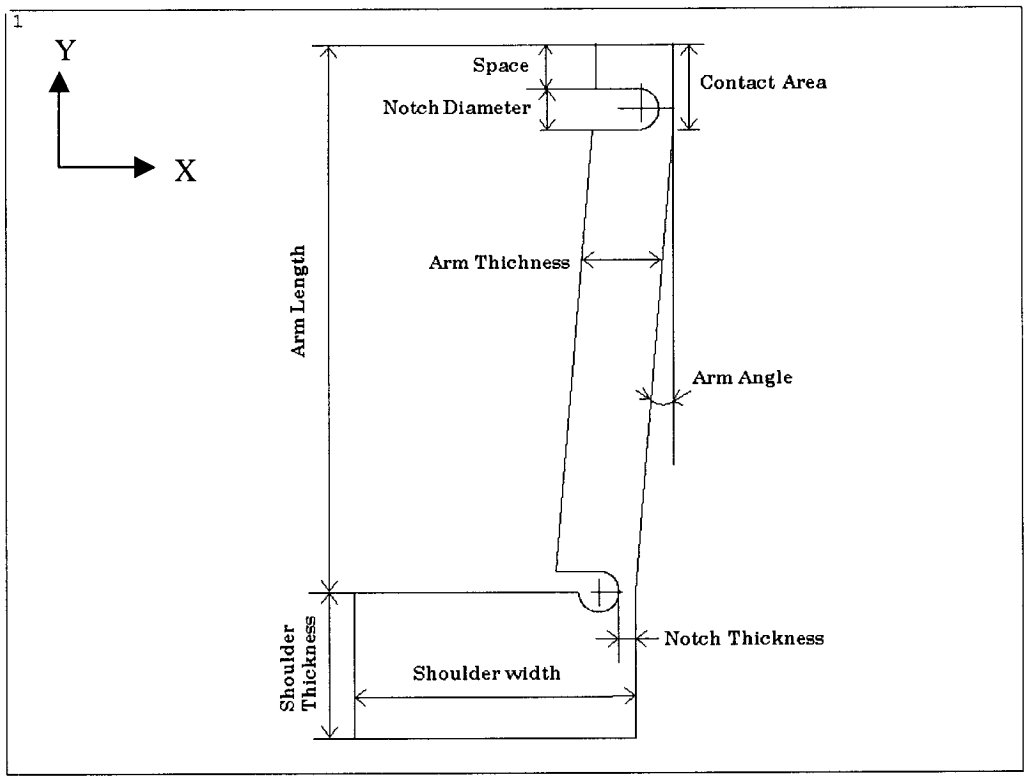

Figure 4.1 Contour of flexible clamp

4.2.1.1 Contact analysis

Since the main objective of the flexible clamp is to clutch the shaft, thus the normal contact force will be an important parameter. Considering this, the contact analysis has been carried out in order to find the displacement, normal contact force, and maximum von Misses stress of flexible clamp. It is assumed that the supposing shaft is rigid, thus it will be treated as a rigid target surface. Frictional coefficient μ is also considered to be 0.2.

Employing elements PLANE82 to construct the flexible clamp main body, TARGE 179 to model the target rigid shaft surface, and CONTA 172 to model the flexible clamp contact area, an efficient finite element model suitable for the contact analysis has been established. At the bottom of the flexible clamp, a vertical displacement of U_y =10 μm has been applied. The generated mesh, applied boundary conditions and vertical displacement

are shown in Figure 4.2. After 6 substeps and 18 cumulative iteration, the results are listed in Table 4.1. The reaction force measured at the top of the clamp can be used to find the stiffness of the flexible clamp. The normal force is the clamping force normal to the contact surface. Figure 4.3 demonstrates the deflection and stress in the vicinity of the contact area.

In order to reduce the computational time, a simplified model based on the fixed boundary condition instead of contact condition has been considered. The relevant results are shown in the Table 4.1. and Figure 4.4-4.5. Examination of the Table 4.1 reveals that good agreement exists between the simplified and contact model. The difference between the contact analysis and the simplified analysis is lower than 6% . Therefore the simplified boundary condition model will be used in the following optimization process.

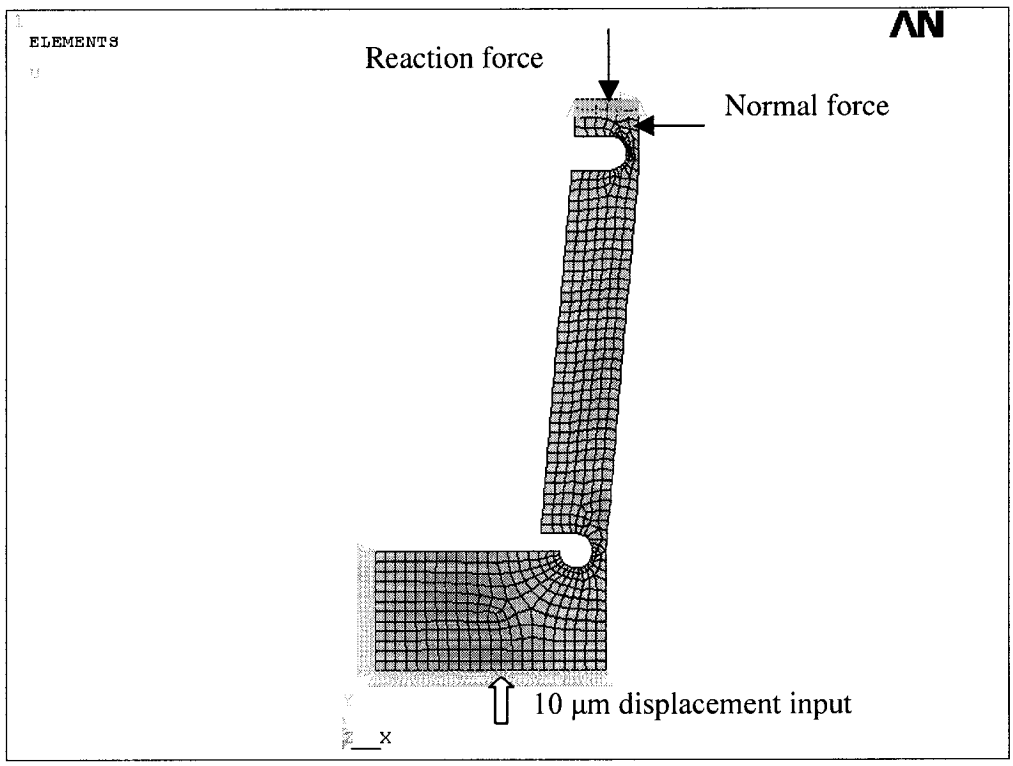

Figure 4.2 Boundary condition and mesh of flexible clamp

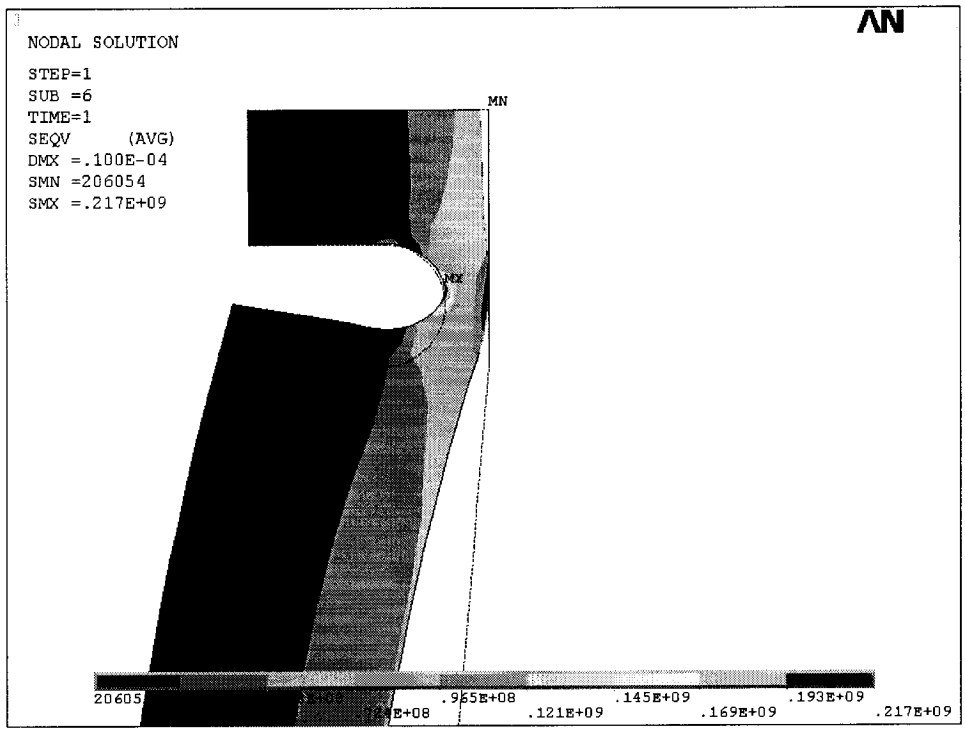

Figure 4.3 Deflection and stress in the vicinity of the contact area

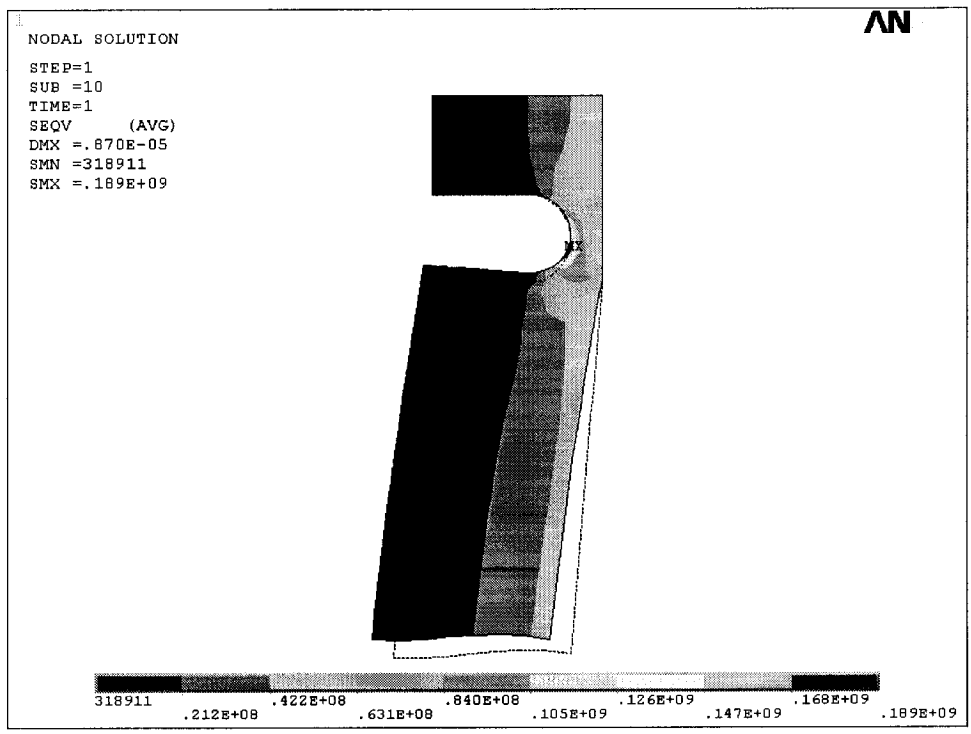

Figure 4.4 Local deflection and stress of simplified model

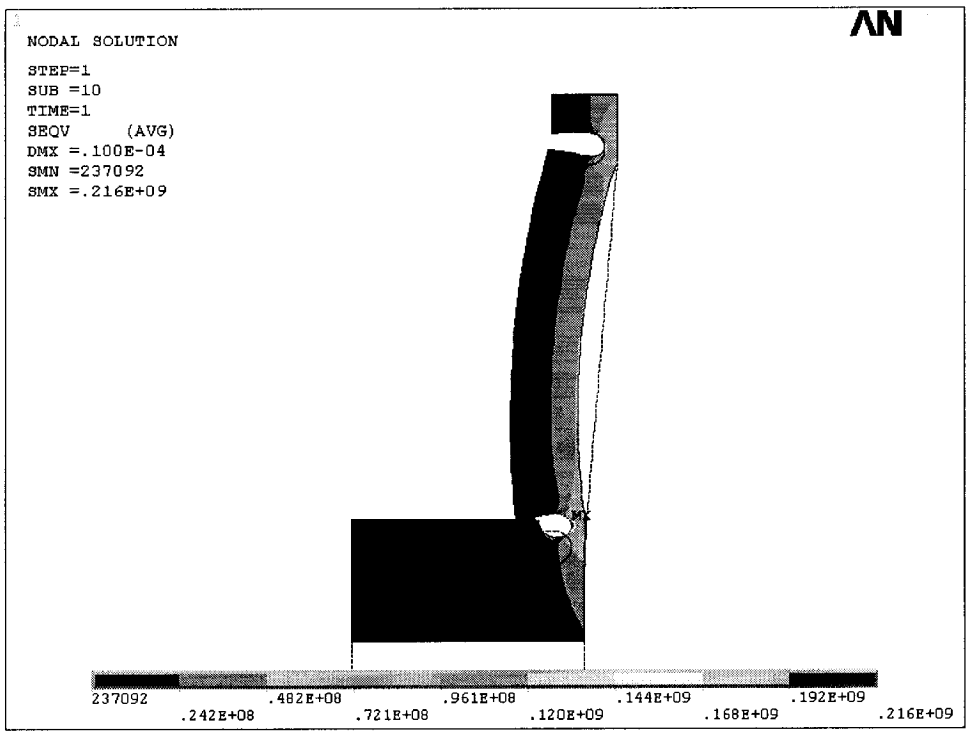

Figure 4.5 Deflection and stress of simplified model

Table 4.1 Comparison between contact analysis and simplified analysis

	Reaction force (N)	Normal force(N)	Friction force (N)	Max stress at upper notch (MPa)	Max stress at lower notch (MPa)
Contact	605	53	11	217	210
Simplified	617	50	10	189	216

4.2.1.2 Design parameters and geometry optimization of 2D model

The objective of the design optimization is to maximize the clamping force or normal force with suitable displacement amplification and to minimize the maximum stress in the flexible clamp. The displacement amplification factor is defined as:

d.a.=output displacement / input displacement (4-1)

Figure 4.6 shows the output displacement due to the input displacement.

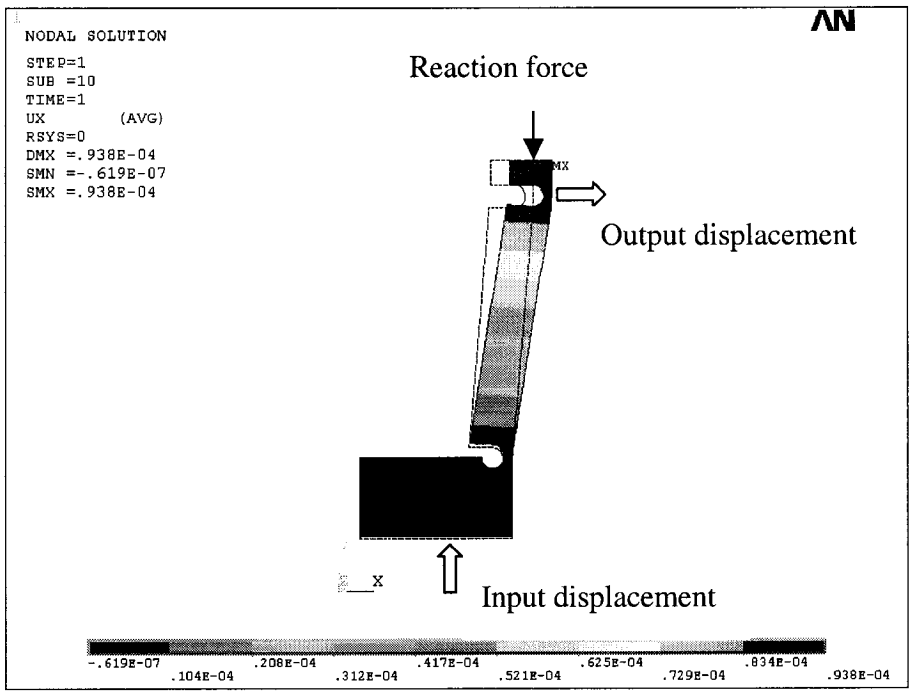

Figure 4.6 Displacement amplification

Since the input displacement is always set as 10 μm, the output displacement is the parameter, which presents the d.a. In order to conduct the optimization, an ANSYS input file has to be first created, which contains the complete analysis sequence including preprocessing, solution, and post processing. The input analysis file must contain a parametrical defined model. In other words, all inputs and outputs containing design variables, state variables and objective function should be defined parametrically. In the following the design variables, state variables and objective function are itemized.

- The initial design variables shown in Figure 4.1and their associated range (side constraints) are defined as:

  AA: Arm Angle (2^{o}-15^{o})

  AT: Arm Thickness (3mm-6mm)

  AL: Arm Length (30mm-40mm)

ND: Notch Diameter (1mm-5mm)

NT: Notch Thickness (0.5mm-2.5mm)

SPACE: Wall Thickness of upper notch

- The state variables and their associated side constraints are described as:

  Range: Output displacement of contact area > 25 μm

  NormalF0: The normal force acted on the contact area >50 N

  SMACFIX: Maximum von Misses stress for fixed contact area < 200MPa

  SMAXFREE: Maximum von Misses stress for free contact area< 200MPa

- The objective function is defined as 1-ETOT

  ETOT: Total potential energy

Since it is desired to increase both the normal clamping force and displacement amplification factor, the maximization of the total potential energy of the flexible clamping is a suitable objective function.

Because input displacement will be applied on the whole bottom of the clamp shoulder, the shoulder width and thickness have not been considered as design parameters. Sweep Generation optimization method [62] is used to study the overall design space. The method varies one design variable at a time over its full range using the uniform design variable increments and establishes the global variational evaluations of the design variables, the state variables and the objective function. The results are plotted in Figures 4.7-4.11. The vertical axis demonstrates the actual values for the state variable or the objective function while the horizontal axis shows the normalized values of the design variables(varying between 0 and 1), where 0 corresponds to its minimum value and 1 to its maximum.

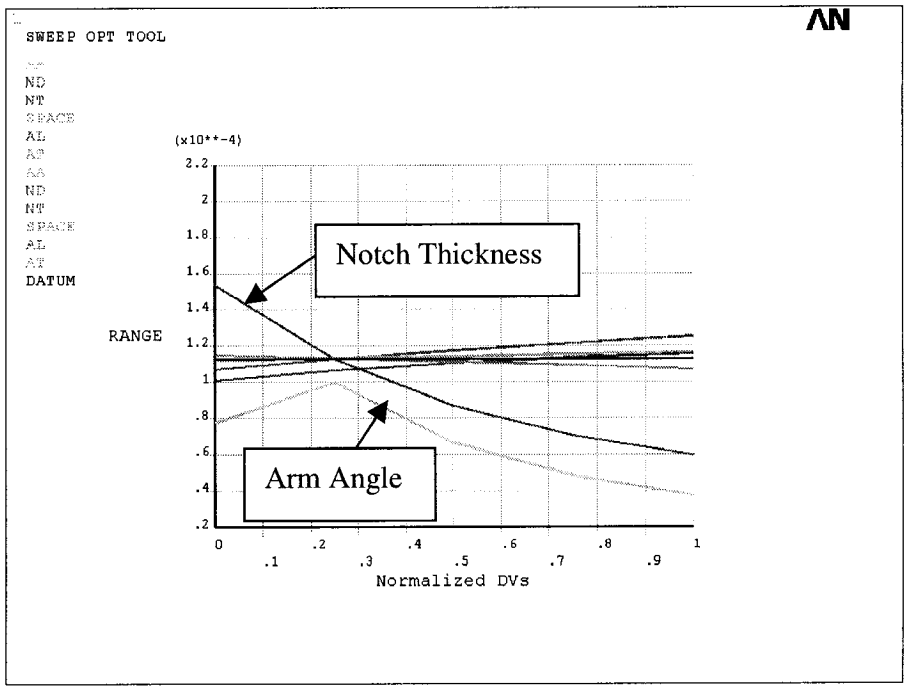

Figure 4.7 Design variables vs. Range in 2D model

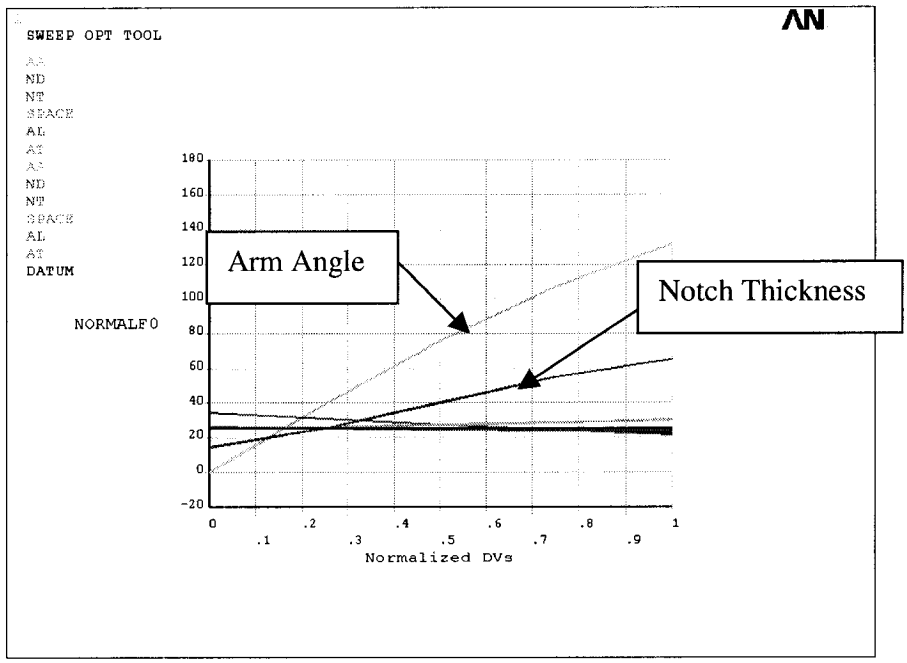

Figure 4.8 Design variables vs. Normal force in 2D model

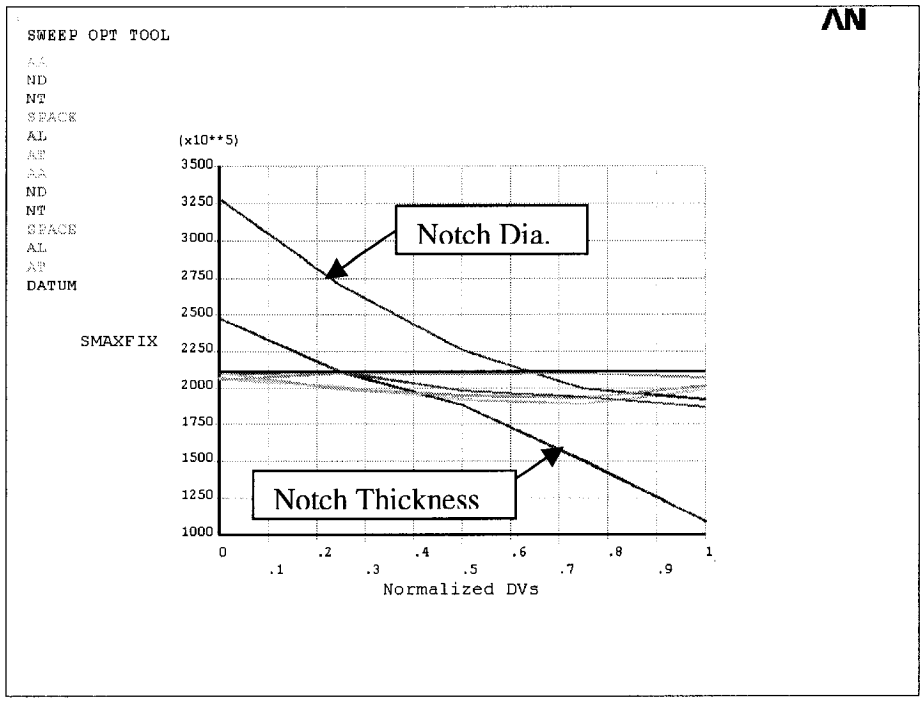

Figure 4.9 Design variables vs. Max stress for fixed contact area in 2D model

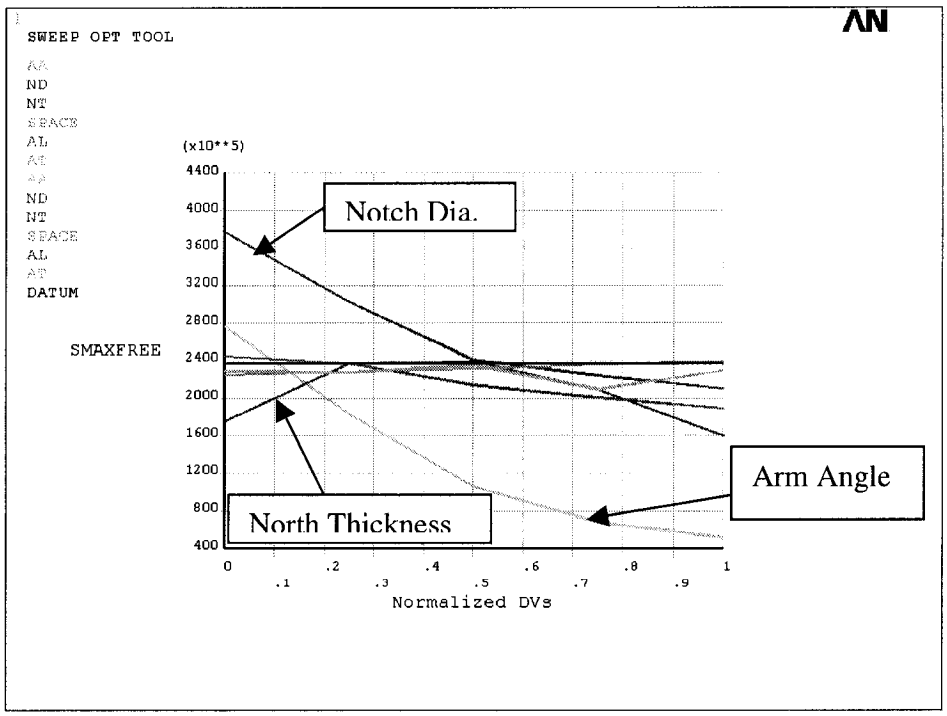

Figure 4.10 Design variables vs. Max stress for free contact area in 2D model.

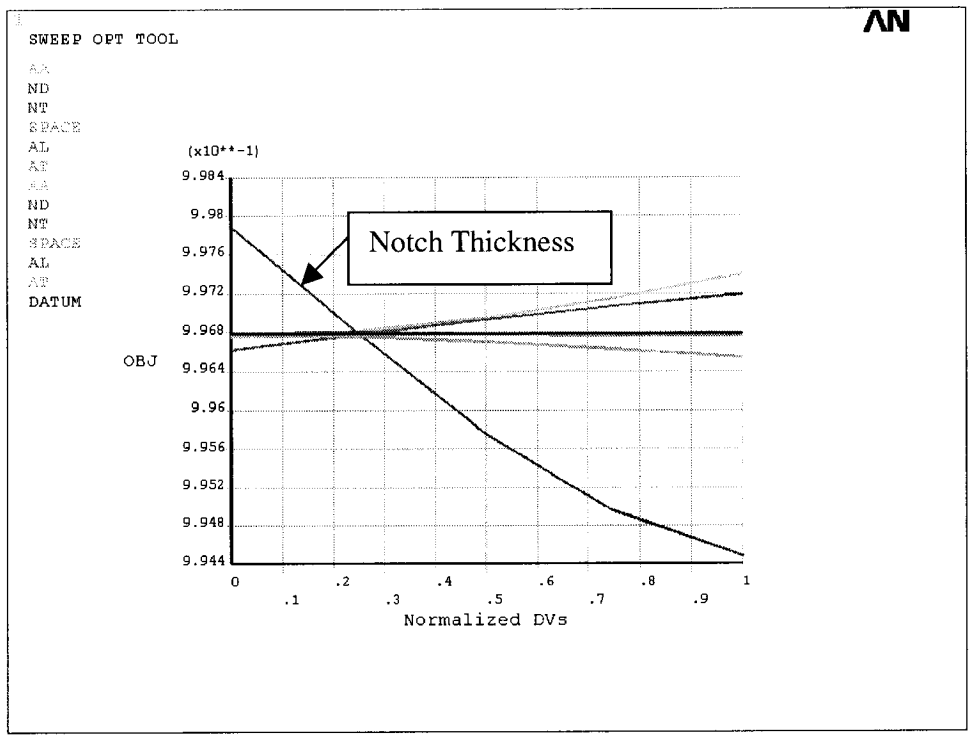

Figure 4.11 Design variables vs. objective function in 2D model

A close examination of the results obtained from the above preliminary optimization reveals that the design parameters SPACE, Arm length (AL) and Arm thickness (AT) have insignificant influence on the performance of flexible clamp. It is noted that to obtain large clamping force with suitable range and stress, some compromise should be made among Arm Angle, Notch Thickness and Notch Diameter. This issue will be addressed in the design optimization of the detailed 3D model of the flexible clamp.

4.2.2 Three dimensional analysis

Three-dimensional analysis is required to obtain more accurate results. A 3D parametric finite element model of the clamp (half part) has been developed as shown in

Figure 4.12. Element Solid 92 has been employed to model the whole body of the flexible clamp. The length of clamp is 33.75 mm, which is half of the length of PZT stack plus the thickness of support slot. The shoulder width and thickness are decided by the diameters of PZT stack and the dimensions of the support ring. Support ring and cover wafer will prevent shoulder from bending. The SPACE is set as 2 mm. The diameter of center shaft is 8 mm. In order to increase the contact area between the clamps and the shaft, a circular concave has been cut out from the contact surface of clamp. The depth of the concave is 0.93mm. To reduce the number of design parameters, the clamp thickness has been represented by the Notch Thickness and Notch Diameter as:

$$AT=ND/2 +NT \qquad (4\text{-}2)$$

Similar to 2D optimization, the contact area boundary condition will also be replaced by the fixing boundary condition in the three dimensional optimization. The displacement input applied to the bottom face of the clamp is set to 10 μm in upward vertical direction. The stress distribution in the deflected clamp under this applied displacement is shown in Figure 4.13. A maximum von Misses stress of 170 MPa for fixed contact area and output horizontal displacement of 57 μm have been obtained. In order to study the stiffness of the clamp, input stiffness and output stiffness are introduced as state variables. The design variables, state variables and objective functions are listed as follows and their associated lower and upper bounds are tabulated in Table 4.2.

- **State variables: (SV)**

  Range: The free displacement of the contact area in the x direction

  NormalF0: The normal force acting on the shaft (clamping force)

  SMAXFIX: Maximum von Misses stress on the clamp for fixed contact area

SMAXFREE: Maximum von Misses stress on the clamp for free contact area

$K_{y\,fix}$: Input stiffness of half-clamp when contact area is fixed

$K_{y\,free}$: Input stiffness of half-clamp when contact area is free

K_x: Output stiffness of half-clamp (Kx = NormalF0/ range)

- **Design variables: (DV)**

AA: Arm Angle

AT: Arm Thickness AT= ND/2+NT,

ND: Notch Diameter

NT: Notch Thickness

- **Objective function: (OBJ)**

OBJ = 1- ETOT: Total potential energy in the deflected clamp.

Table 4.2 Design and control variables and their change range in optimization

NAME	TYPE	MIN	MAX	TOLERANCE
RANGE	SV	0.250000E-04	None	0.565590E-06
NORMALF0	SV	70.0000	None	0.700000
SMAXFREE	SV	None	0.200000E+09	0.200000E+07
SMAXFIX	SV	None	0.200000E+09	0.200000E+07
KYFREE	SV	0.140000E+08	None	140000.
KYFIX	SV	0.100000E+09	None	0.100000E+07
KX	SV	0.200000E+07	None	28000.0
AA	DV	2.00000	15.0000	0.130000
ND	DV	0.100000E-02	0.400000E-02	0.400000E-04
NT	DV	0.125000E-02	0.200000E-02	0.200000E-04
OBJ	OBJ			0.994838E-02

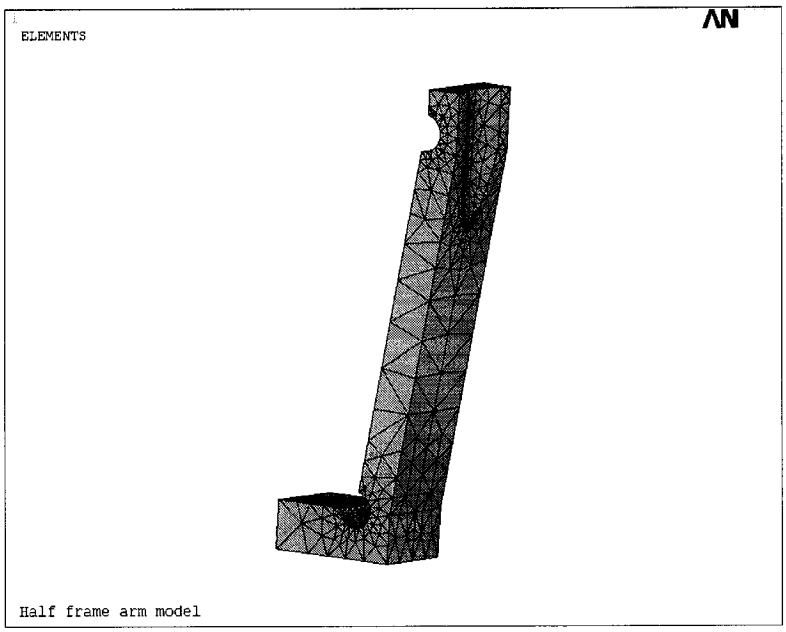

Figure4.12 3D Finite element model of the clamp (half part)

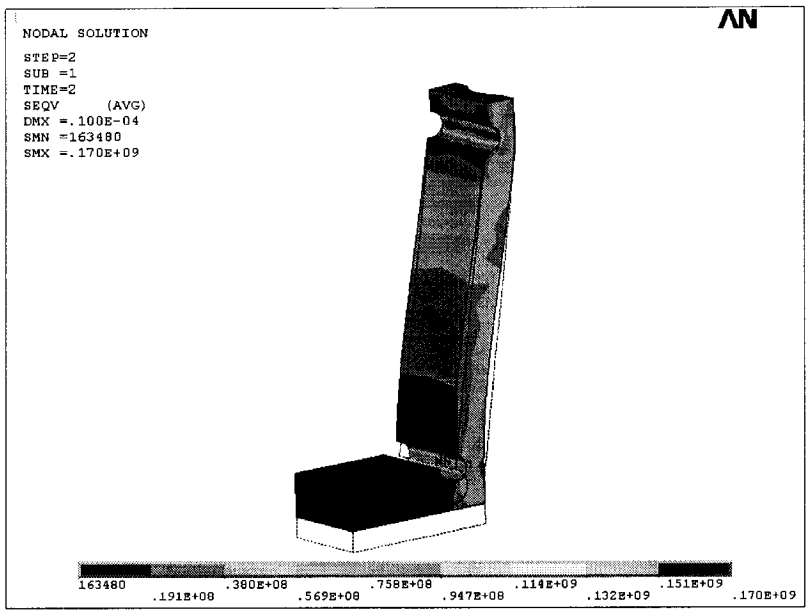

Figure 4.13 Stress and deflection of clamp for fixed contact area in 3D model

Using the sweep tool and the subproblem approximation method [62] in ANSYS the optimization has been carried out. The variation of the design variables versus the state variables and the objective function are shown in Figures 4.14-4.21.

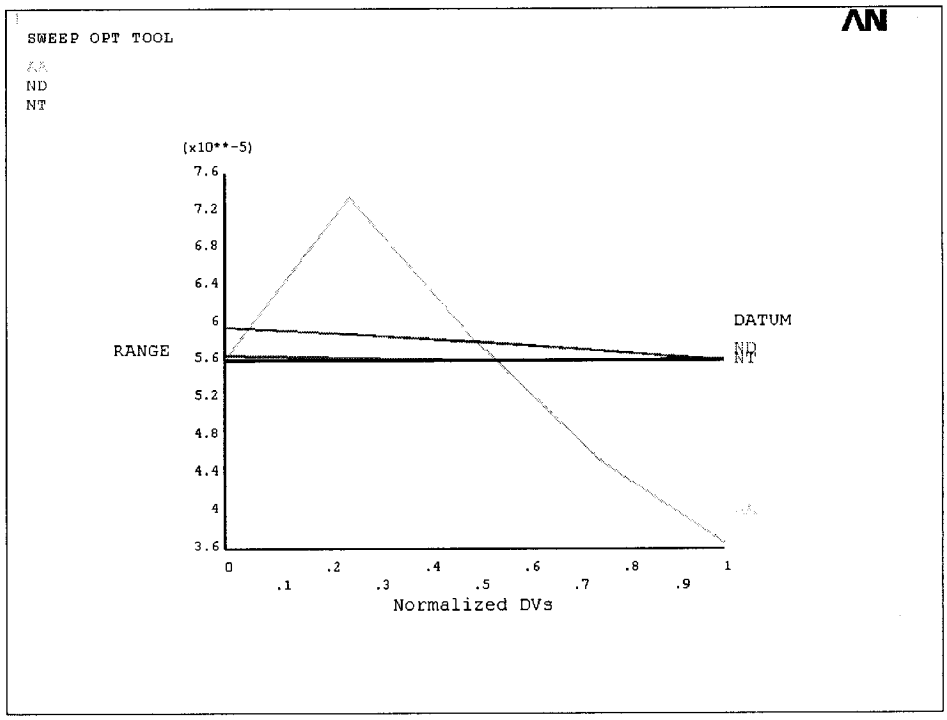

Figure 4.14 Design variables vs. range in 3D model

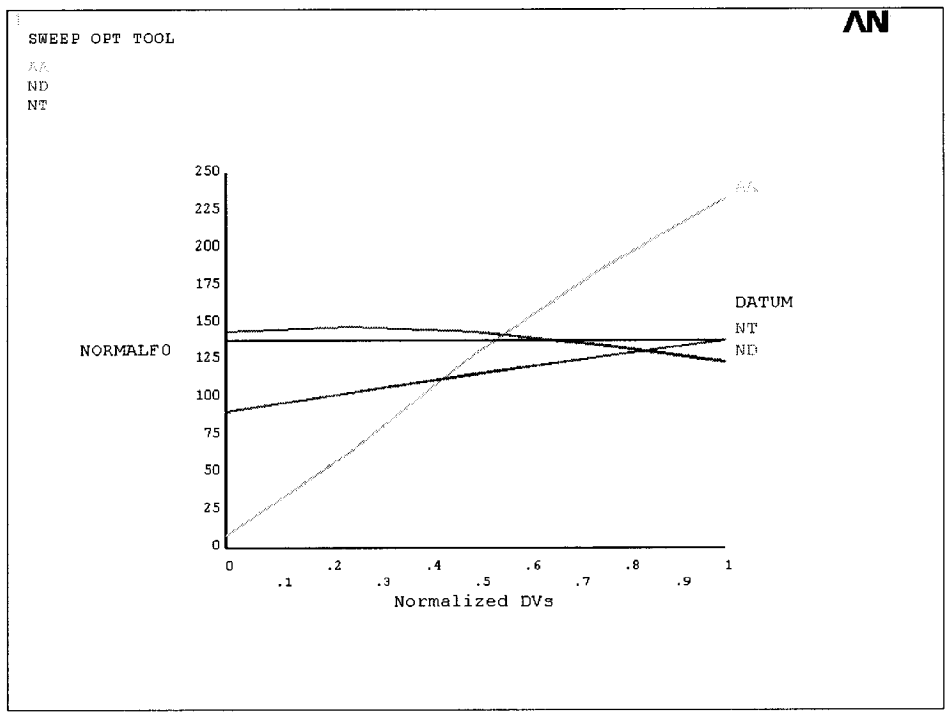

Figure 4.15 Design variables vs. normal force in 3D model

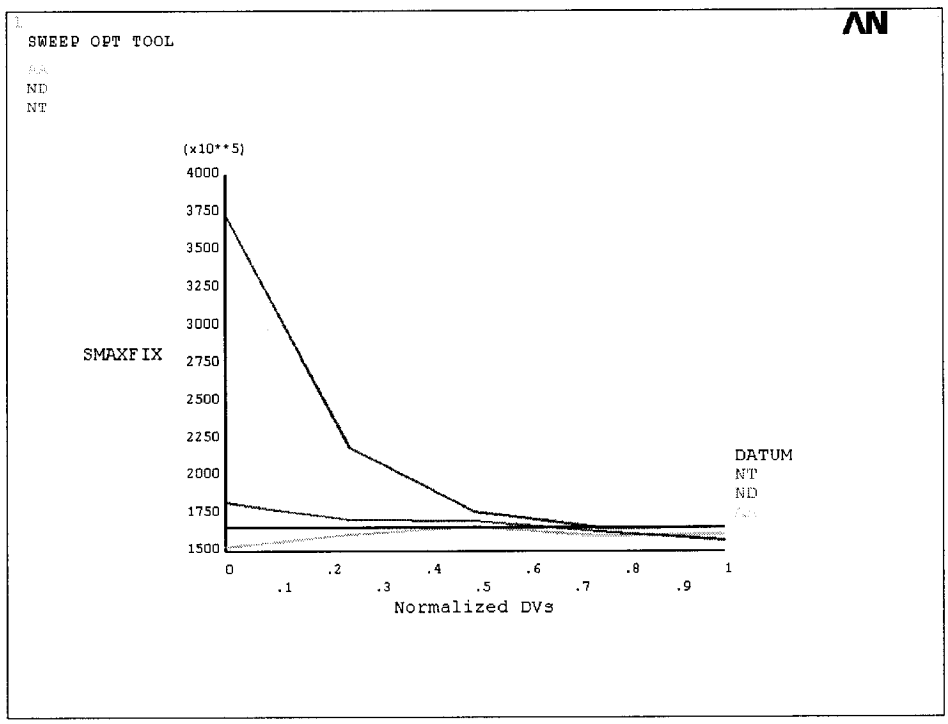

Figure 4.16 Design variables vs. max stress when contact area is fixed in 3D model

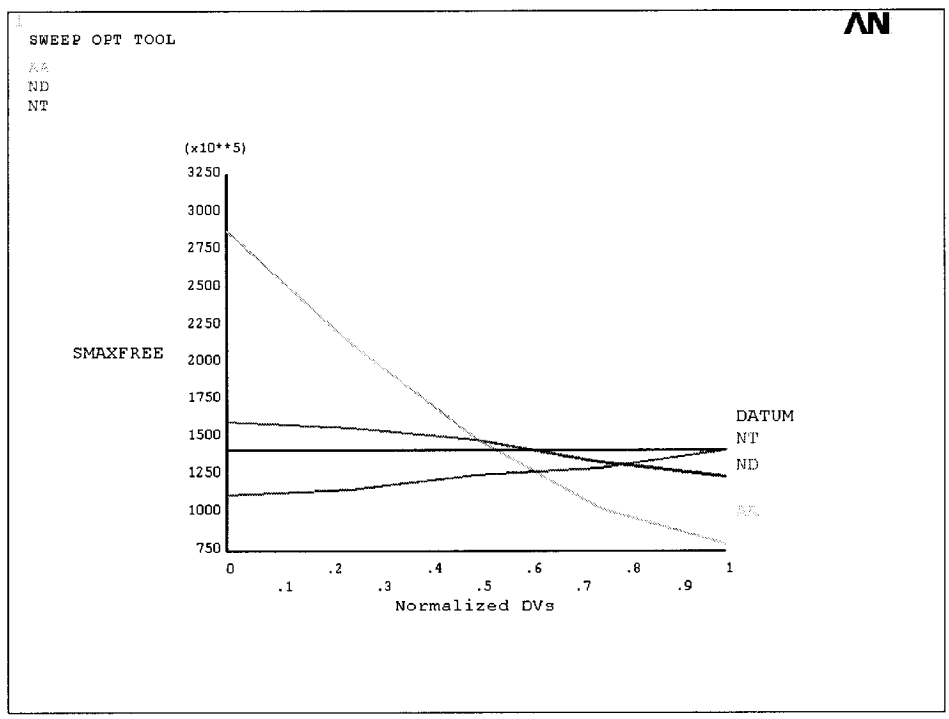

Figure 4.17 Design variables vs. max stress when contact area is free in 3D model

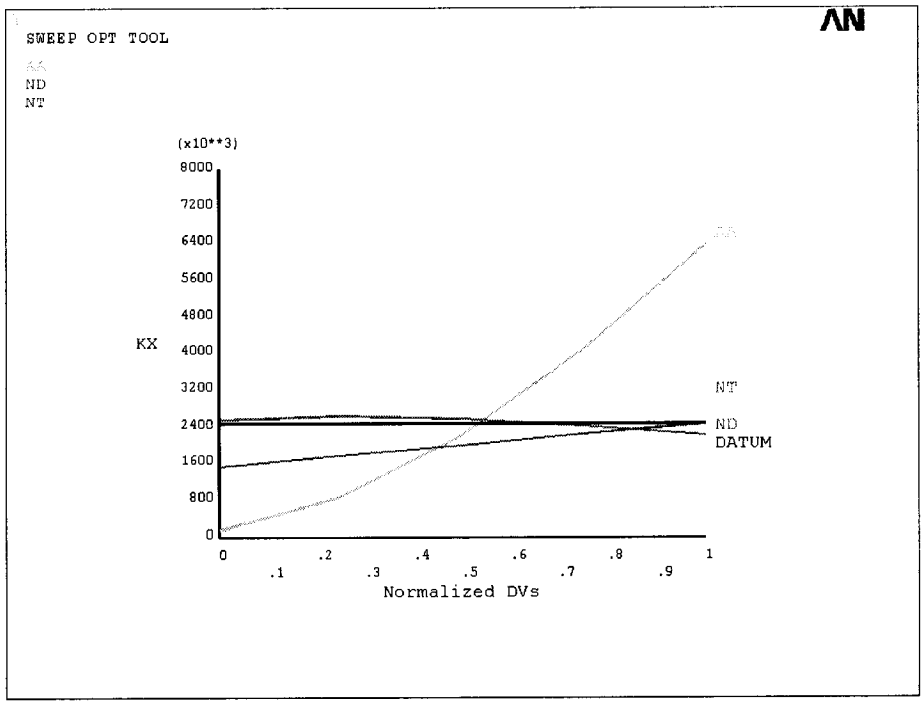

Figure 4.18 Design variables vs. output stiffness in 3D model

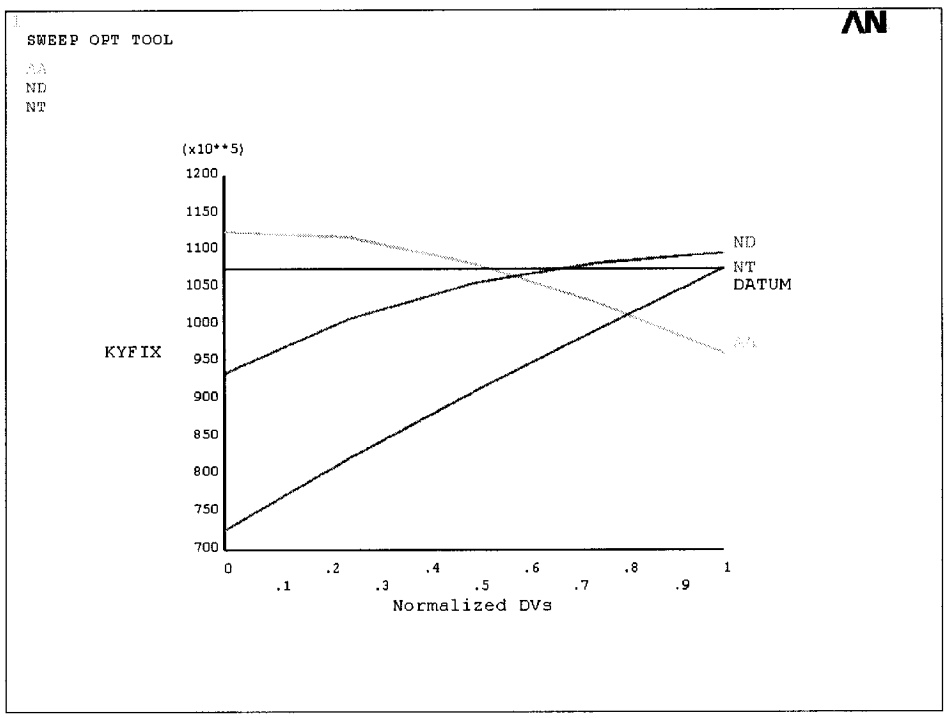

Figure 4.19 Design variables vs. input stiffness for fixed contact area in 3D model

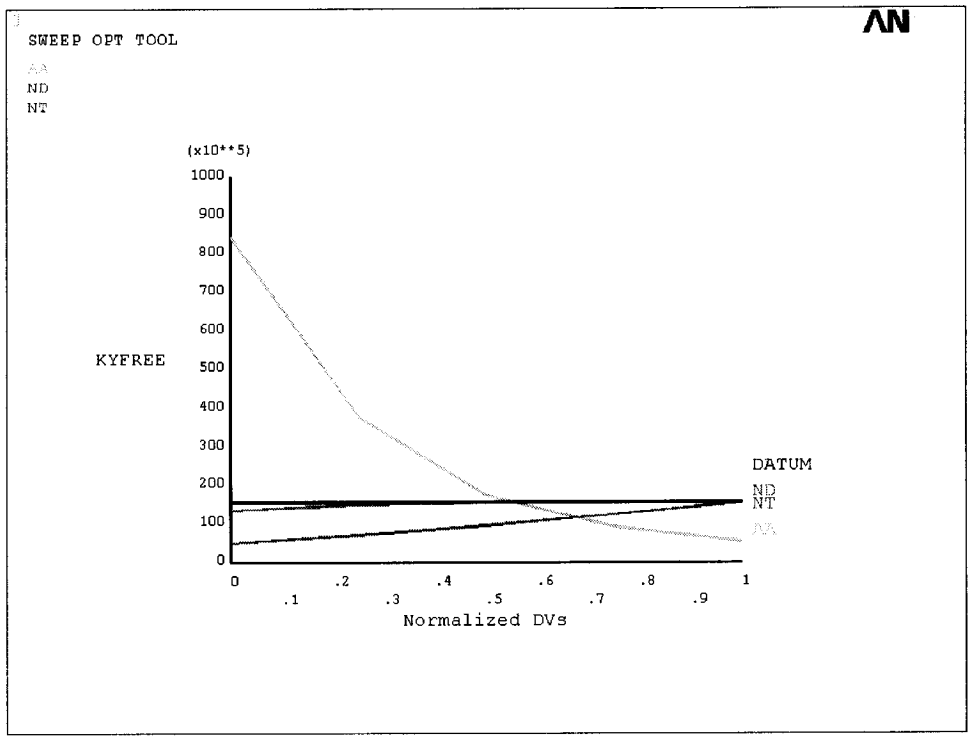

Figure 4.20 Design variables vs. input stiffness for free contact area in 3D model

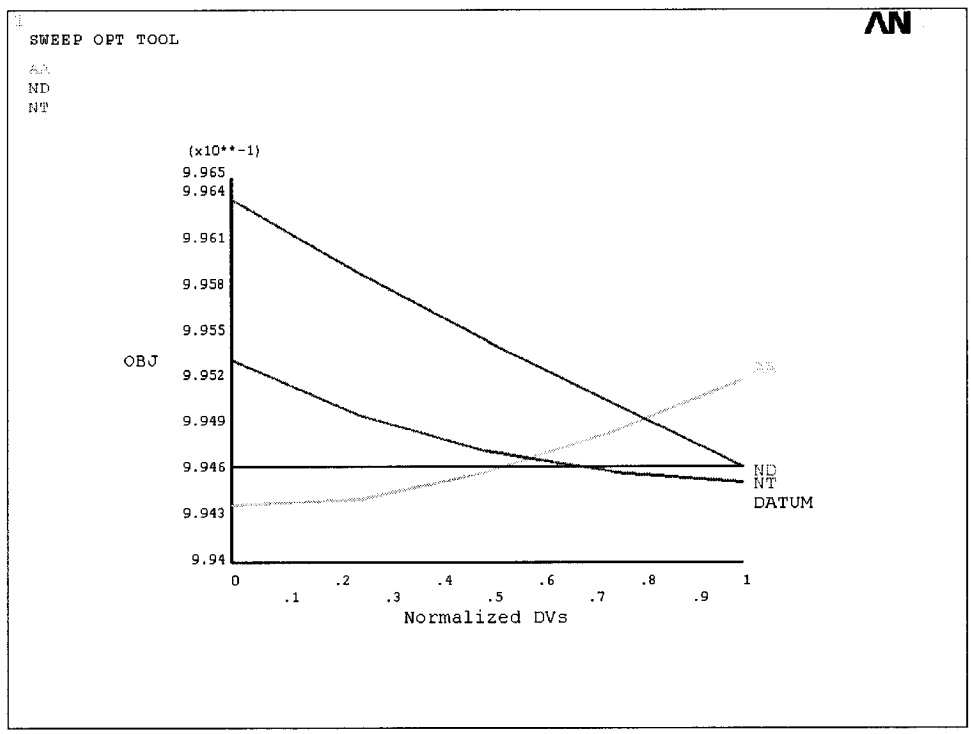

Figure 4.21 Design variables vs. objective function for 3D model

It is again noted that the input displacement of half-clamp is set at 10 μm. The optimized results are listed as follows

- Clamp design variables:

  AA=9°, AT= 3.4mm, ND=3mm, NT=1.9mm

- Clamp state variables:

  Range = 57 μm

  NormalF0 = 133 N

  SMAXFIX = 170 MPa, SMAXFREE = 137 MPa

  $K_{y\,free}$ = 14 N / μm , $K_{y\,fix}$ = 103 N / μm

  K_x = 2.333 N / μm

- Displacement Amplification :

  d.a.= range/input displacement=5.7

4.3 Calculation of compliant mechanism stiffness and reaction force

The displacement amplification factor, the input stiffness and output stiffness of the compliant mechanism are important parameters, which highly affect the performance of the compliant mechanism. Since the whole compliant mechanism consists of three flexible clamps, the output stiffness of compliant mechanism, K_{xc}, is six times of K_x obtained for half model of one clamp. Thus $K_{xc}=6\times2.333\cong14$ N/μm. Also the input stiffness K_{yc} is 3/2 times of K_y. Therefore, $K_{yc}=3/2*K_{yfix}\cong155$N/μm for zero clearance. The maximum input displacement depends on the displacement of PZT stack, δ_o, which is 13.5 μm.

The maximum input pressure force (PF), the clamping force (CF), holding force (HF)and output force (OF) of compliant mechanism for different values of the clearance between

clamp contact area and the shaft (CL), are listed in Table 4.3. Figure 4.22 also demonstrates the effect of clearance (CL) between the clamp and contact area on these forces .

Table 4.3 Forces change with clearances

CL (μm)	PF (N)	CF (N)	HF (N)	OF (N)
0.0	3090.0	797.9	159.6	79.8
25.4	2495.1	442.3	88.5	44.2
50.8	1900.2	86.8	17.4	8.7

It is noted that:

$PF = (CL/d.a.*K_{yfree}+(\delta_s - CL/d.a.)*K_{yfix})*3/2$ (4-3)

$CF = ((\delta_s /2 *d.a.) - CL)*K_x*6$ (4-4)

$HF = CF* \mu$ (4-5)

$OF = HF/2$ (4-6)

Coefficient of friction $\mu = 0.2$

Displacement of PZT stack under pre-load and applied - 200 voltage $\delta_s = 20$ μm

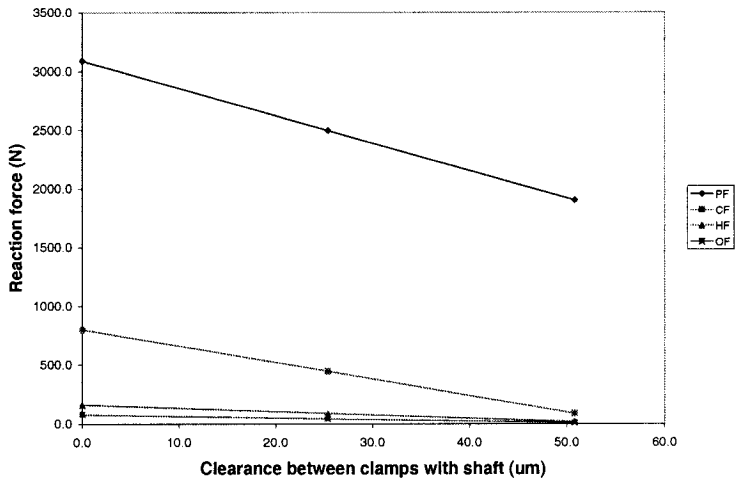

Figure 4.22 Force of compliant mechanism vs. clearance

The compliant mechanism undergoes two distinct conditions (one before contact and the other after the contact) when there is a clearance between the clamp contact area and the shaft. Let us assume the clearance is set at CL=25.4 μm, now referring to Section 4.2.2 the combined input stiffness curve of the compliant mechanism before the contact point and after the contact point shown in Figure 4.23.

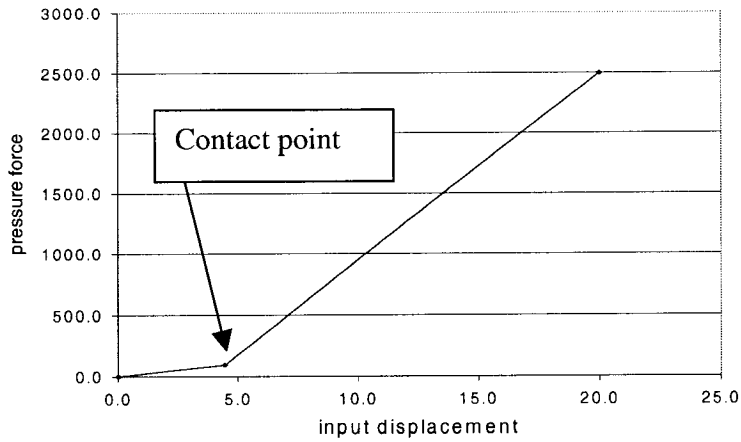

Figure 4.23 Axial stiffness of compliant mechanism for clearance of 25.4 μm

As it was expected the axial stiffness of the compliant mechanism abruptly changes after the contact occurs.

4.4 Displacement and reaction force of BM532 PZT tubular stack

Element Solid 5, which has the piezoelectric characteristics, has been employed to model the PZT stack. Element Solid 5 has eight nodes where each node has three structural displacement degrees of freedoms and one electrical voltage degree of freedom. According to the formulas introduced in Section 2.8, BM 532 material characteristics (Appendix B) is converted to ANSYS piezoelectric material input by executing the developed MATLAB Code (Appendix A). The ANSYS piezoelectric material input data is listed as follows:

- Relative permittivity matrix: i.e. Dielectric matrix (evaluated at constant strain, i.e. mechanically clamped):

$$[\varepsilon^S] = 1.0\text{e-}007 * \begin{vmatrix} 0.2876 & 0 & 0 \\ 0 & 0.2876 & 0 \\ 0 & 0 & 0.0836 \end{vmatrix} \quad (4\text{-}7)$$

- Piezoelectric matrix (relating stress/electric field strength) :

$$[e] = \begin{vmatrix} 0 & 0 & -7.7556 \\ 0 & 0 & -7.7556 \\ 0 & 0 & 26.2262 \\ 0 & 0 & 0 \\ 0 & 0 & 0 \\ 0 & 0 & 0 \end{vmatrix} \quad (4\text{-}8)$$

- Stiffness matrix evaluated at constant electric field strength, i.e. short circuit

$$[c^E] = 1.0e+011 * \begin{vmatrix} 1.3497 & 0.8167 & 0.7366 & 0 & 0 & 0 \\ 0.8167 & 1.3497 & 0.7366 & 0 & 0 & 0 \\ 0.7366 & 0.7366 & 1.0009 & 0 & 0 & 0 \\ 0 & 0 & 0 & 0.2665 & 0 & 0 \\ 0 & 0 & 0 & 0 & 0.2665 & 0 \\ 0 & 0 & 0 & 0 & 0 & 0.2665 \end{vmatrix} \quad (4\text{-}9)$$

The end displacements of the PZT stack when it is under 200 V and varying preload between 0 to 11060 N are provided in Table 4.4. The model and its associated boundary conditions is also shown in Figure 4.24.

Using ANSYS piezoelectric coupling calculation, the free displacement of 13.5 μm and the blocked force of 11060 N when the PZT stack is under 200 V have been obtained.

The contour plot of axial displacement of the tubular PZT stack when it is just under 200 V is shown in Figure 4.25. Comparing these values with the preliminary results obtained in Eqs. (3-7) and (3-8), it can be seen that good agreement exits. The free displacement obtained from 3D finite element simulation is exactly the same as that obtained from Eq. (3-7). However the block force is slightly less than that of Eq. (3-8).

Now using the obtained block force and fee displacement, the stiffness of the PZT stack can be approximated as 11060 /13.5=819 N/μm which is slightly less than that obtained from Eq. (3-9) (K_p=964N/ μm).

Table 4.4 Displacement of PZT stack against pressure force

Pre-load Force (N)	11060	8848	6636	4424	2212	1500	0
Displacement (μm)	0	2.8	5.4	8.1	10.8	11.7	13.5

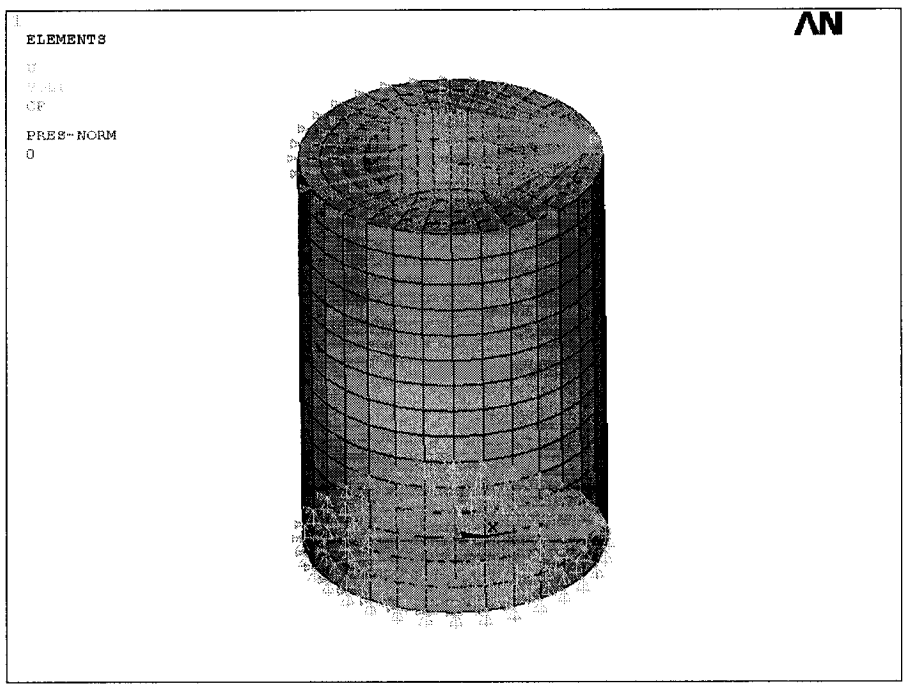

Figure 4.24 Model and boundary conditions of PZT stack

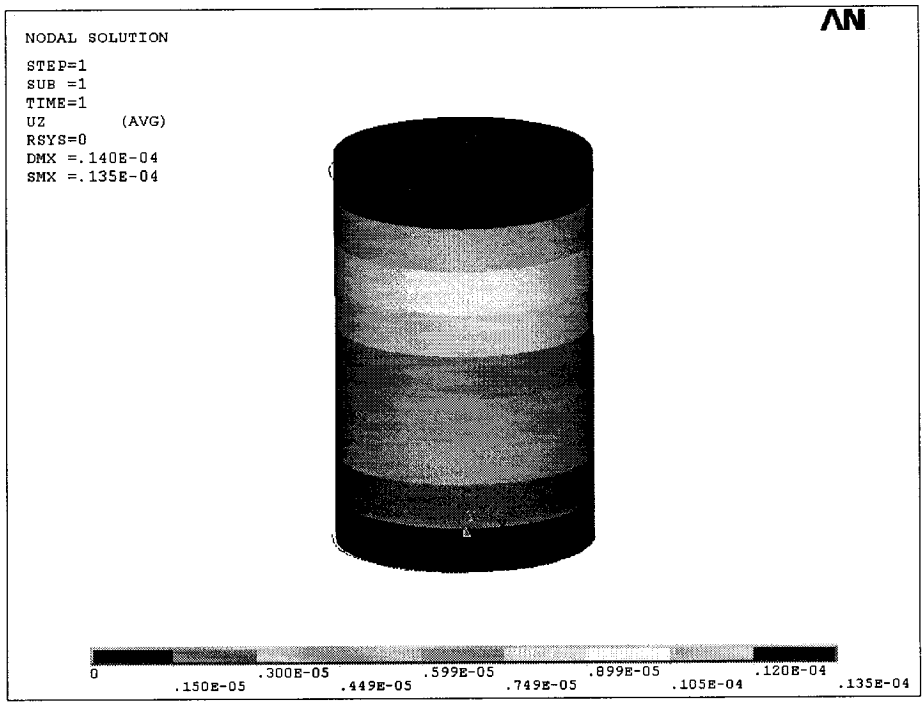

Figure 4.25 Contour plot of displacement of BM532 stack under 200 V

4.5 Extension tube analysis

The extension device consists of a PZT tubular stack, two nuts, and a thin wall tube. The extension tube has two functions. One is to supply the necessary pre-load on the PZT stack in order to prevent the possible tensile stress which has detrimental effect on the PZT stack. The other function is to transfer displacement or force produced by PZT stack in order to assure the inchworm procedure. Since the thickness of the extension tube is crucial to realize these functionalities, a detailed finite element stress and displacement analysis have been conducted in order to avoid any possible failure.

The geometric model of the extension tube has been built in CATIA environment and then it is imported into ANSYS in IGS format. Using element Solid 92, which has the

quadratic displacement behavior and well suited to model the irregular boundaries, the imported model has been meshed. The element Solid 92 has ten nodes with three degrees of freedom at each node, i.e. translations in the nodal x, y, and z directions. Due to the symmetric geometry, only a quarter of the extension cylinder has been modeled. Aluminum 6061 with the following material properties[61] has been selected because of its low elasticity modulus.

Modulus of Elasticity E=69 GPa ; Poisson's ratio $\gamma = 0.33$;

Ultimate Tensile Strength = 124 MPa ; Yield Tensile Strength= 55.2 MPa

The generated mesh and applied boundary conditions are shown in Figure 4.26, where the applied preload is -1533 N. The stress and displacement distribution are demonstrated in Figures 4.27 and 4.28, where the maximum displacement in Z direction is 9.8 μm and maximum von Misses stress is 13.5 MPa. It is noted that the unit of displacement and stress in the figures are mm and MPa, respectively. The stiffness of extension tube K_e has found to be 156 N/μm.

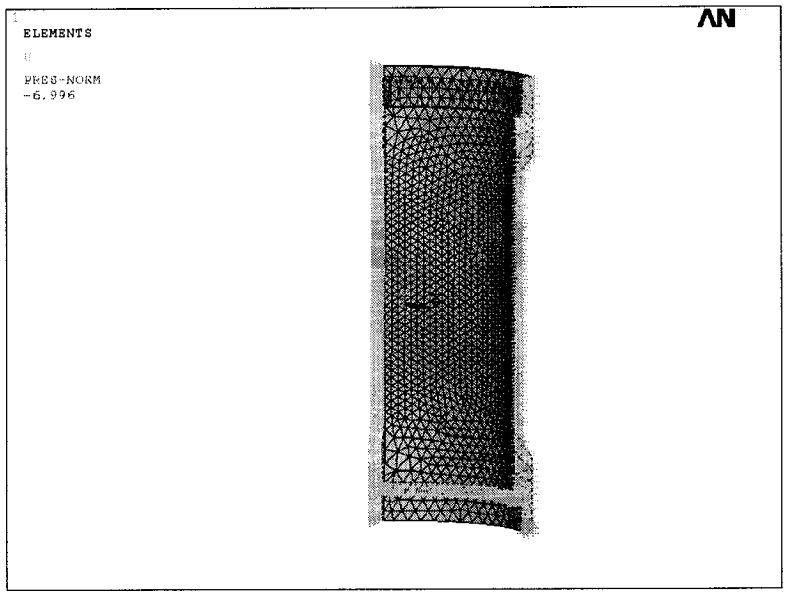

Figure 4.26 FEM model of Extension tube

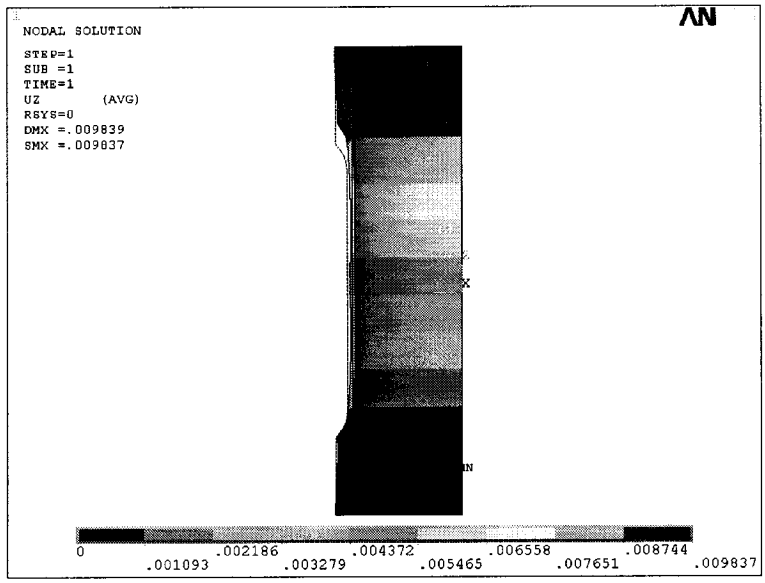

Figure 4.27 Displacement distribution in Z direction in extension tube

4.6 Whole actuator analysis and simulation

In order to simulate the process of piezoelectric inchworm actuator, a mechanical-electrical coupled finite element model has been created using ANSYS. It is better to do research on the clamping device first. In order to better realize this simulation, the clamping device will be first analyzed.

4.6.1 Clamping device simulation

One third of the clamping device has been modeled as shown in Figure 4.28 due to the symmetry of the clamping device in the circumferential direction. Since it has been assumed that the two ends of the clamp have rigid boundary condition, thus the model does not include the support ring. There are two difficulties to simulate the function of the clamping device. First is the pre-load system, which is supplied by Belleville spring washers and nuts. When the nuts are tighten in the assembly process, a pressure load will be applied

on the compliant mechanism through Belleville spring washers to clutch the shaft. The pre-load system has to be included in the model since its effects are important to realize the griping functionality of the compliant mechanism. A special element called pretension element PRETS179 is used to simulate this phenomenon. The second difficulty is the very small clearance between the ends of PZT stack and compliant mechanism as shown in Figure 4.29, which is unavoidable due to the manufacturing tolerances of PZT stack and compliant mechanism. Although it is possible to employ contact elements to handle the clearance problem, birth and death elements have been found to be more convenient. There are other elements used in the finite element model of the compliant device, which are Solid 5 for mechanical & electrical coupling calculation of PZT stack, Solid 95 for the clamps and Solid 45 for the other parts. Figure 4.30 shows the detailed finite element model and applied boundary conditions. In order to simplify the model, the shaft is considered to be rigid. Figure 4.31 shows the deflection simulation of the compliant mechanism model when it is under pressure forces or displacements are applied on its two ends.

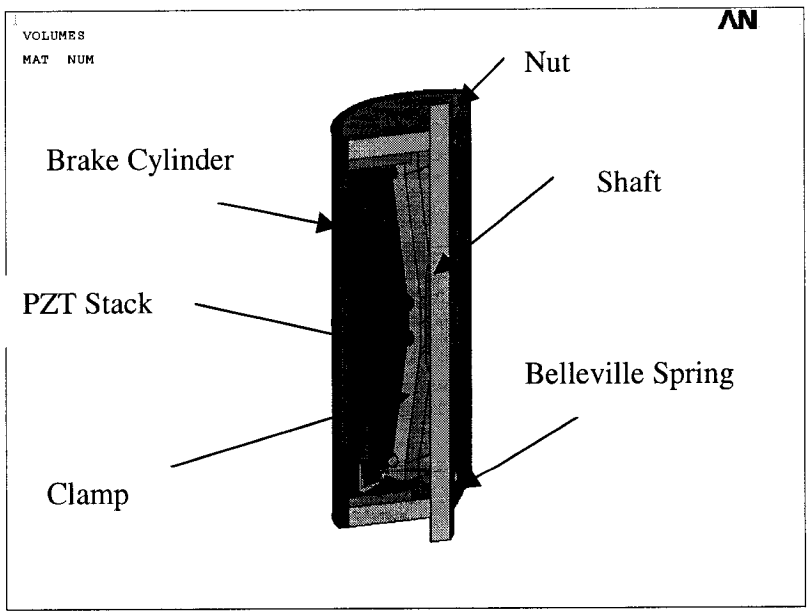

Figure 4.28 3D view of the one third model of the clamping device

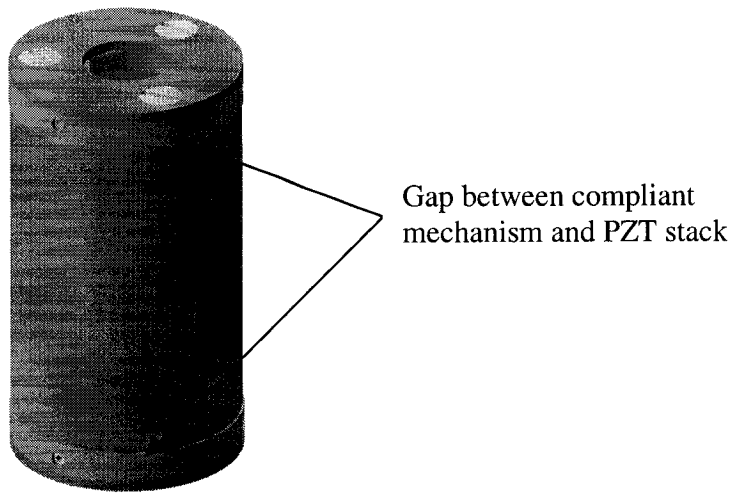

Figure 4.29 Small clearance between compliant mechanism and PZT stack

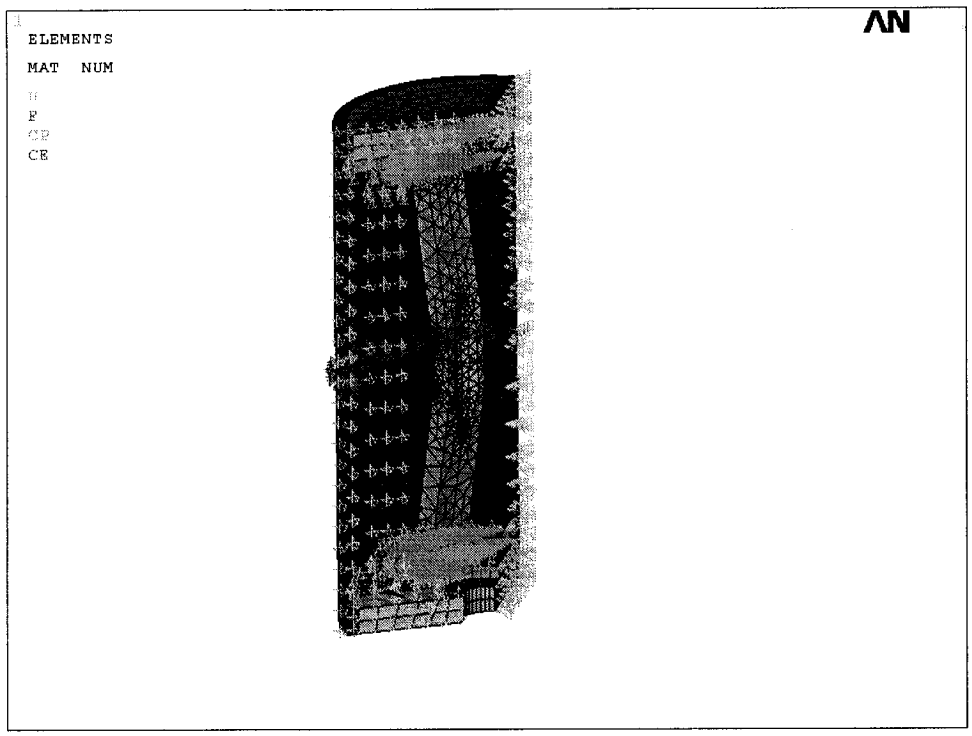

Figure 4.30 Detailed 3D finite element model of the clamping device

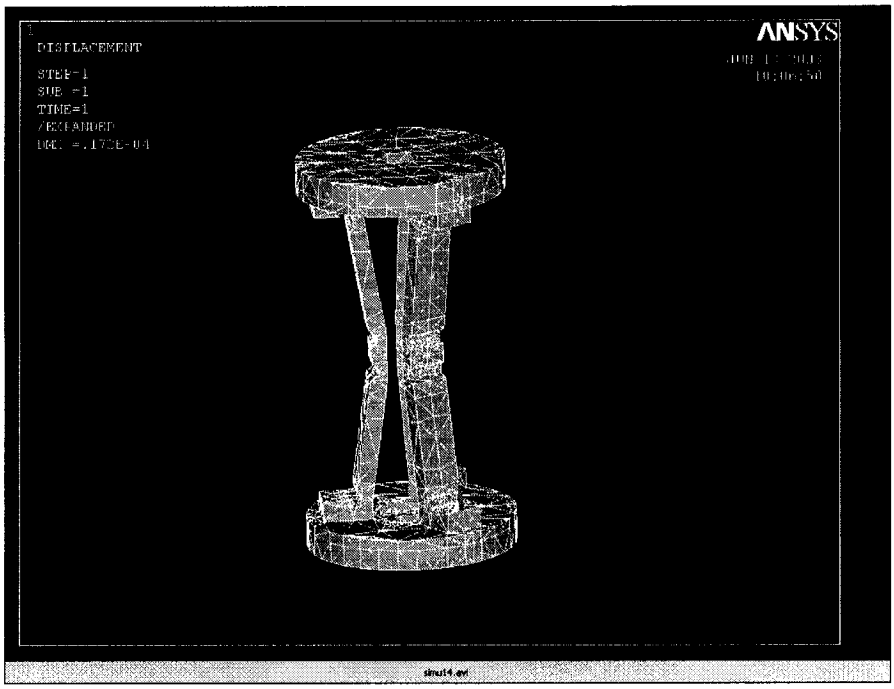

Figure 4.31 Deflection simulation of the of the compliant frame

Using three load steps, the whole clamping procedure has been simulated. In the first step, 1533 N (511 N for one third part) pre-load is applied on the cylinder by using pretension element, which simulates the pressure force acted on the compliant mechanism when the nuts are tightened and Belleville spring washers are contracted. Meanwhile the PZT stack is modeled by the death elements, which means that PZT stack does not withstand any load. Due to this condition, the compliant mechanism clutches the shaft under the applied pre-load condition. In the second step, death elements of PZT stack are replaced by the birth elements, and 200 Volt is applied on the PZT stack, which cause the PZT stack to extend and push the compliant mechanism to release the shaft. In the last or third step the applied 200 Volt is removed from the PZT stack or –200 volt is applied on PZT stack, both of which will cause the compliant mechanism to clutch the shaft again under the recover spring force

produced by the pretension element. The simulated above steps are demonstrated in Figure 4.32.

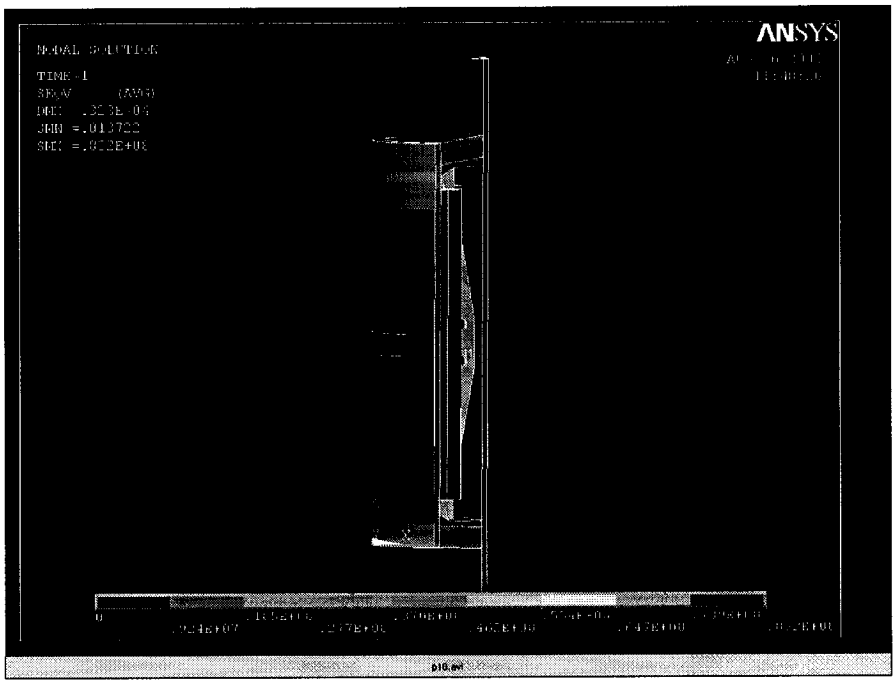

Figure 4.32 Motion of the clamping device simulated in the ANSYS

4.6.2 Whole actuator simulation

After designing all parts of the inchworm actuator, the function of the whole actuator has been simulated in the ANSYS environment using the FEM model. One third of the model has been built again as Figure 4.33. It is assumed that zero clearance exists between the clamps and the shaft. Belleville spring washers are replaced by a solid material whose elastic module is decided by the stiffness of the spring washers. The wall thickness of the extension cylinder is considered to be as the same thickness as the cylinder of the clamping device in order to simplify the model. However, since the cylinder thickness of the clamping device is 3.5 times the thickness of extension cylinder, the elastic module of the extension cylinder has been reduced 3.5 times in order to justify the same cylinder thicknesses for both extension

and clamping devices. The actuator's different stages have been summarized in the following steps:

- Step1: This step is a starting position where the output shaft has been clamped by the braking (clamping) device. There are no input voltages to any of the PZT stack.
- Step 2: In this step, 200 volts has been applied to the lower clamping device; the shaft is then released.
- Step 3: Now 200 volts is applied to the middle extension device; the upper clamping device is pushing upward the shaft due to the extension of the middle cylinder.
- Step 4: Lower clamping device is unloaded in this step; the center shaft is clutched by the clamps.
- Step 5: In this stage, 200 volts is applied to the upper clamping device; the shaft is now released by the clamps.
- Step6: The extension device is unloaded in this step; the middle cylinder is now returned to the original position.
- Step7: Finally upper clamping device is unloaded; the shaft is again clutched by the clamps. Actuator is now in the original state except the output shaft, which is moved upward one step.

The above steps are simulated in the ANSYS environment as shown in Figures 4.34-4.36.

The maximum holding force of one clamping device is 148 N for coefficient of friction of 0.2, and output force would be 74 N. The applied voltage is 200 volts and the inchworm step is 8 micron. The velocity of the moving shaft would be 0.8 mm/s for the frequency of 100 Hz. The maximum von Misses stress on the clamps and the middle extension cylinder wall are found to be 83 MPa and 15 MPa, respectively.

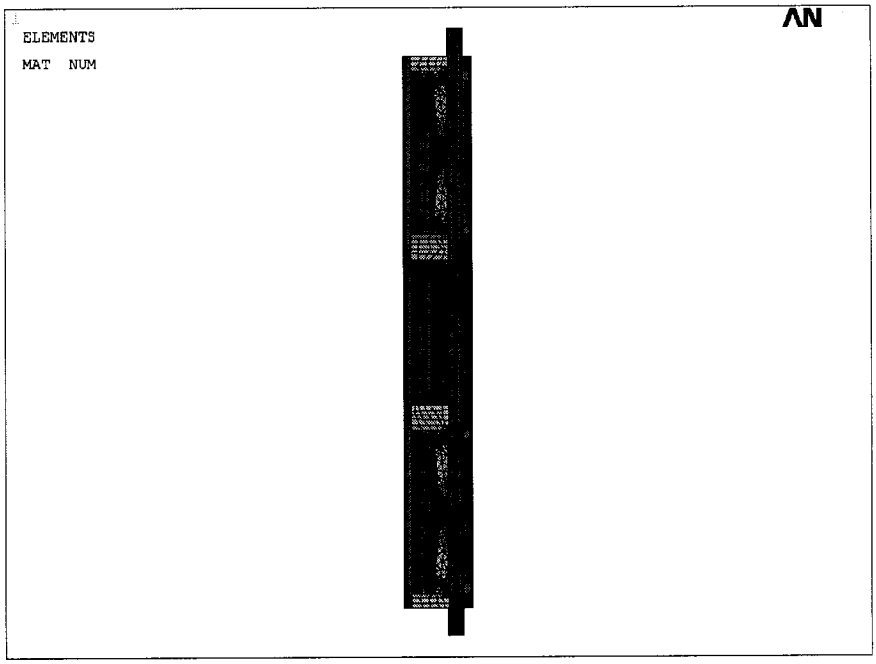

Figure 4.33 Finite element model of the whole actuator

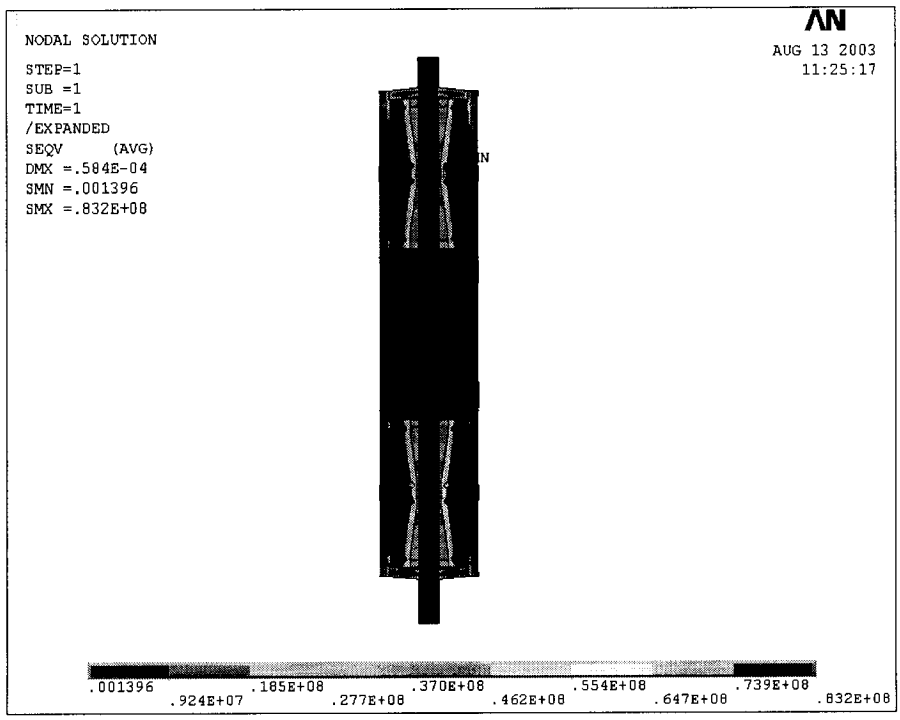

Figure 4.34 Simulation of the whole actuator (step 1)

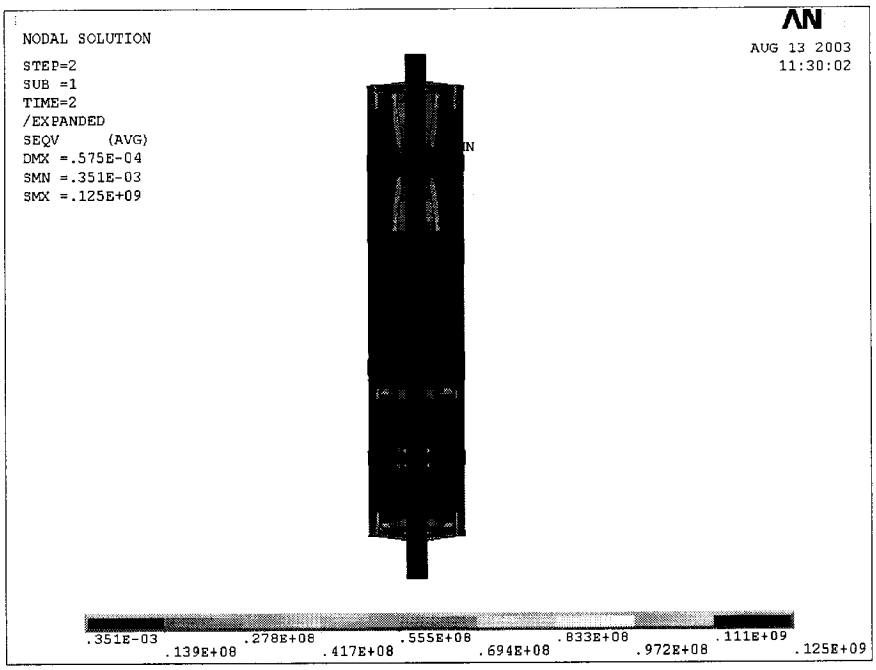

Figure 4.35 Simulation of the whole actuator (step 2)

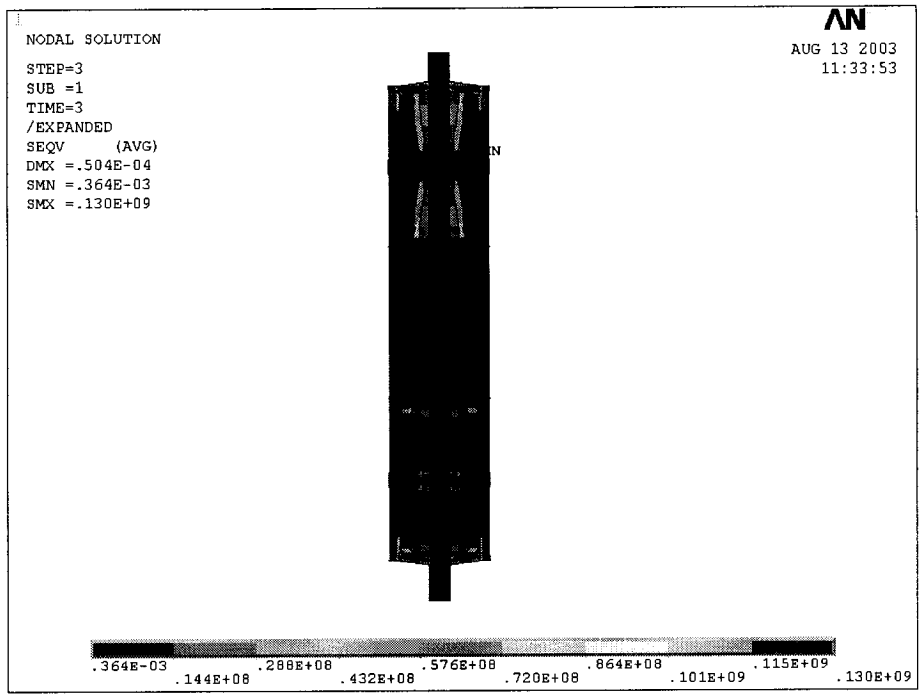

Figure 4.36 Simulation of the whole actuator (step 3)

4.7 Preliminary Fatigue analysis

The maximum step of proposed inchworm actuator is about 8 μm. Now if the actuator is used in a variable geometry smart truss structure and supposed to move 600 mm, then the number of cycles action of the actuator will be about 7.5 x 10^4. Considering this, the fatigue can be an important mode of failure and the fatigue analysis should be conducted to assure that the actuator will function properly in its design service life.

The maximum stress of 170 MPa has occurred at center notches of the clamping arms when a negative 200 volts was applied on the PZT stack, and the shaft was clutched by the clamping arms under the pre-load conditions (see Figure 4.13). The minimum stress at the same location was zero when a positive 200 volts was applied on PZT stack and thus the shaft was released by the clamping arms. Using the stress-life approach in high-cycle fatigue regimes [63], the repeated stress case, in which the stress waveform ranges from zero to a maximum with a mean value equal to the amplitude component, could be analyzed as follow:

the amplitude component: $\sigma_a = \frac{\sigma_{max} - \sigma_{min}}{2} = 85$ MPa (4-10)

the mean component : $\sigma_m = \frac{\sigma_{max} + \sigma_{min}}{2} = \sigma_a = 85$ MPa (4-11)

Since $\sigma_{min} = 0$, thus the stress ratio will be

$$R = \frac{\sigma_{min}}{\sigma_{max}} = 0 \quad (4\text{-}12)$$

Since the mean-stress component is not zero, by using Goodman mean stress correction [63]:

$$\frac{\sigma_a}{\sigma_{a0}} + \frac{\sigma_m}{S_{ut}} = 1 \quad (4\text{-}13)$$

the effective amplitude stress at zero mean would be

$$\sigma_{a0} = \frac{\sigma_a}{1 - \frac{\sigma_m}{S_{ut}}} \tag{4-14}$$

For stainless steel 304, the ultimate tensile strength is S_{ut} = 505 MPa and the approximate endurance limit can be defined as:

$$S_e = 0.5\ S_{ut} = 252 \text{ MPa} \tag{4-15}$$

It is noted that the correction factors are assumed to be 1 since the clamps has perfectly machined and tested in room temperature and reliability of 50% has been considered.

Now using Eq. 4-14, σ_{a0} = 102 MPa

Therefore the fatigue design safety factor can be found as:

$$N_{s.f.} = \frac{S_e}{\sigma_{a0}} = 2.5 \tag{4-16}$$

4.8 Summary

Since the efficiency, accuracy and performance of the inchworm actuator are highly dependent on the functionality of the flexible clamp mechanism, an in-depth design optimization procedure has been conducted in order to obtain optimal design parameters defined for the flexible clamps. The relative curves representing the relationships between design parameters and state parameters (control parameters) were also provided which can be very useful for the researchers. The input stiffness and output stiffness of the compliant mechanism have also been presented which can be used to calculate the pre-load force on and clamping force of the compliant mechanism. The displacement and reaction force of BM532 PZT stack under different pre-loads have been calculated using electrical- mechanical coupling capability of the ANSYS, which is found to be in agreement with the theoretical results provided in Section 3.3.2.4. Then, the steps

involved in the function of the clamping device and the whole actuator have been presented in detail and also the functionality of the clamping device and the whole actuator have been simulated in ANSYS, which provides a vivid action processes of the brake device and the whole inchworm actuator. Finally, a simple fatigue analysis of clamp has been provided. In the next chapter, the experiments conducted on the fabricated prototype will be introduced, and the results of test will be compared with those obtained from simulation.

CHAPTER 5 PROTOTYPE FABRICATION AND EXPERIMENT

5.1 Introduction

In order to verify the proof-of- concept design of this inchworm-type piezoelectric actuator, a prototype has been fabricated in the Machine Shop of Concordia University according to the drawings of the design (Appendix C). The BM532 PZT tubular stacks have also been fabricated and tested. A static tests for both the clamping and extension devices have been performed to find the clamping force and displacement. A functional experiment is also conducted to validate the design and the simulation results.

5.2 BM532 PZT tubular stack

Sensor Technology Ltd fabricated these special designs of PZT stacks. The zero-load displacement, the blocked force and the stiffness measurements have been completed. The figures and data are shown in Appendix D. The characteristics of three PZT stacks and the theoretical values are summarized in Table 5.1.

Table 5.1 Characteristics of BM532 PZT stacks

	Free disp. δ_o (μm)	Average slope (nm/V)	Blocked force F_b (N)	Stiffness K_p (N/μm)	Capacitance (μF)
Stack #1♦	14.7	86.5	3600	250	4.4
Stack #2	15.3	76.5	2300	148	4.4
Stack #3 ♣	14.3	71.6	3300	230	4.9
Theoretical	13.5	67.5	11060	819	6.4

♦ Stack 1 was re-measured after rework. The free displacement changed from 17.3 μm to 14.7 μm and the blocked force changed from 4300 N to 3600 N.

♣ Stack 3 was damaged when the blocked force was measured. Thus, in order to maintain the required free displacement and blocked force, the length of stack was increased from 63.5 mm to 72mm after repairing. This stack will only be used in extension device.

where:

Free displacement δ_o = (max free displacement – min free displacement)/2

Average slope is equal to (max- min displacement)/ voltage range

Voltage range is –200 volts to +200 volts

Block force $F_b = \delta_o * Y_{33}^E * \frac{A}{L}$

Y_{33}^E : Elastic modulus of PZT stack in axial direction measured in short circuit condition

A : Cross section area of PZT stack

L: Length of PZT stack

The displacement versus applied force of the PZT stack #1 when it under 200 V for both FEA and experimental test is shown in Figure 5.1.

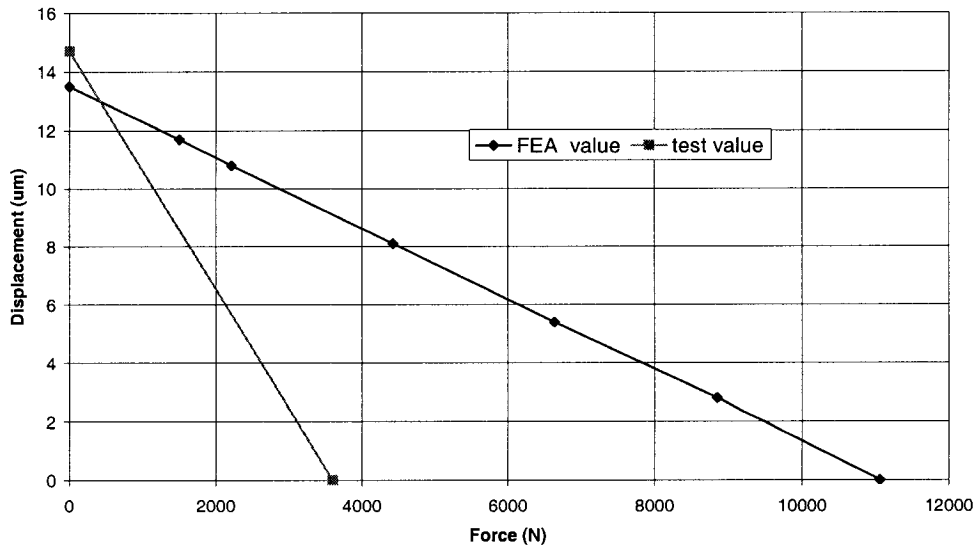

Figure 5.1 Force-displacement of PZT stack #1 diagram

As it can be seen a significant difference exits between the real properties and the theoretical ones of PZT stack. According to the reports submitted by the Sensor Technology

Ltd., the stiffness of the real PZT stacks are only 30 percent of the expected value for the ceramic alone. They implied that the shims and epoxy layers between thin ceramic wafers could have significant contribution to this unexpected low stiffness of the PZT stack. Other defects of PZT stacks such as the initial region of low stiffness (Appendix D Figure 3, Compression vs. applied force measured under short circuit conditions) and the observed misalignment or unparallel of the PZT stack ends which is in the range of 250 μm could also have significant effect for low stiffness of the PZT stack. The initial low stiffness will basically cause over 18 μm displacement to be lost under the low pressure load. The defects will also increase the clearance between PZT stack and the compliant mechanism, however they can be overcome by the pre-load device through reducing the diameter of shaft and adjusting clamps positions by adjustment screws. Since the fabricated PZT stacks have unexpectedly low stiffness, naturally the generated block force provided in Table 5.1 would be low in comparison to the simulated results. The lower blocked force of PZT stacks will limit the maximum clamping force and therefore the output force of the inchworm actuator. According to Figure 5.1, if the output displacement of PZT stack has to be 10 μm, the maximum output force of PZT stack is 1151 N, which is much lower than the designed pre-load 3100 N.

5.3 Clamping and extension device assemblies

The difficult parts for manufacturing are clamps and support rings. They should be as identical as possible. MAZAK CNC mill and GILDEMEISTER CNC lathe were used to fabricate these parts. Figures 5.2-5.5 show the clamping assembly, extension assembly and their relative components.

In order to reduce the clearance between the PZT stack and the compliant mechanism, the thickness of the supporting ring was matched according to the real length of

individual PZT stacks. The center hole diameters of two compliant mechanisms should be 8.9 mm, which are the same as the diameter of the shaft (see Figure 3.18). After fabrication the hole diameters of the two compliant mechanisms were found to be 8.585 mm and 8.814mm. The difference can be attributed to the manufacturing and assembly tolerances. The diameter of shaft was then reduced from 8.9 mm to 8.5 mm in order to accommodate the manufacturing and assembly tolerances. The careful adjustment has to be well performed to assure that the two compliant mechanisms are aligned with the axis of the shaft and small clearance exits between the contact surfaces of all six clamps and the shaft. It can be realized from Figure 4.22 that the clearance between the clamps and the shaft will greatly reduce the clamping force of brake devices and decrease the performance of the inchworm actuator. Therefore skillful adjustments by using screws on the support rings are important to obtain the maximum clamping force.

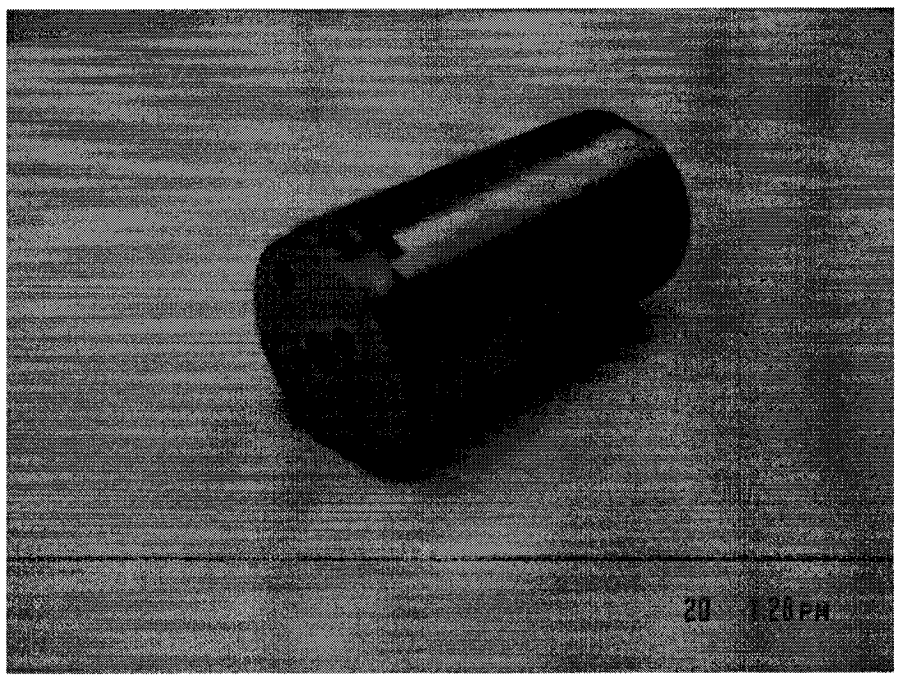

Figure 5.2 Clamping assembly

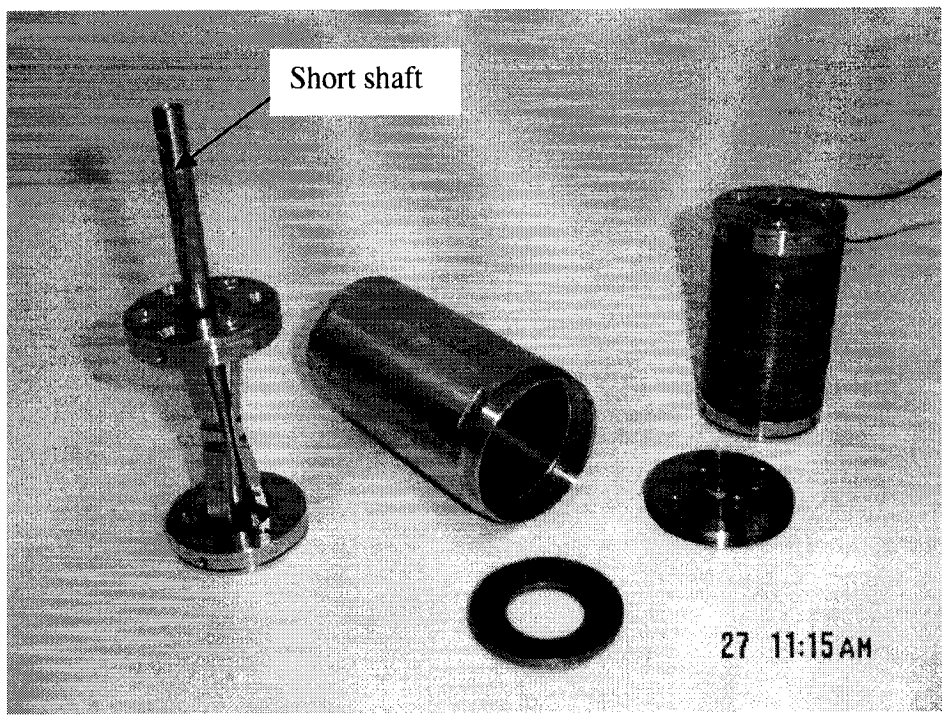

Figure 5.3 Components of the clamping assembly

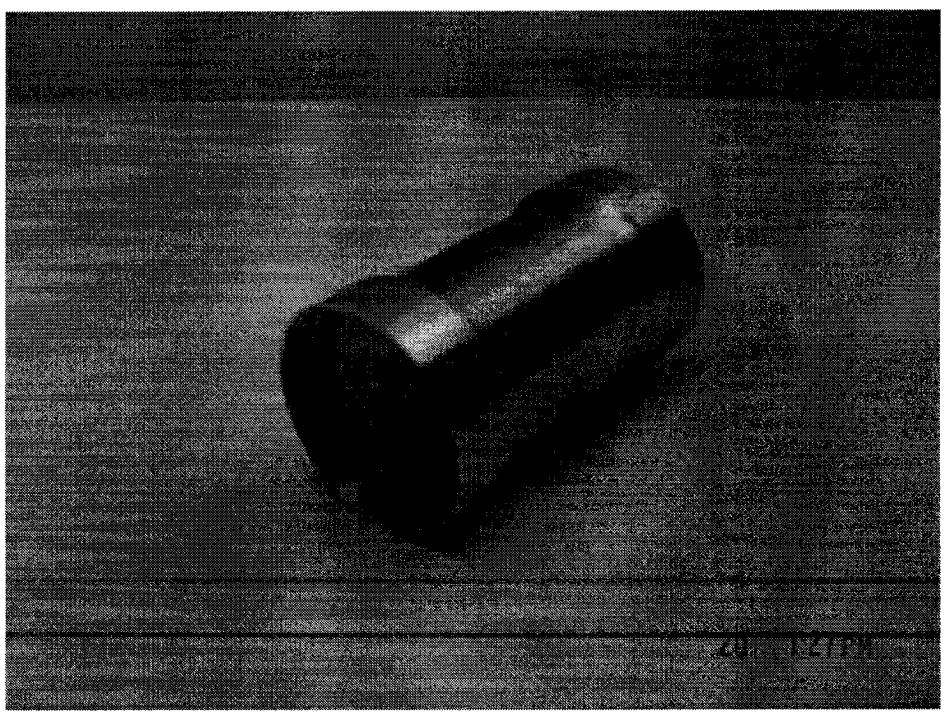

Figure 5.4 Extension assembly

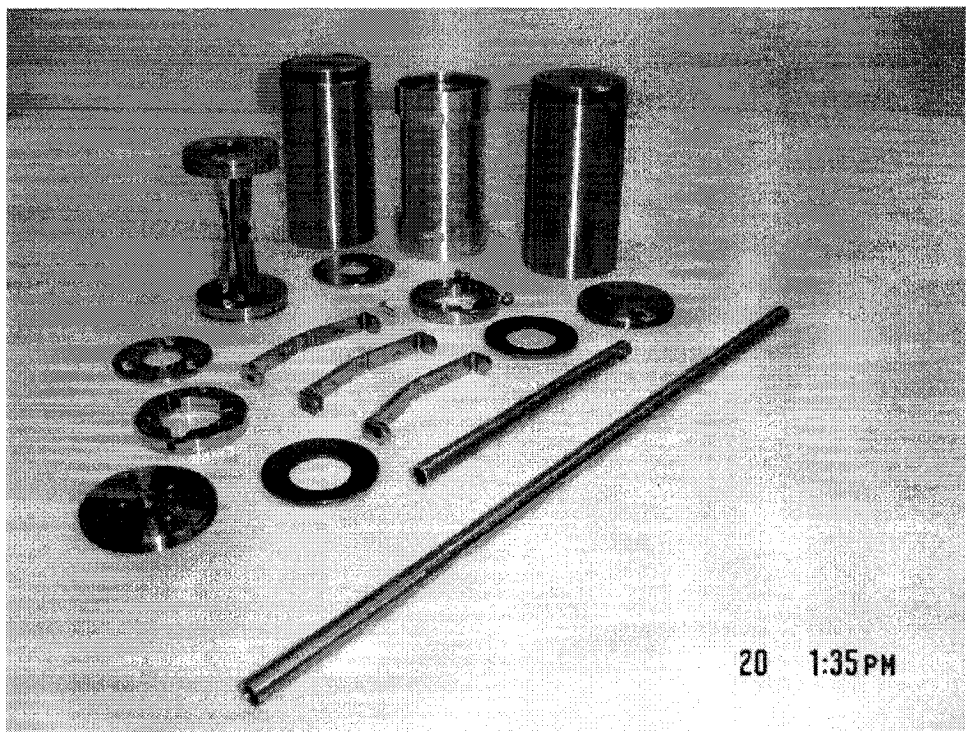

Figure 5.5 All the metal parts of the inchworm actuator

5.4 Experiment setup and results

The preliminary static and functional tests were performed to verify the design and the simulation results.

5.4.1 Zero-load displacement measurement of BM532 PZT stack

In order to verify the test result of Sensor Technology Ltd., Zero-load displacement measurement has been conducted on the PZT Stack #1. A positive 200 volts and negative 200 volts were applied on PZT stack. Figure 5.6 shows the experiment setup for zero-load displacement measurement. The average displacement is ± 13 μm , which is less than the values measured by Sensor Technology Ltd.(i.e. 14 ~17 μm) but is similar to the theoretical value (i.e.13.5 μm).

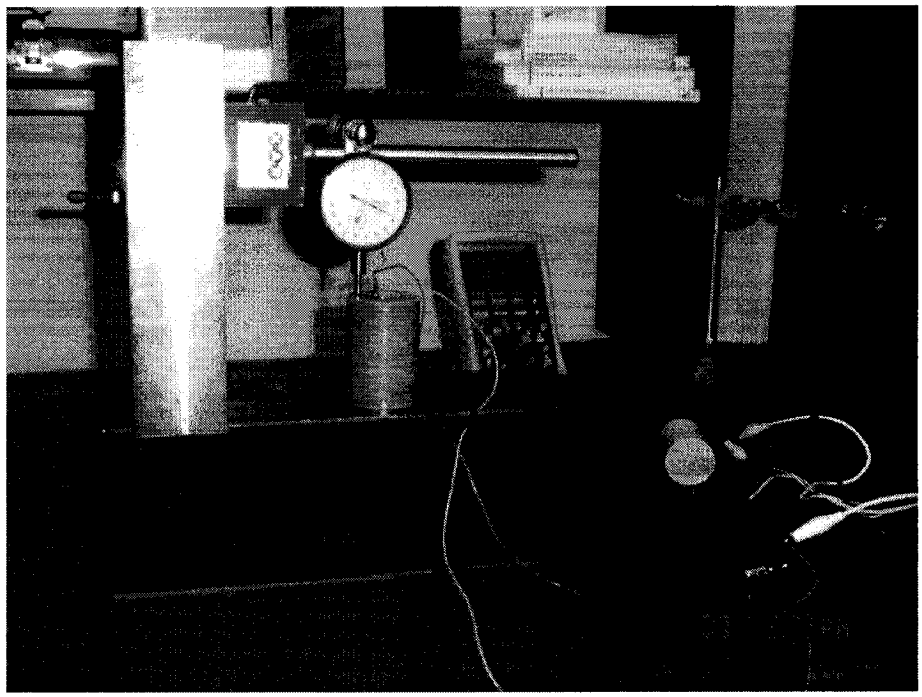

Figure 5.6 Experiment setup for zero-load displacement measurement

5.4.2 Displacement measurement of extension device

To measure the displacement of the extension device, the PZT stack was inserted into the extension cylinder. Then a negative 200 voltage was applied on the PZT stack causing the PZT stack to be contracted 13 μm. The two end nuts would be tightened lightly. The PZT stack was short-circuited and a pre-load was then applied. Finally, applying positive 200 V or negative 200 V on the PZT stack, the average displacement of extension device has been measured to be ± 8 μm. The experimental setup for the extension displacement measurement is shown in Figure 5.7. Since the stiffness of the extension cylinder K_e is 155 N/μm (see Section 4.3) and the stiffness of PZT stack K_p is 250 N/μm, the applied pre-load would be

$$F_p = \delta_o * \left(\frac{K_p * K_e}{K_p + K_e}\right) = 1244 \text{ N} \qquad (5\text{-}1)$$

Now using Eq. 3-2, the displacement of extension device under the spring pre-load is

$$\delta_s = \pm \delta_o (K_p/(K_p+K_e)) = \pm 8 \ \mu m \qquad (5\text{-}2)$$

which is exactly similar to the measurement result. The test and theoretical displacements of extension device are summarized in Table5.2.

Table 5.2 Displacement comparison of extension device

	- 200 Volts	+ 200 Volts
Test results	- 8 Micron	+8 Micron
Theoretical results	- 8 Micron	+8 Micron

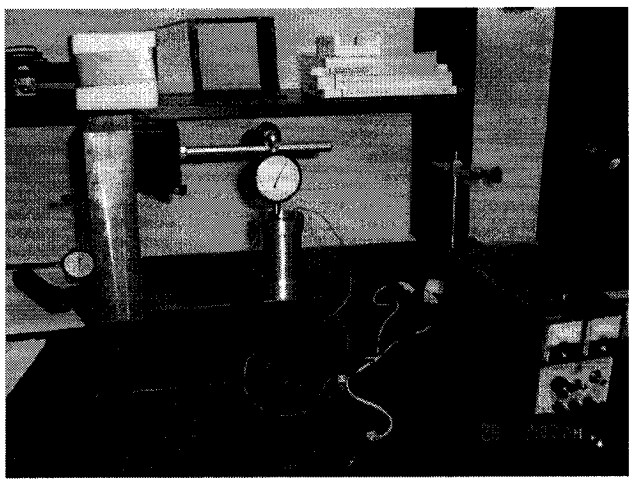

Figure 5.7 Experiment setup for the extension displacement measurement

5.4.3 Brake device function test

The objective of the brake device function test is to measure the clamping force which will determine the maximum holding force and the output force of actuator. Since the pre-load pressure force and the clearance have significant effect on the maximum clamping force, first they will be addressed.

5.4.3.1 Application of pre-load force

It is assumed that zero clearance exits between the clamps and shaft. Since the initial stiffness of the PZT stack is small (see Appendix D), when end nuts are tightened, a pre-load will be applied on the compliant mechanism through the Belleville spring washers. According to the results of Section 4.3, the axial stiffness of the compliant mechanism is 155 N/μm. The maximum displacement range of the PZT stack under pre-load is also10 μm (See Section 3.3.2.4) , therefore, the pre-load should be at least 1550 N.

In this design, three B1750-057 Belleville spring washers (h = t) in parallel have been used to establish the pre-load spring system. Stiffness of the total spring washers K_w is 7.973 N/μm (see Section 3.8 K_w=3*2.658 N/μm). The compliant mechanism is in series with the spring washers. To better realize this configuration, a simplified pre-load spring model has been shown in the Figure 5.8. Therefore, the total stiffness can be written as:

$$K_s = K_c * K_w / (K_c + K_w) = 7.6 \text{ N/μm.} \qquad (5\text{-}3)$$

Now considering Eq. (5-3), for a pre-load of 1550 N, the axial displacement of the nut should be 0.2 mm, which means the rotation angle of the nut should be 72 ° since the pitch of the nut is 1 mm. Figure 5.9 demonstrates how the torque has been applied on the nut in order to induce the above preload..

Now when a negative 200 V applies on the PZT stack, it will contract 10 μm. The clamping force will then be doubled but the pre-load pressure force should be over 3100. In order to investigate the effects of the pre-load forces on the clamping force, the experiments have been conducted to measure the output forces of clamping device and its changes with the number of spring wafers in parallel and the rotation angles of end nut. Table 5.2 ~ 5.3 show the results. when the pre-loads larger than 1700 N, no significant increase in the ouput force can be observed. This can be attributed to this fact that the stiffness of the compliant

mechanism and the displacement of the PZT stack under the pre-load condition are decisive factors on the clamping force. It is noted that the pre-load forces have been estimated using curves in Figure 3.22. It has to be also pointed out that the output forces measured show some variation due to the friction conditions and the hysteresis of PZT stack.

Table 5.3 Output force variations with respect to the number of spring wafers in parallel when the nut is rotated 90° rotation angle (measured by load cell)

Number of spring wafers	Pre-load force (N)	Measured torque (Nm)	Output force (N)		
			0 V	-200 V	200 V
2	1734	7.5	30	43	0
3	2601	10.8	31	47	0
4	3468	13.6	31	46	0

Table 5.4 Output force variations with respect to the rotation angles of the nut when three spring wafers are in parallel (measured by dead weight)

Rotation angle (Degree)	Pre-load force (N)	Measured torque (Nm)	Output force (N)		
			0 V	-200 V	200 V
90	2601	10.2	24.5	44	0
120	3294	19.0	29.0	52.5	0
150	3990	23.0	37.7	55.4	0

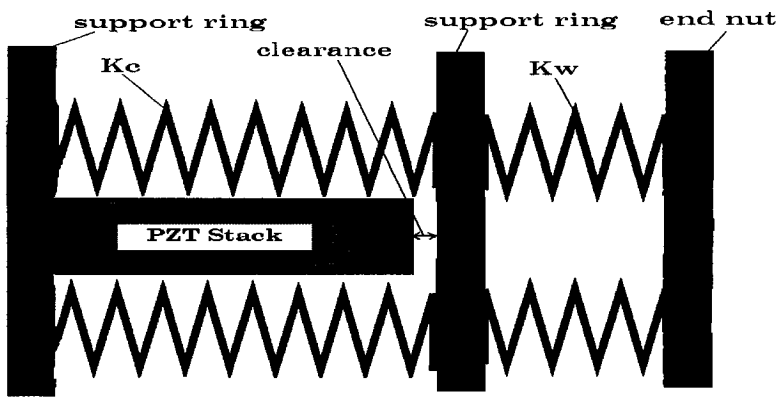

Figure 5.8 Model of pre-load spring system

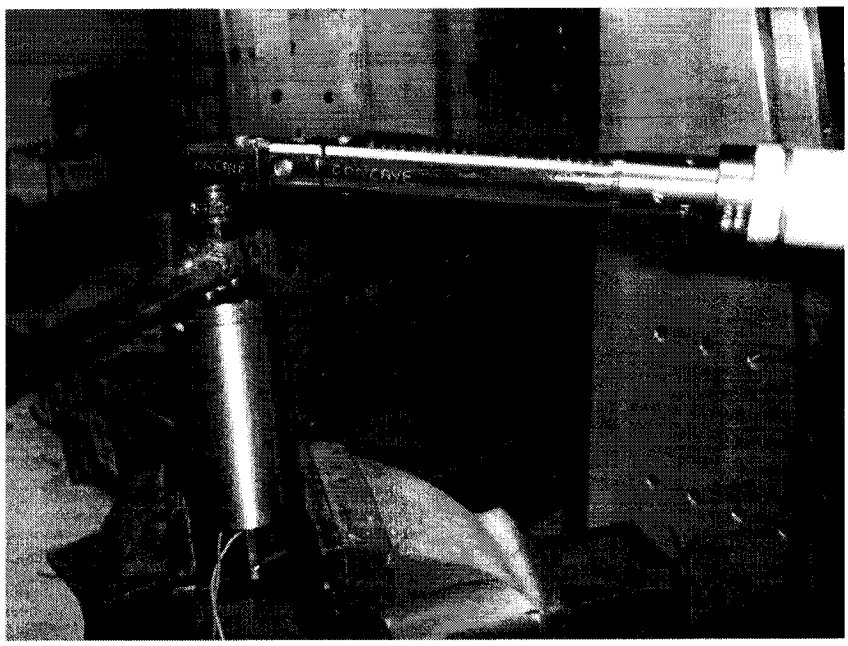

Figure 5.9 Applying pre-load spring force on the brake device

5.4.3.2 Output force measurement and clearance adjustment

Since it is difficult to directly measure the clamping force of the brake device, the clamping force has been obtained indirectly using the measured output force. Basically the claming force of the brake device is the output force divided by the coefficient of friction (assumed to be 0.2).

It is very difficult to control the clearance between PZT stack and the support ring (see Figure 5.8), since it depends on the length of the PZT stack and the length of the compliant mechanism. The initial displacement of PZT stack due to its low stiffness under small pressure (see Appendix D), which is not expected, make it also more complex. By using matched fabrication and thin metal washers, the clearance could be controlled to less than 20 μm, otherwise, the clamping device will not work efficiently.

The clearance adjustment of PZT stack and support ring also affects the clearance between the clamps and the shaft. The appropriate adjustment by using the special screws on

the support rings can significantly reduce this clearance, which is difficult to measure, and normally there is 25 μm to 50 μm clearance between the clamps and the shaft. Considering that the clearances have a crucial effects on the maximum clamping force of brake device, the test results can be always improved by skillful adjustments. In order to increase the clamping force, a negative 200 volts is applied on PZT stack. In this case the clamping force is theoretically twice of that when no power is applied on the PZT stack. The test results and comparisons are listed in Table 5.4. Figures 5.10 and 5.11 show the experimental setup to measure the clamping force. It is noted that the holding force of the whole actuator has measured to be 100 N.

Table 5.5 Test and theoretical results for the output force of the clamping device

	no power (zero volt)	- 200 volts	+ 200 volts
test results	38 N	55 N	0
theoretic calculation	8.7 N~ 79.8 N	17.4 N~159.6 N	0

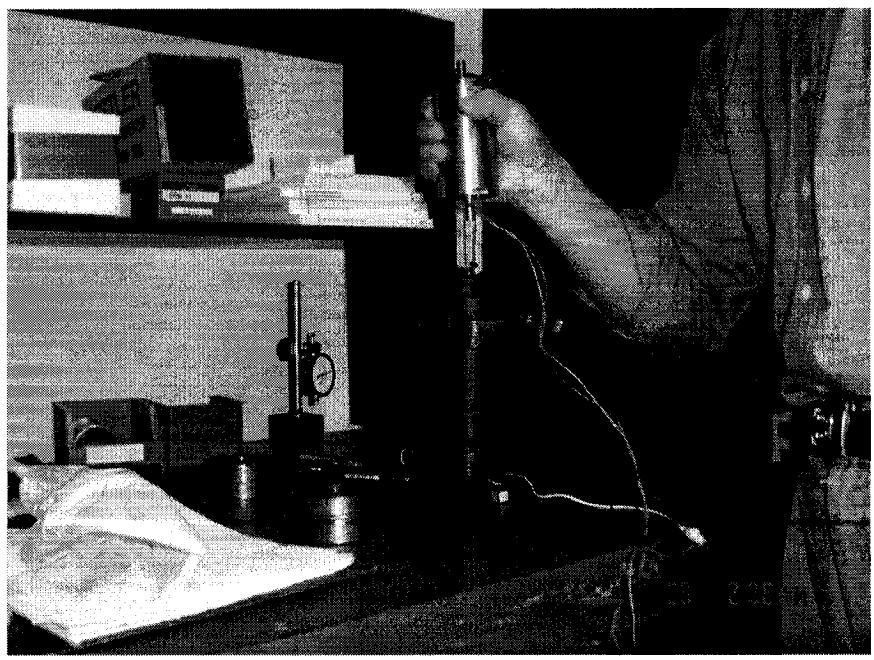

Figure 5.10 Clamping force measurement using hanging dead weights

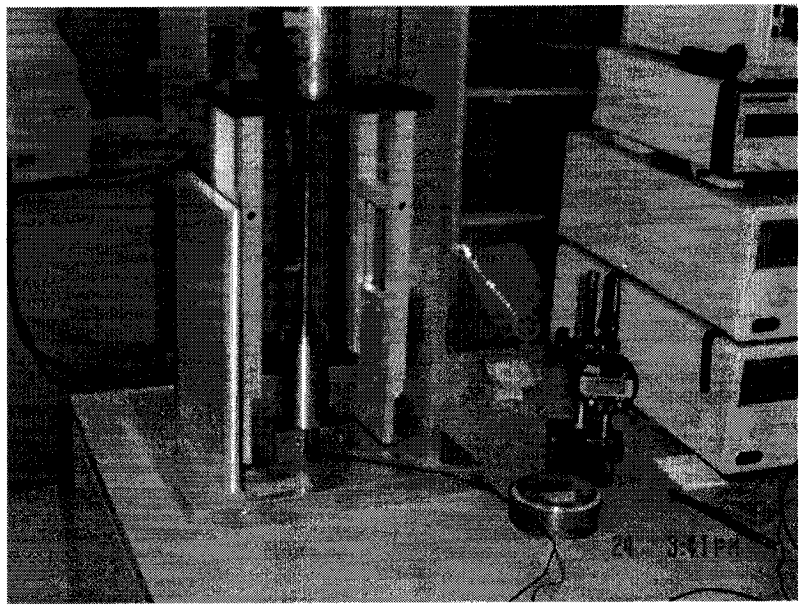

Figure 5.11 Clamping force measurement using sliding stand and dead weight

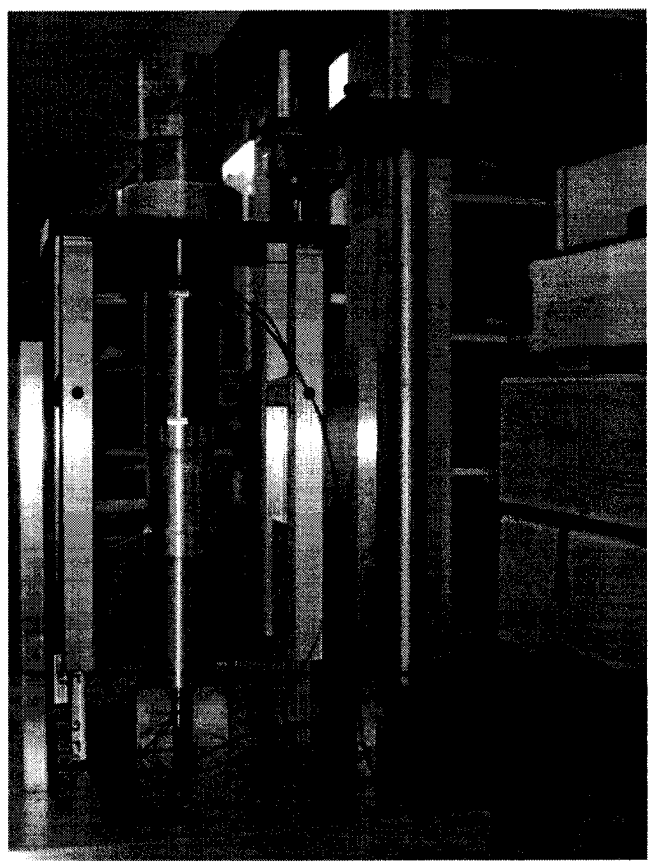

Figure 5.12 Actuator holding force measurement

As it was noticed before in Table 5.1, the blocked forces of the fabricated PZT stacks are much lower than the expected design requirements, so the pre-load forces could not be over 2000 Newton. This discrepancy between the block force of the fabricated PZT stack and the expected block force is essentially the main reason for the disagreement between the predicted and experimental output forces. How using the above experimental results, the proposed concept design were proved to be practical.

5.5 Summary

The free displacement, blocked force, and stiffness of BM532 PZT stacks have measured. The results confirmed that the blocked force and stiffness of all three BM532 PZT stacks are only one third of the design requirements. The reason for this unexpected behavior of the PZT stacks is mainly due to the defects during the fabrication and assemblage of the thin ceramic wafers of the PZT stacks. The lower blocked force and lower stiffness naturally resulted in lower output force of inchworm actuator. The theoretical output force is 74 N at zero volt and 148 N at negative 200 volts, while the experiment output force is 38 N at zero volts (no power) and 55 N at negative 200 volts. The output force could be increased by reducing the clearance between the clamps and shaft through the adjustment device. Although the experimental output force of the actuator was lower than that of expected due to the low qualities of PZT stack and the manufacturing tolerances, the finite element analysis and the prototype experiments proved that the actuator design is novel and effective.

CHAPTER 6 CONCLUSIONS AND FUTURE WORKS

6.1 Introduction

The study of adaptive structure technology is extremely important because of their demonstrated potential to outperform conventional structures in a number of different applications such as shape control, vibration suppression, reduction of acoustic emissions, self-health monitoring and damage mitigation. An adaptive truss structure can be formed through the use of active members, which include actuators and sensors. Since the performance of these active members is the decisive factor in the feasibility study of the adaptive structures, thus the design and fabrication of efficient and accurate active elements will continuously be part of the focus in adaptive structure's research community.

Among many types of actuators, which can be embedded in adaptive structures, the inchworm-type actuators are more attractive due to their large displacement, large force and high resolutions capabilities. The objective of this research is to present a proof-of-concept design of an inchworm-type piezoelectric actuator with output of maximum displacement and force which can be used for shape control and vibration control of adaptive truss structures.

The proposed inchworm actuator adopts "pusher" type with frictional clamping mechanisms. Similar to most inchworm-type actuators, it consists of three main components: two clamping or braking devices and one expanding device. The two frictional clamping devices provide alternating braking forces when the moving shaft, which is pushed by the expanding device, walks inside the PZT tubular stacks and emulates an inchworm, summing small steps to achieve large displacements. Since the development of an efficient clamping mechanism is essential to obtain the high force and displacement capabilities, an in-depth design optimization procedure has been conducted to find the optimal design parameters of

the flexible clamping mechanism. CATIA is used as a platform to model the whole actuator and ANSYS is used to analyze and optimize the performance of the actuator.

The complete design of the proposed actuator has been performed using the finite element analysis. The simulation result confirms that the output force of 74 Newton and incremental displacement in each step of 8 micron can be achieved using the proposed actuator. A prototype of actuator has been fabricated and static tests have been performed to validate the simulation results.

6.2 Conclusions

The following important conclusions can be drawn from the analytical and experimental studies undertaken in this research.

- The concept – design of inchworm-type piezoelectric actuator is novel and practical. The compliant mechanism with flexible hinges is efficient. The adjustable screw device is helpful to reduce the clearance and the tolerance of manufacture.
- The parameterized finite element model of clamp has been proved to be successful to design a robust clamp in order to increase the output force of actuator.
- The simulation of whole piezoelectric inchworm actuator using piezoelectric coupling analysis, pretension element, death and birth elements, contact elements have been performed and compared with experiments.
- The experiments of PZT stacks, clamping device, extension device, adjustment device and pre-load system have been conducted. The results are in agreement with the simulation results.
- Although the blocked force and stiffness of all three BM532 PZT stacks are only one third of design requirements, the prototype of inchworm actuator can still function

through proper adjustment, however the experimental output force is found to be 38 N at zero volts and 55 N at negative 200 volts which are lower than that of the theoretical predictions 74 N and 148 N respectively.

- Since the clearances have crucial effect on the performance of the actuator, the output force could be increased by reducing the manufacturing tolerances and the clearance between the clamps and shaft through the adjustment device

6.3 Future work

Although this thesis has taken an important step towards the understanding of the inchworm-type actuators, other interesting aspects are identified to complement this research. These are summarized as:

- All the calculation and experiments conducted in this research are under static conditions. The dynamic test and dynamic simulation of this piezoelectric inchworm actuator should be carried out to obtain more realistic results.
- Increasing the stiffness of the compliant mechanism, improving the properties of PZT stacks, reducing the clearance between clamps and shaft or even using micro-ridges instead of friction principle can create a larger output force of actuator and better dynamic characteristics.
- Using Titanium instead of stainless steel and adopting more compact and powerful PZT stacks can reduce the weight of the actuator and thus make it more suitable in space structure applications.

REFERENCES

1. Yan, Y. J. and Yam, L.H., "Optimal design of number and locations of actuators in active vibration control of a space truss", *Smart Material and Structure,* Vol. 11, pp.496-503, 2002

2. Lu, L.Y., Utku, S., and Wada, B.K., "Vibration Suppression for Large Scale Adaptive Truss Structures Using Direct Output Feedback Control", *Advances in vibration Control for Intelligent Structures, Advances in Intelligent Material Systems and Structures*, Vol. 1, pp70-82, 1994

3. Saravanan U., Sivakumar, S. M., and Kalyanaraman,V., "A study on the design and behavior of smart antenna", *Smart Material and Structure,* Vol. 10, pp.580-598, 2001

4. Lammering, R., Jia, J. and Rogers, C. A., " Optimal Placement of Piezoelectric Actuators in Adaptive Truss Structures", *Journal of Sound and Vibration*, Vol. 171, No. 1, pp-67-85, 1994

5. Robertshaw, H.H., and Reinholtz, C.F., "Variable Geometry Trusses", Smart Materials, Structures, and Mathematical Issues, U.S. Army Research Office Workshop on Smart Materials, Structures, and Mathematical Issues, pp105-120, 1988

6. Natori, M. and Ogura, S., " Control of Truss Structures Using Member Actuators", *Mechanical Systems and Signal Processing,* Vol. 7, No. 4, pp321-333, 1993

7. Utku, S., *Theory of Adaptive Structures: Incorporation Intelligence into Engineered Products*, CRC Press, 1998

8. Uchino, K., *Piezoelectric Actuators and Ultrasonic Motors*, Kluwer Academic Publishers, 1997

9. Preumont, A., *Vibration Control of Active Structures: An Introduction,* 2 nd Edition, Kluwer Academic Publishers, 2002

10. Uchino, K., "Piezoelectric ultrasonic motors: overview", *Smart Material and Structure*, Vol. 7, pp.273-285, 1998

11. Bexell, M. and Johansson, S., "Characteristics of a piezoelectric miniature motor", *Sensors and Actuators*, Vol. 75 pp118–130, 1999

12. Kummel, M., Goldschmidt, S., and Wallaschek, J. "Theoretical and experimental studies of a piezoelectric ultrasonic linear motor with respect to damping and nonlinear material behaviour", *Ultrasonics,* Vol. 36, No.1, pp103-109, 1998

13. Petit, L., Briot, R., Lebrun,L., and Gonnard P. "A Piezomotor Using Longitudinal Actuators", *IEEE Transactions on Ultrasonics, Ferroelectrics, and Frequency Control*, Vol. 45, No.2, pp277-284, 1998

14. Galane, T., Frank, J., Bernard, J., Chen, W., and Lesieutre, G., "Design, Modeling, and Performance of a High Force Piezoelectric Inchworm Motor", *Journal of Intelligent Material Systems and Structures*, Vol.10, pp. 962-972, 1999

15. Yeh, R., Hollar, S. and Pister, K.S.J., "Single Mask, Large Force , and Large Desplacement Electrostatic Linear Inchworm Motors", *The 14 th IEEE International Conference on Micro Electro Mechanical Systems*, Jan. 2001, pp260-264

16. Bexell, M. and Johansson, S., "Characteristics of Piezoelectric Miniature Motor", *Sensors and Actuators*, Vol. 75, 1999, pp118-130

17. Stibitz, G.R. "Incremental Feed Mechanisms", Patent #3,138,749, 1964

18. Hsu, S., Arbor, A. and Blatter, A. "Transducer", Patent #3,292,019, 1966

19. Locher, G.L., "Micrometric Linear Actuator", Patent #3,296,467, 1967

20. Brisbane, A.D. "Position Control Device", Patent #3,377,489, 1968

21. G.V. Galutva, "Device For Precision Displacement of a Solid Body", Patent #3,684,904, 1972

22. Bizzigotti, R.A., "Electromechanical Translation Apparatus", Patent #3,902,085, 1975

23. May, W.G. Jr., "Piezoelectric Electromechanical Translation Apparatus", Patent #3,902,084, 1975

24. Burleigh Instruments Ltd. Company technical literature

25. O'Neill, C.G. and Foster, C.E., "Electromotive Actuator", Patent # 4,219,755, 1980.

26. Fujimoto, T., "Linear Motor Driving Device", Patent #4,736,131, 1988.

27. Takahara, K., Kuwao, F., Shigehara, M., Katoh, T., and Motohashi, S., "Piezo Linear Actuators for Adaptive Truss Structures", *Adaptive structures; Proc. of the ASME Winter Annual Meeting*, San Francisco, CA, Dec. 10-15 1989, pp. 83-88.

28. Sekine, K., Shibayama, Y., Iwasawa, N., Tagawa N., Sunahara, S., Yoshida, S., and Arikabe, T., "Identification and adaptive control of flexible truss structures", *First Joint US/Japan Conference on Adaptive Structures,* Maui, HI, Nov 13-15 1990, pp. 458-484.

29. Shibuta, S., Morino, Y., Shibayama, Y. and Sekine, K., "Adaptive Control of Space Truss Structures by Piezoeletric Actuator", *Journal of Intelligent, Material, and Structure*, Vol. 3, 1992, pp. 697-718.

30. Zhang, B. and Zhu, Z., "Design of an Inchworm-Type Linear Piezomotor", *Smart Structures and Materials 1994: Smart Structures and Integrated Systems*, Vol. 2190, 1994, pp. 528-539

31. Henderson, D. and Fasick, J.C., "Inchworm Motor Developments for the Next Generation Space Telescope", *Current Developments in Optical Design and Engineering VII*, Vol. 3429, 1998, pp252-256

32. Newton, D., Garcia, E., and Hornel, G. C., "A linear piezoelectric motor", Smart Material and Structure, Vol. 7, No. 3, pp.295-304, 1998

33. Galane, T., Frank, J., Bernard, J., Chen, W., and Lesieutre, G., "Design, Modeling, and Performance of a High Force Piezoelectric Inchworm Motor", *Journal of Intelligent Material Systems and Structures*, Vol.10, pp. 962-972, 1999

34. Canfiel, S. Edinger, B. Frecker, M. and Koopmann, G., " Design of Piezoelectric Inchworm Actuator and Compliant End-Effector for Minimally Invasive Surgery", *SPIE Proceedings*, Vol. 3668, pp. 835-843, 1999

35. Roberts, D., "Development of a Linear Piezoelectric Motor based upon the Inchworm Model", *Smart Structures and Materials 1999: Smart Structures and Integrated Systems,* Vol. 3668, 1999, pp. 705-716

36. Kim, J, Kim, J. D., and Choi, S.B., "A Hybrid inchworm linear motor", *Mechatronics*, Vol. 12, 2002, pp525-542

37. Frank, J., Koopmann, G., Chen, W. and Lesieutre, G. "Design and Performance of a High Force Piezoelectric Inchworm Motor, *SPIE Proceedings*, Vol. 3668, pp. 717-723, 1999.

38. Vaughan, M. E., "The Design, Fabrication, and Modeling of a Piezoelectric Linear Motor", M.S. Thesis, Virginia Polytechnic Institute and State University, 2001

39. Murata, T., "Drive Apparatus and Motor Unit Using The Same", Patent #4,947,077, 1990.

40. Lee, S. and Esashi, M., "Design of the Electrostatic Linear Microactuator Based on the Inchworm Motion", *Mechatronics*, Vol. 5, No. 8, pp. 963-972, 1995

41. Carman, G., Chen, Q., Yao, D. and Kim, C., "Mesoscale Actuator Device: Micro Interlocking Mechanism to Transfer Macro Load", *Sensors and Actuators*, Vol. 73, pp. 30-36, 1999

42. Park, J., Keller, S., Carman, G. P. and Hahn, H. T., "Development of a compact displacement accumulation actuator device for both large force and large displacement", Sensors and Actuators Vol. 90, pp191-202, 2001

43. Wang, Z. L., and Kang, Z. C., Functional and Smart Materials: Structural Evolution and Structure Analysis, Plenum Press, New York, 1998

44. W.G. Cady, *piezoelectricity*, McGraw-Hill, New York; Revised Edition by Dover Publications, New York ,1964

45. Randeraat, J. van and Setterington, R. R., *Piezoelectric Ceramics*, second edition, Eindhoven : Philips Gloeilampenfahrieken, N.V., 1974

46. Jaffe, B. and Cook, W.R. , *Piezoelectric ceramics*, Academic Press, London and New York, 1971, Chapter 2, pp7-21

47. Ikeda, T., *Fundamentals of Piezoelectricity*, Oxford University Press, New York, 1990

48. *ANSYS Coupled-Field Analysis Guide*, Release 7.1, ANSYS Inc., 2003

49. *ANSI/IEEE Standard 176*, 1987

50. Polytec PI (Physik Instrumente), www.pi.ws

51. Morgan Advanced Ceramics, www.morgan-electroceramics.com

52. APC International, Ltd., www.americanpiezo.com

53. Sensor Technology Ltd., www.sensortech.ca

54. CATIA Version 5, Release 11 online documentation, Dassaut Systems, 1994 - 2003

55. Polytec PI, "Theory and Applications of Piezo Actuators and PZT NanoPositioning Systems"
http://www.physikinstrumente.com/tutorial/index.html

56. Howell, L.L. *Compliant Mechanisms,* New York, Wiley, 2001

57. Paros, J.M. and Weisbord, L. How to design flexure hinges. Machine Design, Vol.37, pp151–156, 1965,

58. King T, Xu W. The design and characteristics of piezomotors using flexure-hinged displacement amplifiers. Robotics and Autonomous Systems, Vol.19 , pp189–197, 1996

59. Lobontiu, N., Paine J. S.N. , Garcia, E., and Goldfarb, M. "Design of symmetric conic-section flexure hinges based on closed-form compliance equations", Mechanism and Machine Theory, Vol. 37, pp477–498, 2002

60. Associated Spring SPEC On–Line Catalog, www.assocspring.co.uk/spec/catalog/idxbelsprr.asp

61. MatWeb, Material Property Data, http://www.matweb.com/search/GetUnits.asp

62. ANSYS Advanced Analysis Techniques Guide, Release 7.1, ANSYS Inc., 2003

63. Norton, R.L., Machine Design: An Integrated Approach, second edition, Prentice-Hall, New Jersey,2000

Appendix A: **MATLAB code for conversion of published material data into the format needed for the ANSYS model**

```
% Transformation of BM532 (Sensor Technology ltd.)
% Curie temperature: 210 c
% Density 7650 kg/M^3
K33=3250  % Relative dielectric constants (relative permittivity), constant stress
K11=K33
E0=8.85*10^-12  % Permittivity of vacuum
d31=-250*10^-12 % Piezoelectric charge constant
d33=630*10^-12
d15=0
f=[0 0 0 0 0 d15;0 0 0 0 d15 0; d31 d31 d33 0 0 0]  %Piezoelectric constant matrix
d=f'   % f transposed
NUXY=0.34     % Poison's ratio
NUXZ=0.34
NUYZ=0.34
se11=14*10^-12     %Compliance constants, short circuit
se33=20*10^-12
Ye11=1/se11        % Elastic constants, short circuit
Ye33=1/se33
GXY=Ye11/(2*(1+NUXY))   % Shear elastic constants
GYZ=GXY
GXZ=GYZ
se44=1/GYZ
se12=-NUXY/Ye11
se13=-NUYZ/Ye33
se66=2*(se11-se12)
SE=[se11 se12 se13 0 0 0;se12 se11 se13 0 0 0;se13 se13 se33 0 0 0;0 0 0 se66 0 0;
   0 0 0 0 se44 0;0 0 0 0 0 se44]  % Compliance matrix
ef=f*inv(SE)    % e'(e transposed)
ET=E0*[K11,0,0;0 K11,0;0 0 K33] % dielectric matrix evaluated at constant stress, i.e.
mechanically free
CE=inv(SE) % stiffness matrix evaluated at constant electric field, i.e. short circuit
ES=ET-f*CE*d    %dielectric matrix evaluated at constant strain, i.e. mechanically
clamped
e=CE*d  %piezoelectric matrix relating stress/electric field
```

Appendix B: The Specification Of BM532 piezoelectric material

BM532

BM500 series ceramics are Lead Zirconate Titanates with high coupling coefficients and piezoelectric charge coefficient. These materials find application in passive devices and low power resonators.

BM532 is a modified version of ***BM500*** and has a higher capacitance per unit volume.

BM532			UNITS
Electrical[1]			
Relative Dielectric Constant	$K_{33}T$	3250	---
Dissipation Factor		2.0	%
Piezoelectric			
Coupling Factor	k_p	0.56	---
	k_{31}	0.34	---
	k_{33}	0.68	---
Charge Constant	d_{31}	-250	10^{-12}C/N
	d_{33}	630	10^{-12}C/N
Voltage Constant	g_{31}	-7.5	10^{-3}Vm/N
	g_{33}	20	10^{-3}Vm/N
Mechanical Quality Factor	Q_M	70	---
Frequency Constants[2]	N_P	2100	Hz.m
	N_1	1425	Hz.m
	N_3	1850	Hz.m
Elastic Modulus			
Compliance	S_{11}^E	14.0	$10^{-12}m^2/N$
	S_{33}^E	20.0	$10^{-12}m^2/N$
Density		7.65	g/cm^3
Curie Temperature	T_C	210	°C
Ageing Characteristics[3]			
Coupling Factor	k_p	-1.0	---
Dielectric Constant	K_{33T}	-1.0	---
Frequency Constant	N_p	1.0	Hz.m

1. Low field parameters; measured at 1 kHz

Appendix C: Piezoelectric Linear Actuator Drawing

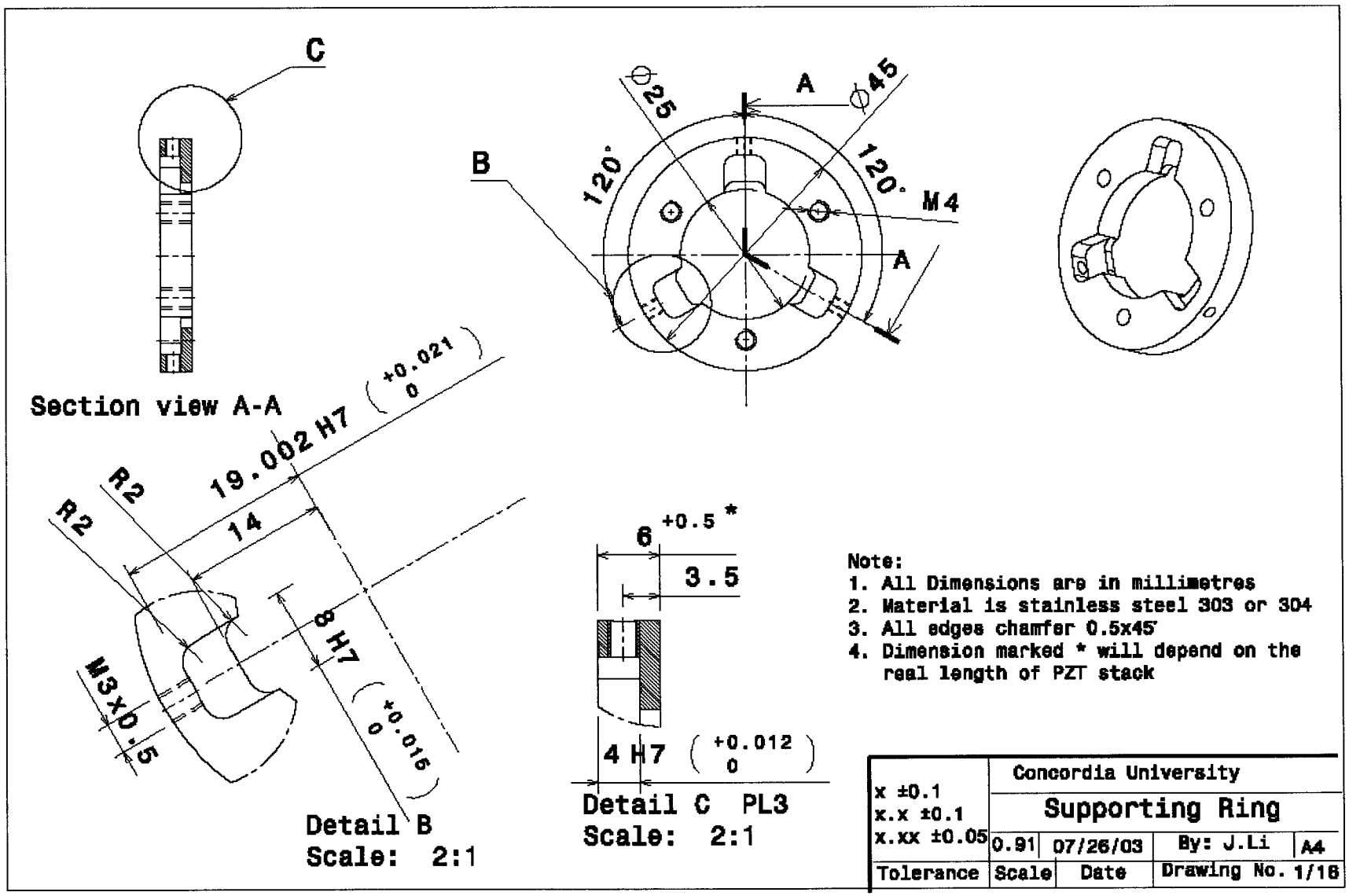

Appendix C: Piezoelectric Linear Actuator Drawing

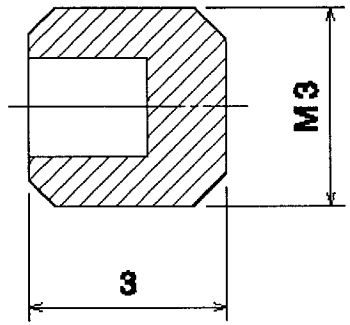

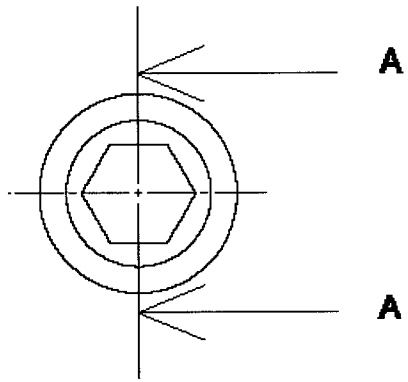

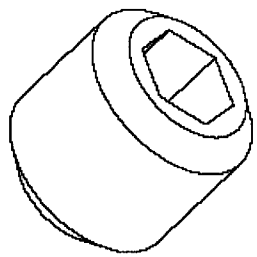

Note:

1 ISO_4026_M3x3_GRADE_A_STEEL_HEX_SOCKET_SET_SCREW _WITH_FLAT_POINT

2 Quantity is 12

Isometric view
Scale: 10:1

	Concordia University			
	Adjust screw			
	9	07/26/03	By: J.Li	A4
Tolerance	Scale	Date	Drawing No. 2/18	

Appendix C: Piezoelectric Linear Actuator Drawing

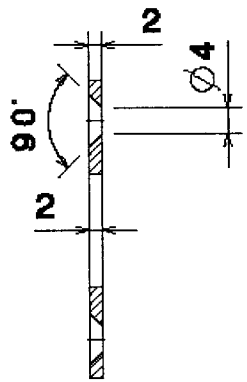

Section view A-A

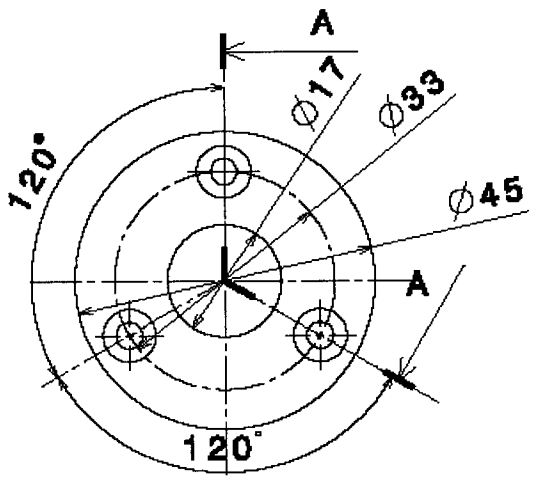

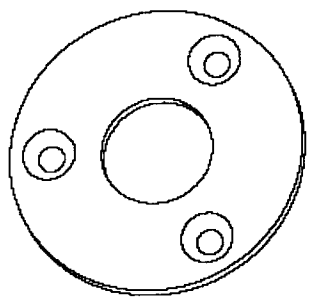

Note:
1. All Dimensions are in millimetres
2. Material is Stainless steel 303 or 304

x ±0.1 x.x ±0.1 x.xx ±0.05	Concordia University			
	cover			
	0.9	07/26/03	By: J.Li	A4
Tolerance	Scale	Date	Drawing No	3/18

Appendix C: Piezoelectric Linear Actuator Drawing

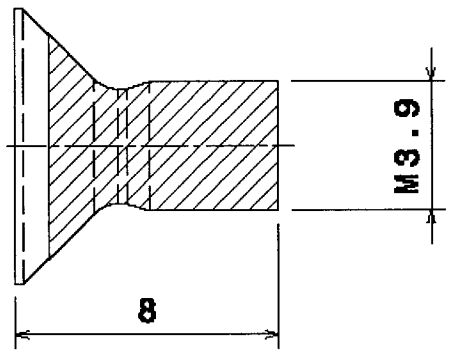

Section view A-A
Scale: 5:1

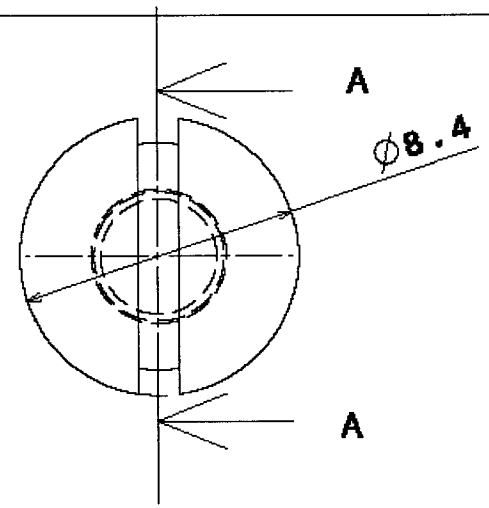

Front view
Scale: 5:1

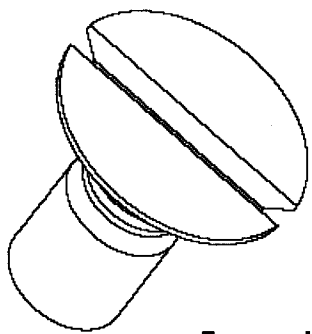

Isometric view
Scale: 5:1

Note:
1 ISO_2009_M4x6_STEEL_GRADE_A_COUNTERSUNK _SLOTTED_FLAT_HEAD_SCREW

2 Quantity is 12

	Concordia University			
	Flat head screw			
		07/26/03	By: J.Li	A4
Tolerance	Scale	Date	Drawing No.	4/18

Appendix C: Piezoelectric Linear Actuator Drawing

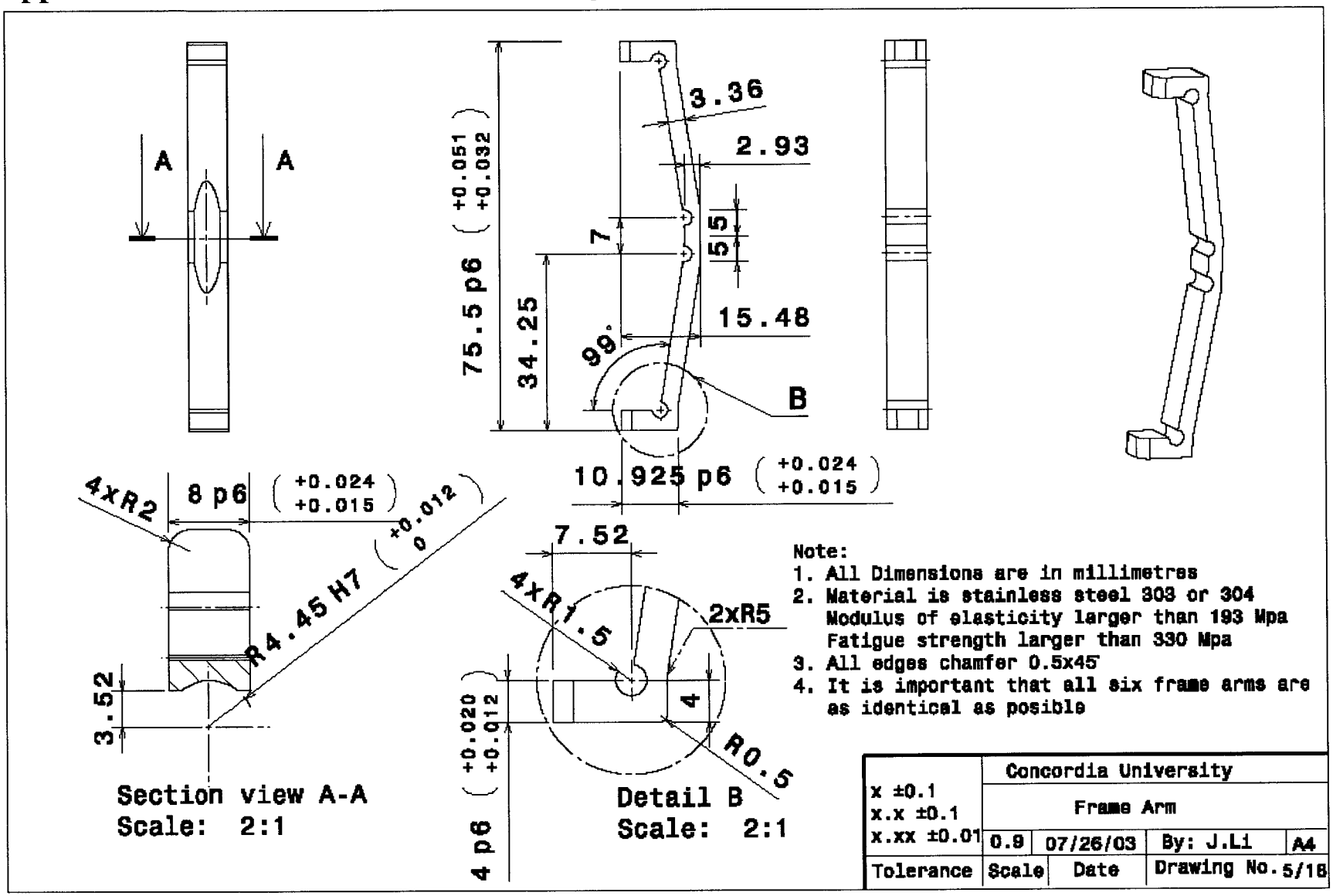

Appendix C: Piezoelectric Linear Actuator Drawing

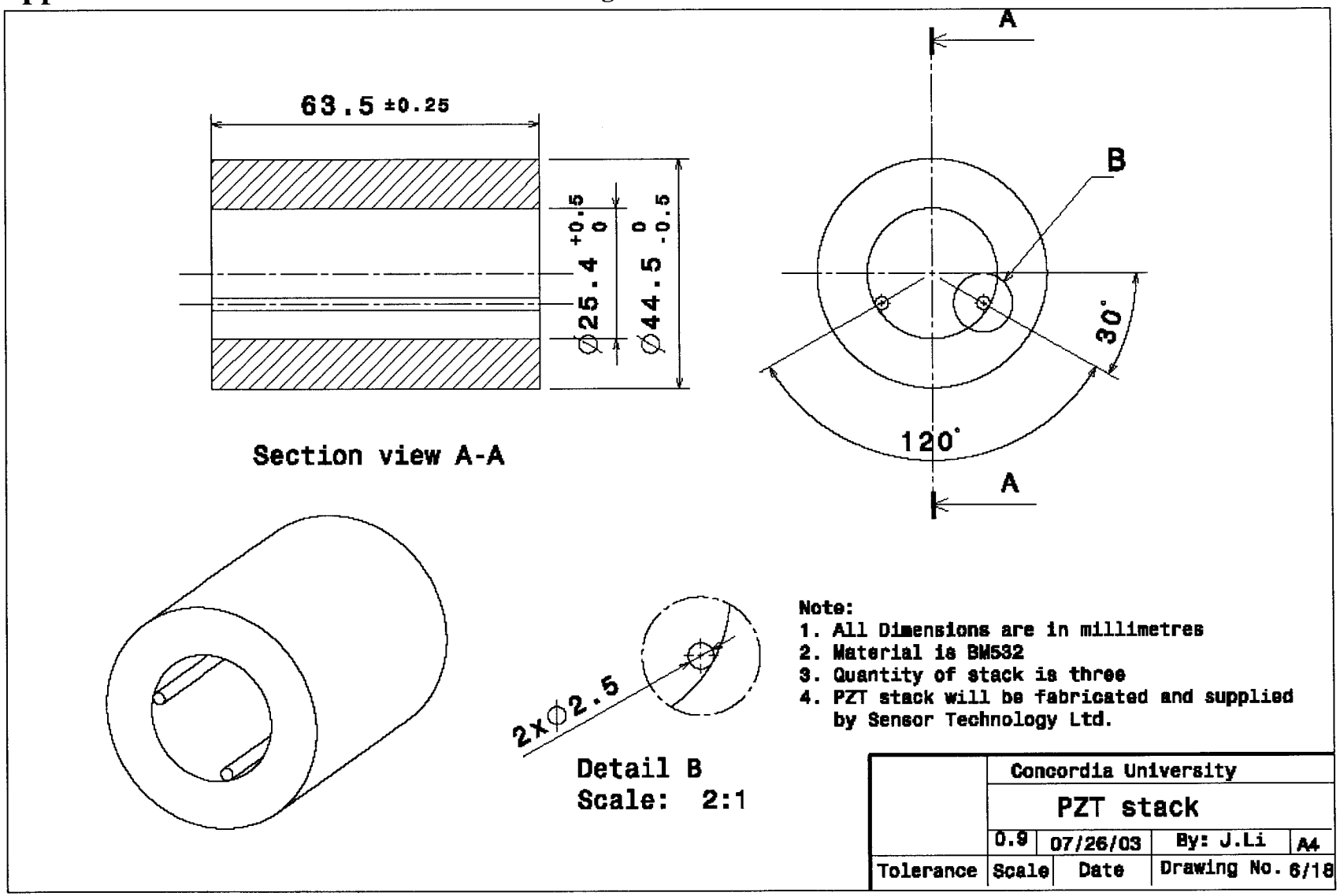

Appendix C: Piezoelectric Linear Actuator Drawing

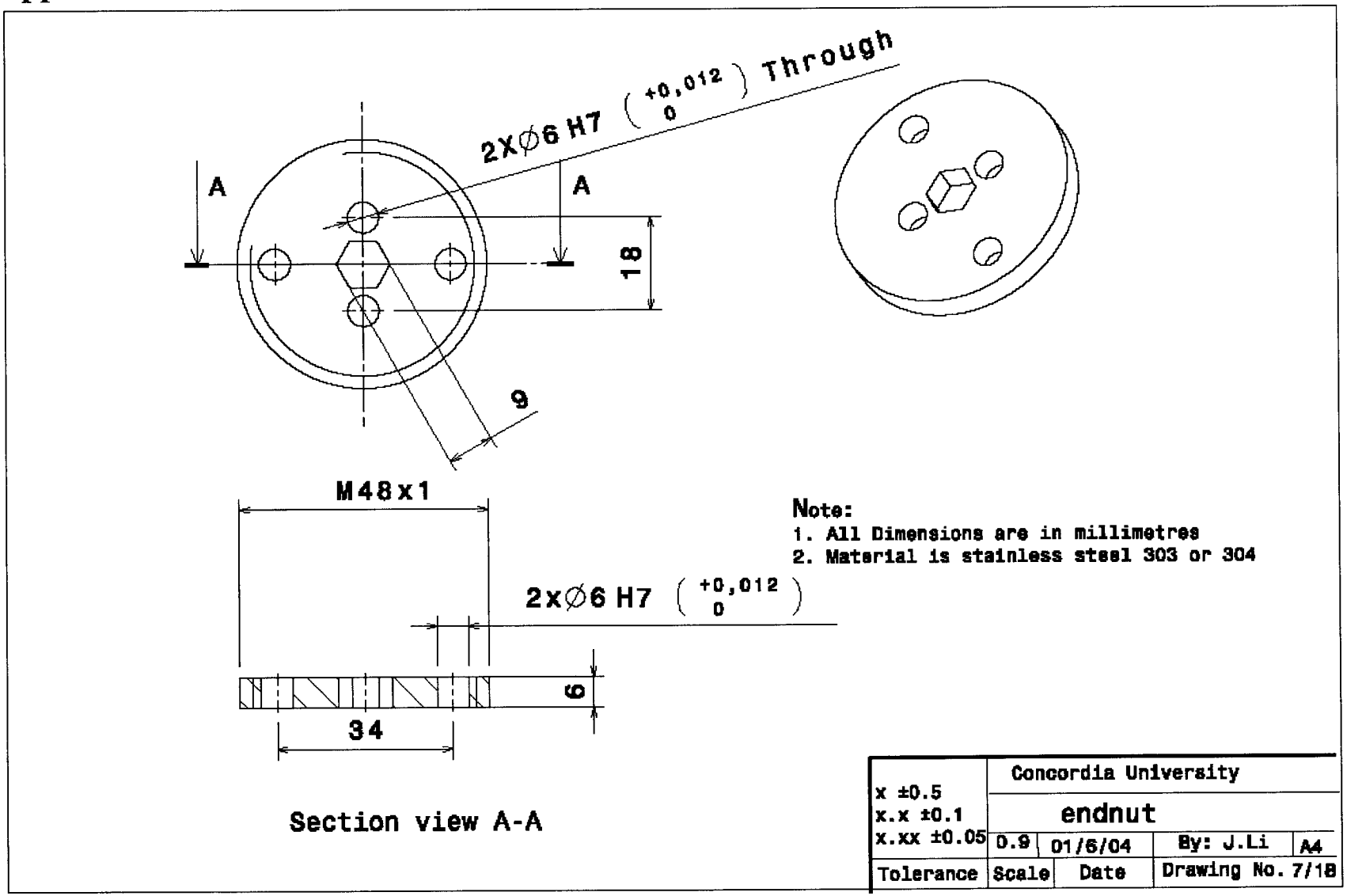

Appendix C: Piezoelectric Linear Actuator Drawing

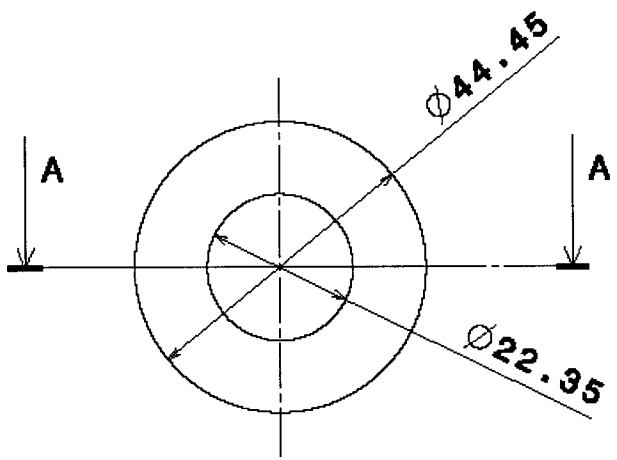

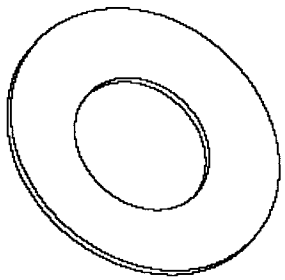

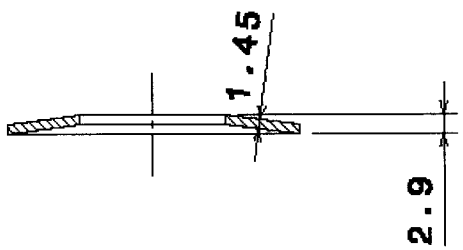

Section view A-A

Note:
1. All Dimensions are in millimetres
2. Material is spring steel
3. Quantity is twelve
4. Belleville spring washers are supplied by SPEC. The catalog number is B1750-057

x ±0.2 x.x ±0.2	Concordia University			
	Belleville Spring Washer			
	0.9	01/26/04	By: J.Li	A4
Tolerance	Scale	Date	Drawing No. 8/18	

Appendix C: Piezoelectric Linear Actuator Drawing

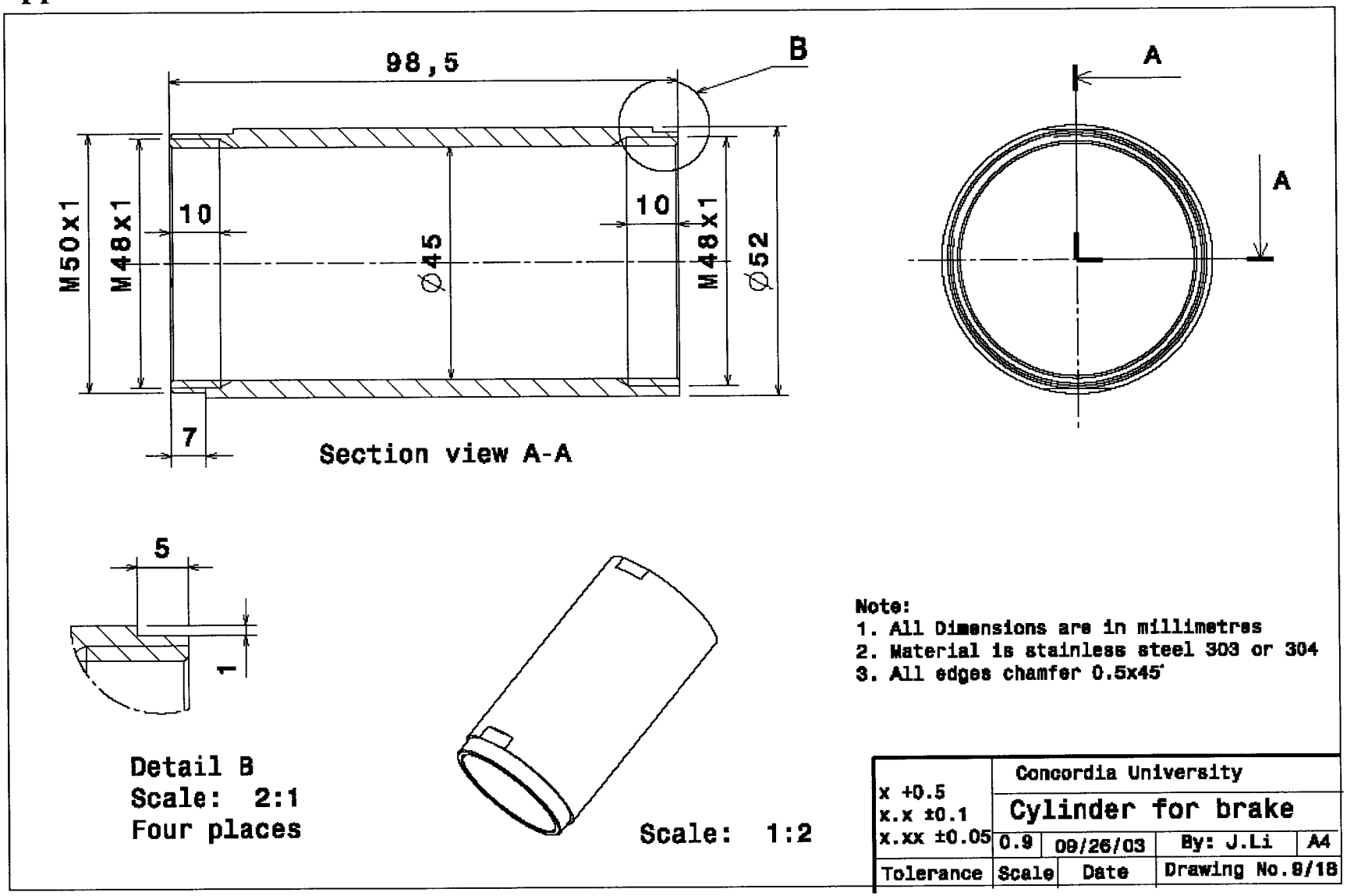

Appendix C: Piezoelectric Linear Actuator Drawing

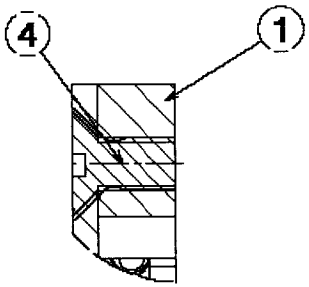

Detail B
Scale: 2:1

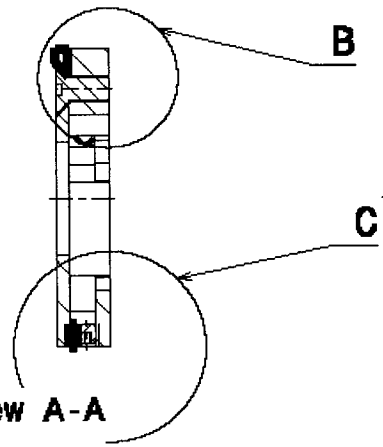

Section view A-A
Scale: 1:1

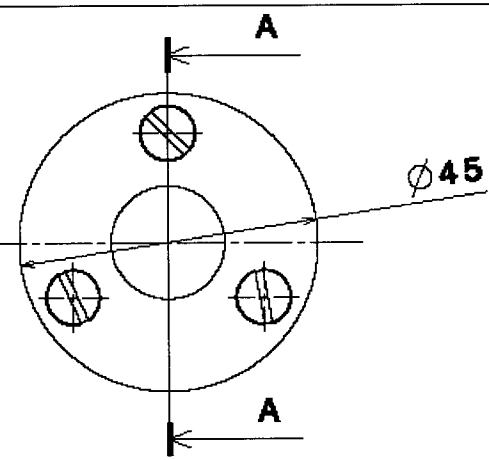

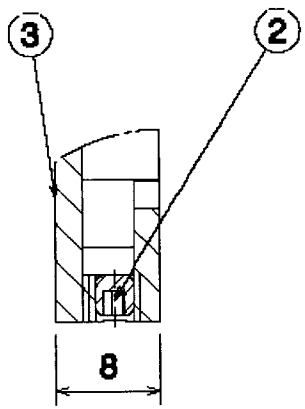

Detail C
Scale: 2:1

Bill of Material: Support ring assembly

Number	Part Name	Type	Quantity
1	supporting ring	Part	1
2	ISO_4026_M3x3_GRADE_A_STEEL_HEX_SOCKET_SET_SCREW_WITH_FLAT_POINT	Part	3
3	cover	Part	1
4	ISO_2009_M4x6_STEEL_GRADE_A_COUNTERSUNK_SLOTTED_FLAT_HEAD_SCREW	Part	3

Note:
1. All Dimensions are in millimetres
2. Quantity of assembly is 4

	Concordia University			
	Support ring assembly			
	0.9	07/26/03	By: J.Li	A4
Tolerance	Scale	Date	Drawing No.	10/18

Appendix C: Piezoelectric Linear Actuator Drawing

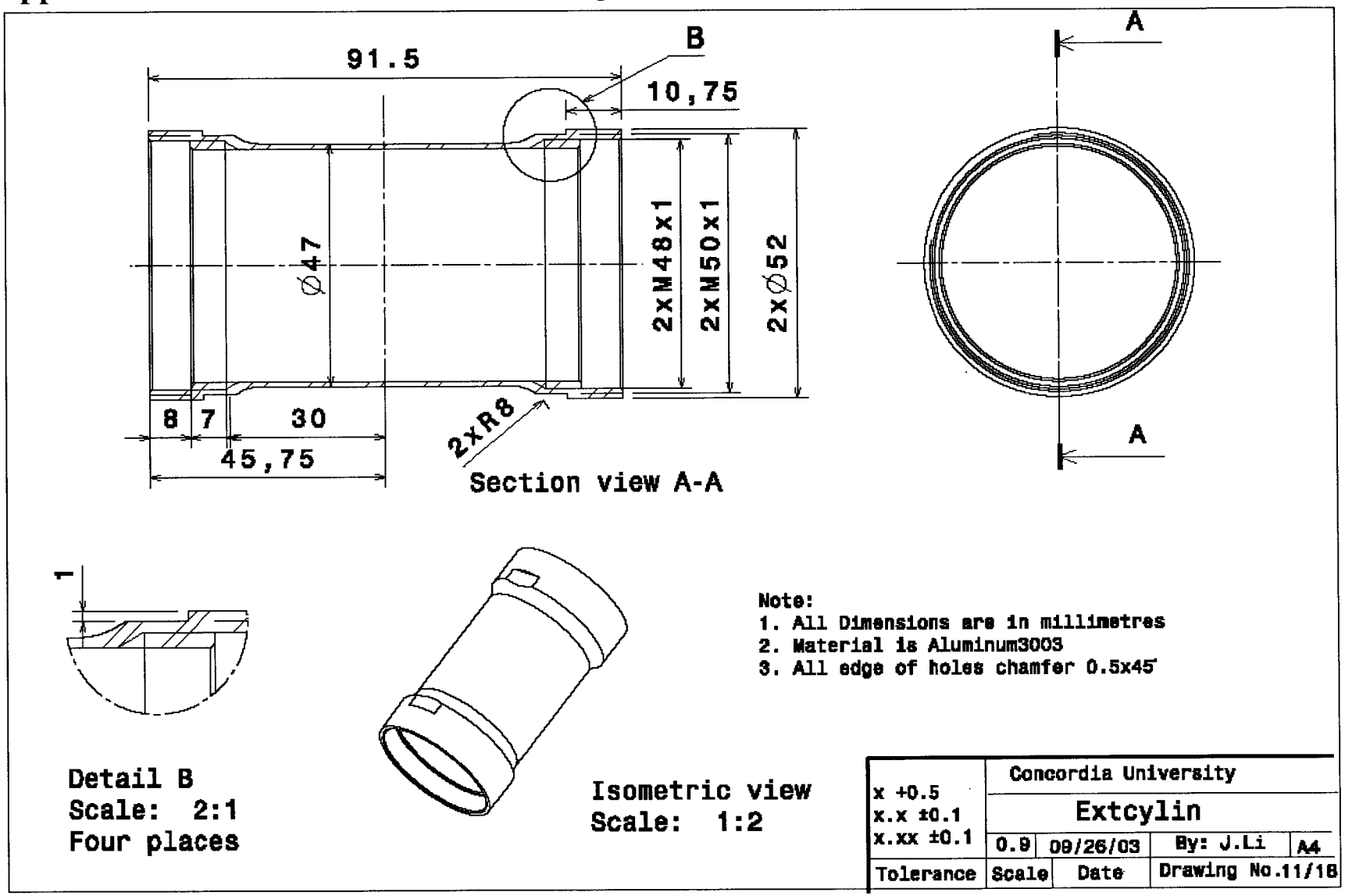

Appendix C: Piezoelectric Linear Actuator Drawing

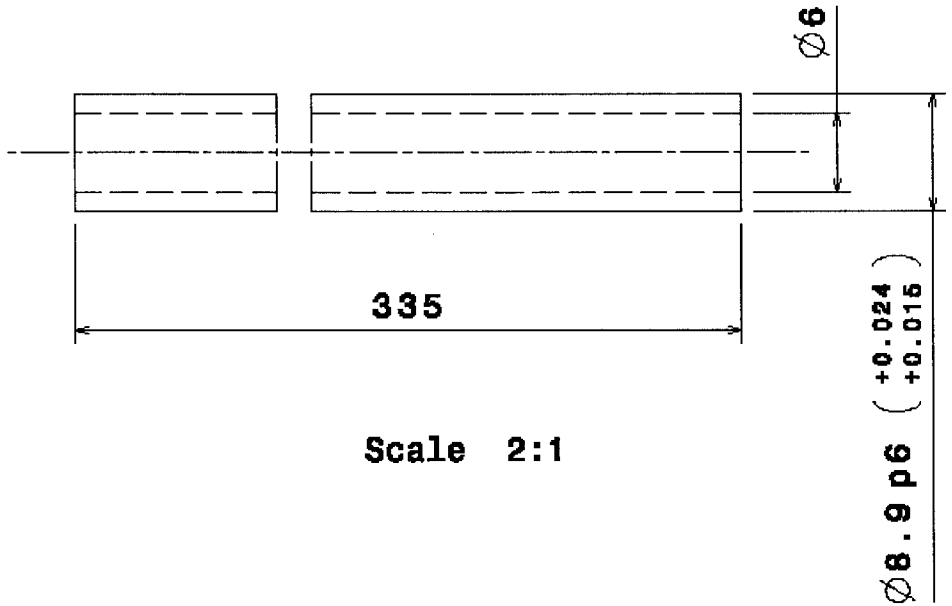

Scale 2:1

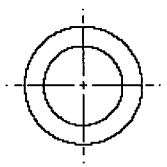

Scale 2:1

Note:
1. All Dimensions are in millimetres
2. Material is stainless steel 304
3. All edge fillet radius 0.2 except defined
4. Tolerance of tube is required only in the 70 mm length from each end
   In the middle part of tube, the tolerance is free

	Concordia University			
	Shaft			
	0.9	07/26/03	By: J.Li	A4
Tolerance	Scale	Date	Drawing No.12/18	

Appendix C: Piezoelectric Linear Actuator Drawing

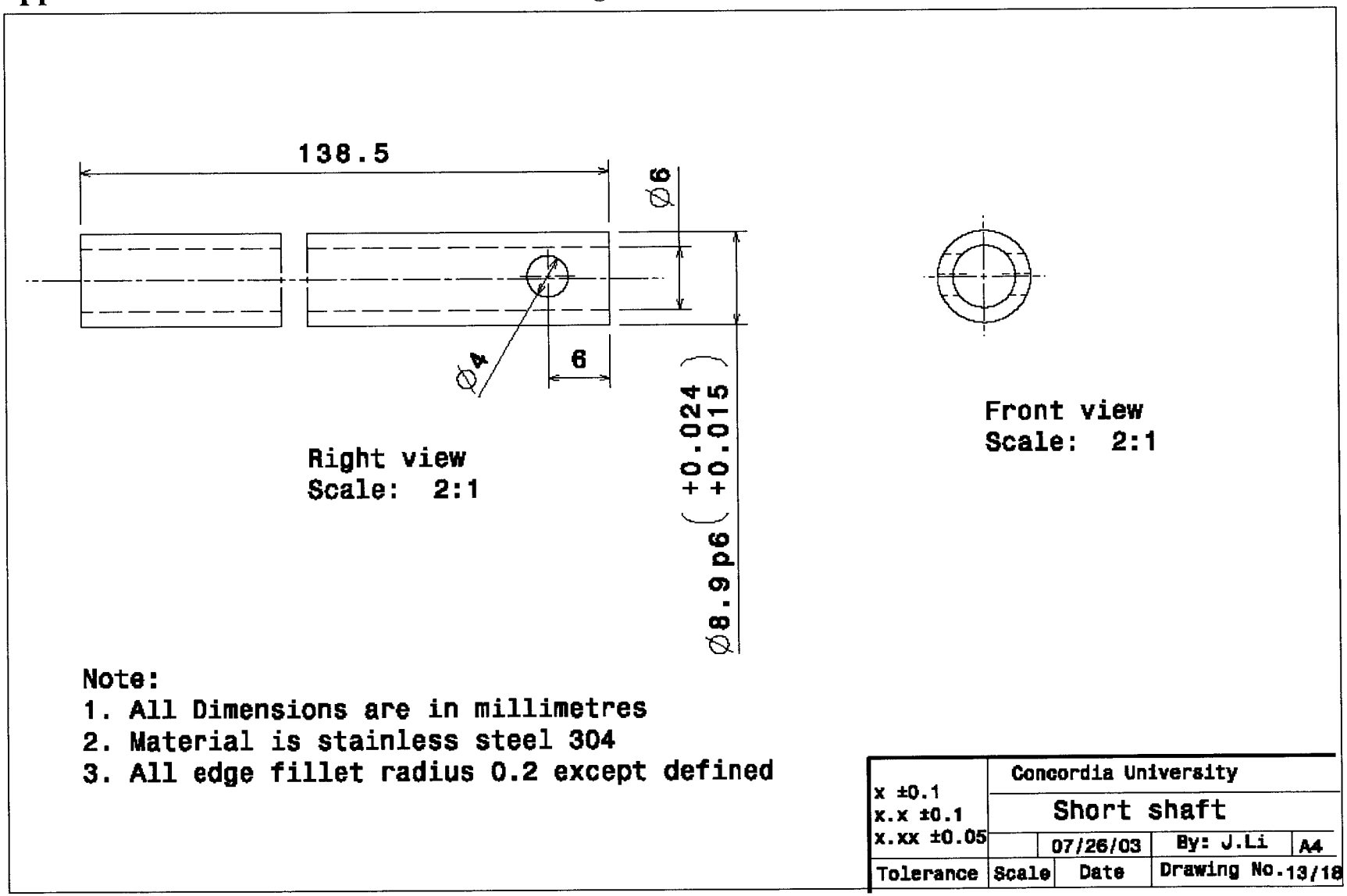

Appendix C: Piezoelectric Linear Actuator Drawing

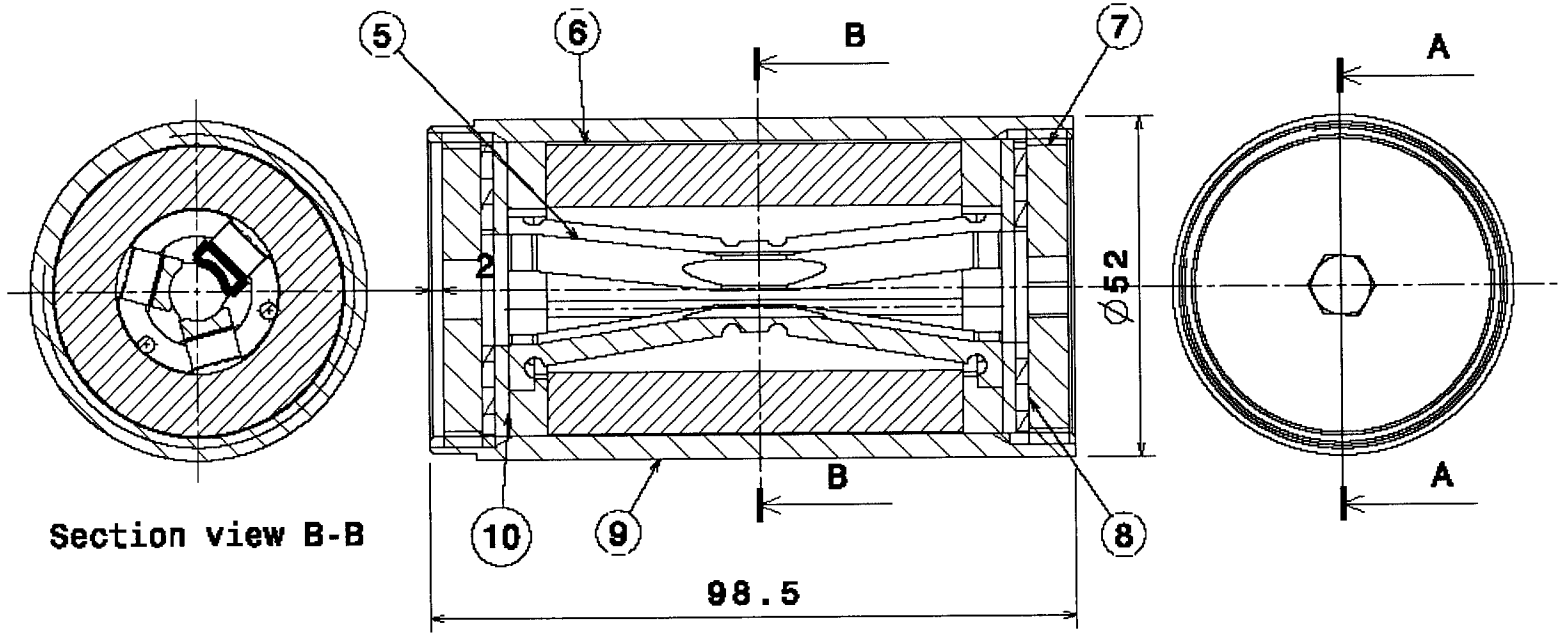

Bill of Material: Brake Assembly

Number	Part Name	Type	Quantity
10	supporting ring assembly	Assembly	2
5	frame arm	Part	3
6	PZTstack	Part	1
7	endnut	Part	2
8	spring washer	Part	2
9	cylinderbrake	Part	1

Note:
All dimensions are in millimeters

x ±0.1 x.x ±0.1 x.xx ±0.05	Concordia University			
	BrakeAssembly			
	0.9	07/26/03	By: J.Li	A4
Tolerance	Scale	Date	Drawing No.14/18	

Appendix C: Piezoelectric Linear Actuator Drawing

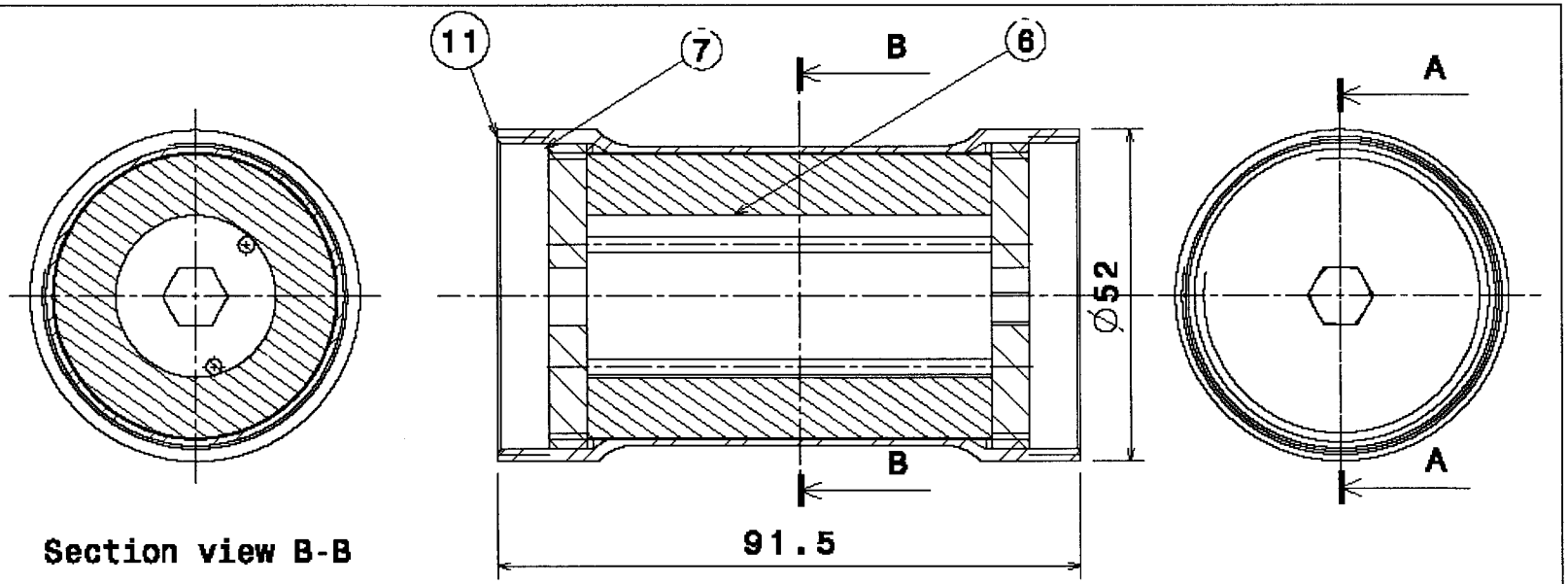

Note:
All dimensions are in millimetres

Number	Part Number	Type	Quantity
11	extcylin	part	1
7	end nut	part	2
6	PZTstack	part	1

Concordia University			
Extension assembly			
0.9	07/26/03	By: J.Li	A4
Scale	Date	Drawing No.15/18	

Appendix C: Piezoelectric Linear Actuator Drawing

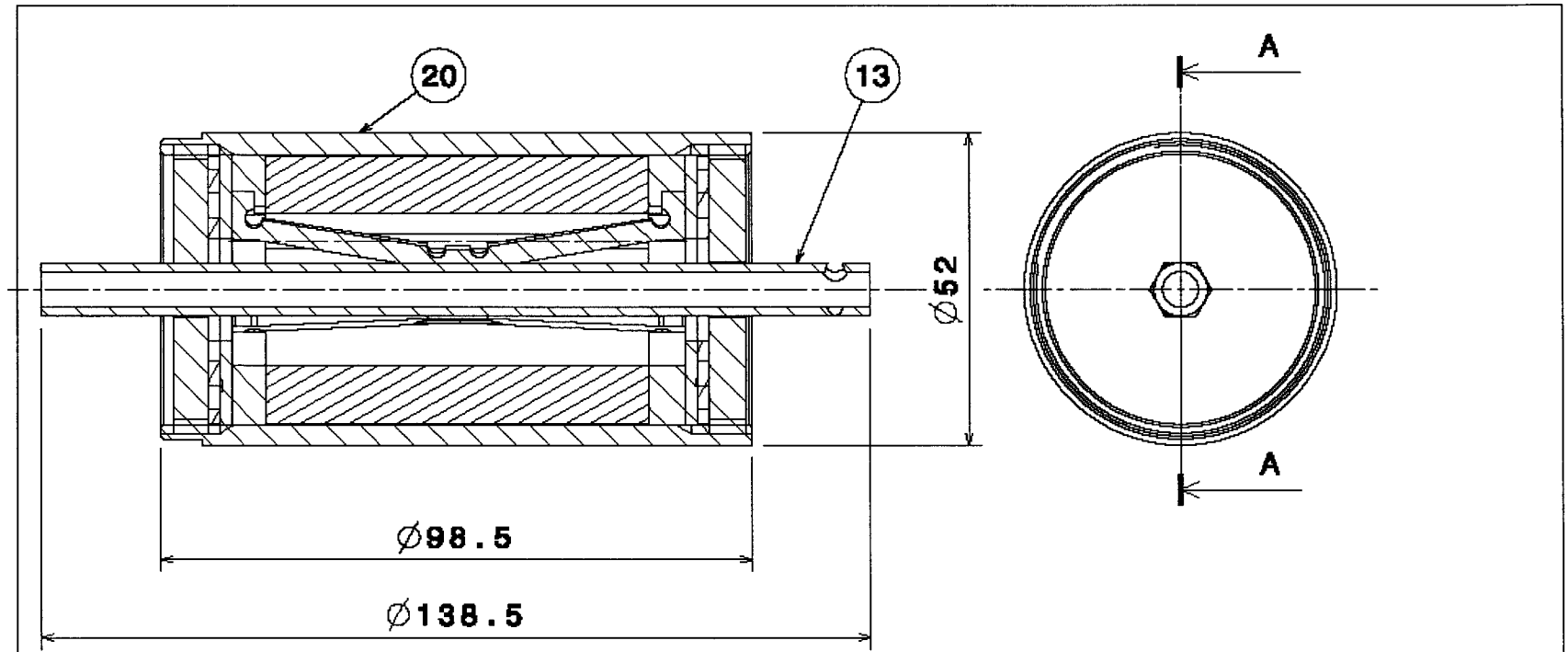

Section view A-A
Scale: 1:1

Note:
All dimensions are in millimeters

Bill of Material: brakecalibration

Number	Part Number	Type	Quantity
20	brakeA	Assembly	1
13	shortshaft	Part	1

	Concordia University			
	Brake calibration			
	0.9	07/26/03	By: J.Li	A4
Tolerance	Scale	Date	Drawing No.	16/18

Appendix C: Piezoelectric Linear Actuator Drawing

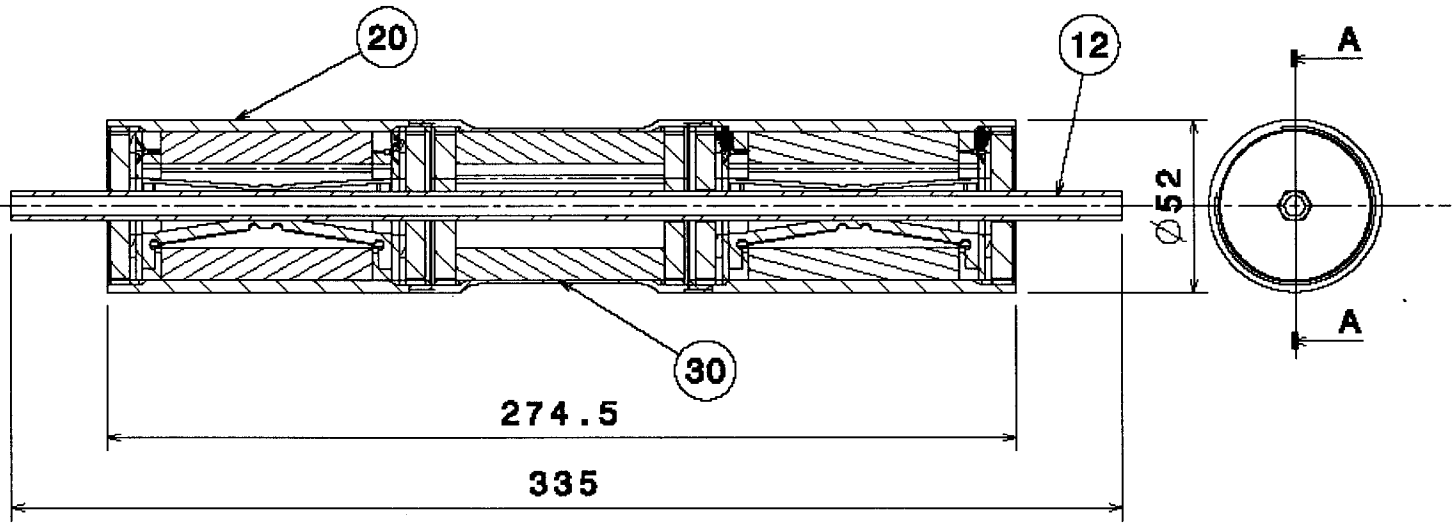

Section view A-A

Note:
All dimensions are in millimetres

Bill of Material: actuator

Number	Part Number	Type	Quantity
20	BrakeAssembly	Assembly	2
30	ExtenAssembly	Assembly	1
12	Shaft	Part	1

x ±0.1 x.x ±0.1 x.xx ±0.05	Concordia University			
	Actuator assembly			
	0.9	07/26/03	By: J.Li	A4
Tolerance	Scale	Date	Drawing No.17/18	

Appendix C: Piezoelectric Linear Actuator Drawing

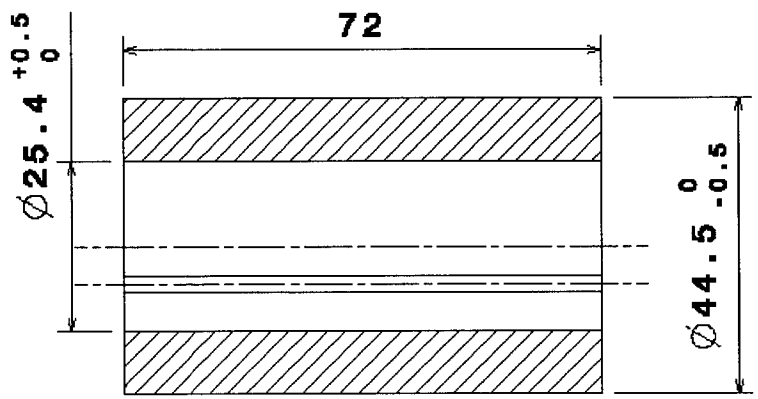

Section view A-A

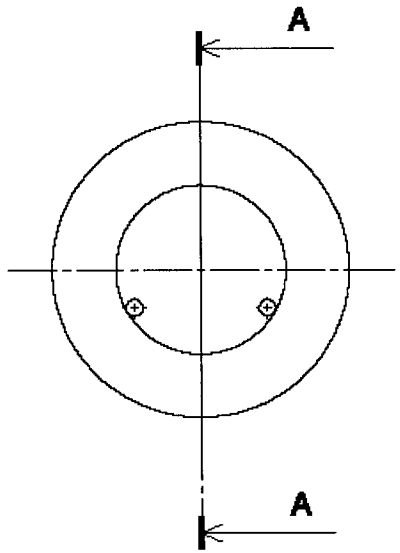

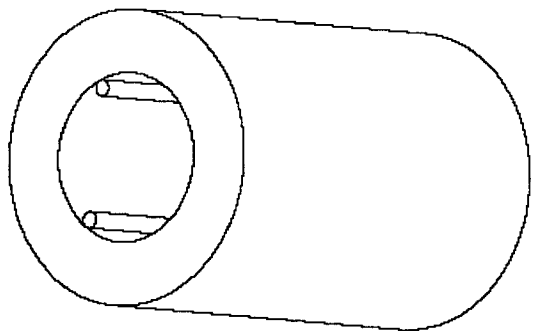

Note:

1. All Dimensions are in millimetres
2. Material is BM532
3. Quantity of stack is one
   (revised from Drawing No. 4)
4. PZT stack will be fabricated and supplied by Sensor Technology Ltd.

	Concordia University			
	PZT extension stack			
	0.9	03/27/04	By: J.Li	A4
Tolerance	Scale	Date	Drawing No. 18/18	

Appendix D: Characterization Of Tubal BM532 PZT Stacks

Sensor Technology Limited
SENSOR
P O Box 97, 20 Stewart Road
Collingwood, Ontario, Canada L9Y 3Z4
E-Mail:Techsupport@sensortech.ca
World Wide Web: www.sensortech.ca
Tel: 705.444.1440
Fax: 705.444.6787

Characterization of First Ring Stack for Concordia University

Dec 17, 2003

1. Zero-load displacement

Zero-load displacement was measured as a function of voltage using a LVDT. The results are shown in Figure 1. The average slope which is equal to (Maximum - Minimum Displacement)/(Voltage range) was 86.5 nm/V.

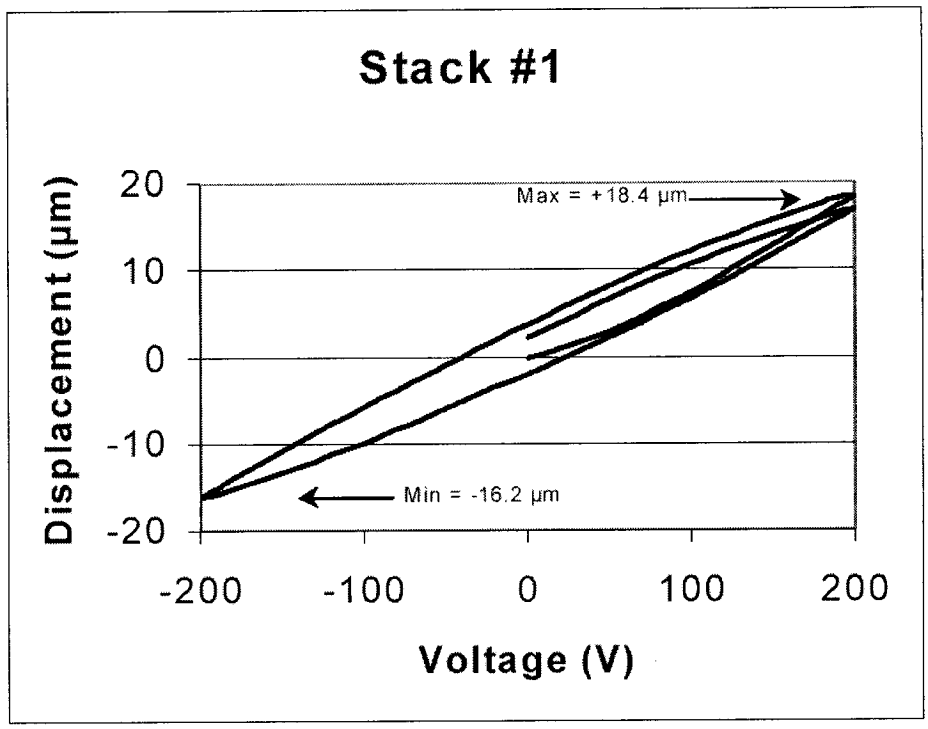

Figure 1. Voltage vs. displacement measured using LVDT

Appendix D: Characterization Of Tubal BM532 PZT Stacks

Sensor Technology Limited
SENSOR
P O Box 97, 20 Stewart Road
Collingwood, Ontario, Canada L9Y 3Z4
E-Mail:Techsupport@sensortech.ca
World Wide Web: www.sensortech.ca
Tel: 705.444.1440
Fax: 705.444.6787

2. Blocked Force Measurement

Blocked force was measured using the apparatus shown in Fig. 2.

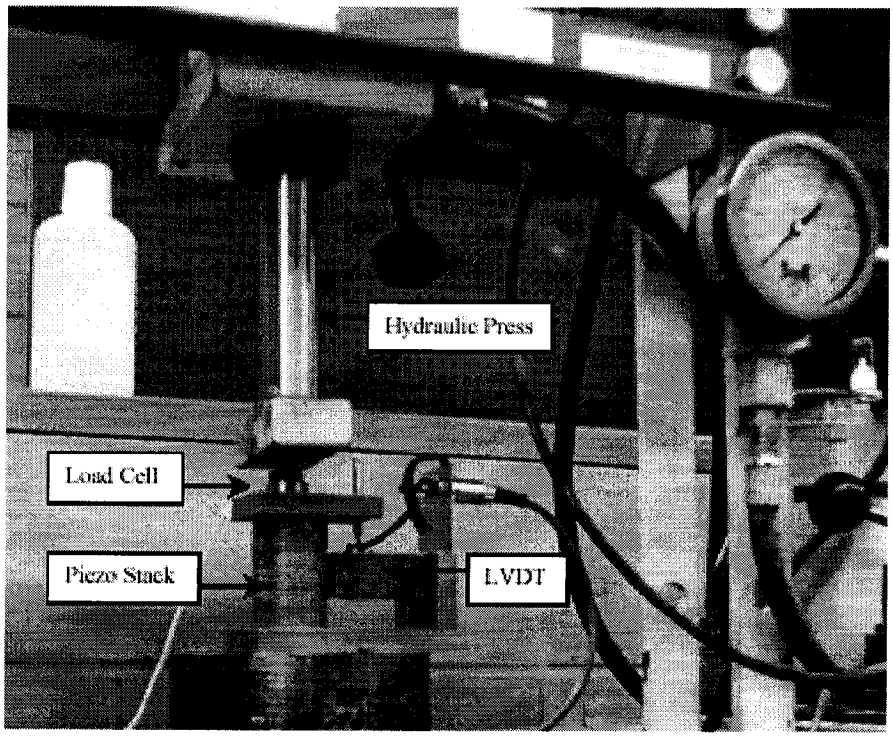

Figure 2. Apparatus used for measuring blocked force.

Two different approaches were used to measure the blocked force. In the first approach the short circuit Young's modulus was measured by shorting the stack terminals and measuring the compression vs. force characteristic. These results are shown in Fig. 3. The characteristic was approximately linear and hysteresis-free, except for points near zero force where there was an initial region of low stiffness. The stiffness in the linear region was 0.25 N/nm. Converting to Young's modulus using area = 0.001049 m^2 and stack height H = 0.0635 m, gives the result Y_{33}^{E} = 1.5E10 N/m^2. This is smaller than the value expected for the ceramic alone (5E10 N/m^2) and suggests that there was a significant contribution from the shims and epoxy layers.

Appendix D: **Characterization Of Tubal BM532 PZT Stacks**

Sensor Technology Limited
SENSOR
P O Box 97, 20 Stewart Road
Collingwood, Ontario, Canada L9Y 3Z4
E-Mail:Techsupport@sensortech.ca
World Wide Web: www.sensortech.ca
Tel: 705.444.1440
Fax: 705.444.6787

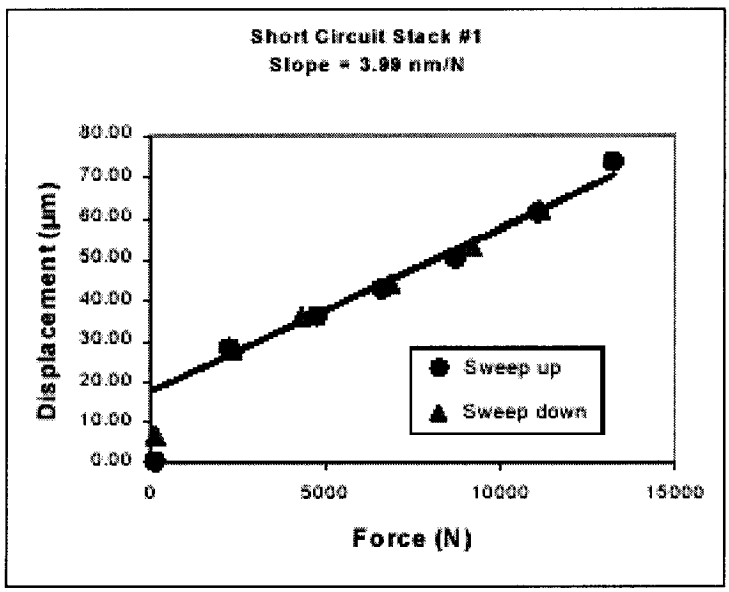

Figure 3. Compression vs. applied force measured under short circuit conditions.

The blocked force (BF) is related to the zero-load displacement (ΔH) by (1):

$$BF = \Delta H * Y_D^E * \frac{Area}{H} \qquad (1)$$

Using an average displacement of 17.3 µm at 200 V gives a blocked force at 200 V of 4.3 kN.

The second measurement approach was to subject the stack to a prestress at zero voltage (various values between 50 and 1300 kg were used) and record the zero-voltage LVDT reading (proportional to stack compression). 200 V was then applied causing stack expansion and a change in LVDT reading. The increase in force required to return the LVDT to its original reading was then measured. This is the blocked force. The values obtained in this way showed significant variation that was likely connected with hysteresis in the displacement vs. voltage characteristics (Fig. 1). However the values were in the vicinity of and bracketed the above noted 4.3 kN value. In one case 3.8 kN blocked force was measured with 3.6 kN prestress and in another, 5.1 kN was measured with 4.6 kN prestress. Because of the hysteresis-related variations we believe that the first measurement approach, which gave 4.3 kN @ 200 V, is the most reliable technique. Prestress is needed to reach the linear region of the Fig. 3 characteristic and ensure the largest possible blocked force.

Appendix D: Characterization Of Tubal BM532 PZT Stacks

Sensor Technology Limited
SENSOR
P O Box 97, 20 Stewart Road
Collingwood, Ontario, Canada L9Y 3Z4
E-Mail:Techsupport@sensortech.ca
World Wide Web: www.sensortech.ca
Tel: 705.444.1440
Fax: 705.444.6787

3. Stack Appearance

The stack height specification was achieved by adding two unmetallized ceramics on top and bottom and then grinding the flat surfaces to obtain the desired total height and flatness. However in this process it was found that to achieve the desired height and flatness, one of the inactive ceramics was ground completely through on the left side of the stack while a thin remnant remained on the other half. This leaves an nonuniform surface appearance on one of the ends even though the surface is smooth and flat. This is a purely cosmetic effect which can be removed in future stacks by using only single inactive elements of greater thickness on the two ends.

4. Reference

1. C. Near, "Piezoelectric actuator technology", SPIE vol 2717 p. 246 (1996).

Appendix D: Characterization Of Tubal BM532 PZT Stacks

Sensor Technology Limited
SENSOR
P O Box 97, 20 Stewart Road
Collingwood, Ontario, Canada L9Y 3Z4
E-Mail:Techsupport@sensortech.ca
World Wide Web: www.sensortech.ca
Tel: 705.444.1440
Fax: 705.444.6787

Characterization of Second Ring Stack for Concordia University

March 26, 2004

WO # 03271, Part # SJ14-00-1WSH-00

1. Zero-load displacement

Zero-load displacement was measured as a function of voltage using a LVDT. The results are shown in Figure 1. The average slope which is equal to (Maximum - Minimum Displacement)/(Voltage range) was 76.5 nm/V.

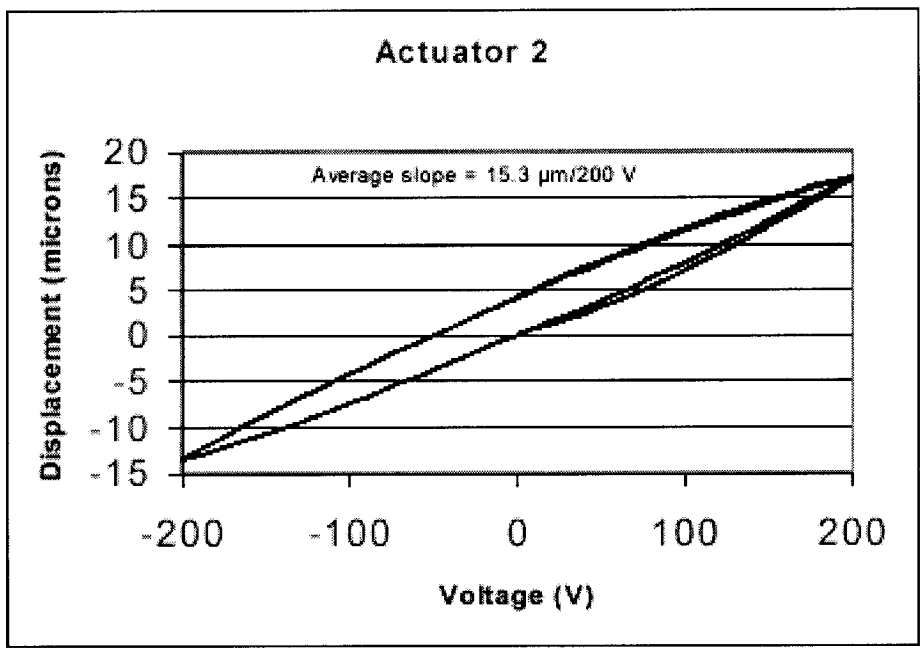

Figure 1. Voltage vs. displacement measured using LVDT

Appendix D: **Characterization Of Tubal BM532 PZT Stacks**

2. Blocked force measurement:

Two different approaches were used to measure the blocked force. In the first approach the short circuit Young's modulus was measured by shorting the stack terminals and measuring the compression vs. force characteristic. These results are shown in Fig. 3. The characteristic was approximately linear and hysteresis-free, except for points near zero force where there was an initial region of low stiffness. The stiffness in the linear region was 0.15 N/nm. Converting to Young's modulus using area = 0.001049 m^2 and stack height H = 0.0635 m, gives the result Y_{33}^E = 9.0E9 N/m^2. This is smaller than the value expected for the ceramic alone (5E10 N/m^2) and suggests that there was a significant contribution from the shims and epoxy layers.

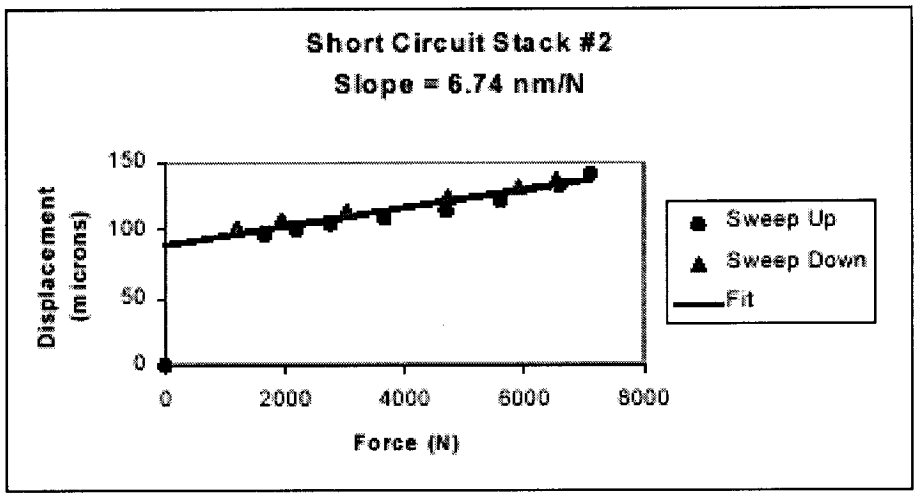

Figure 3. Compression vs. applied force measured under short circuit conditions.

The blocked force (BF) is related to the zero-load displacement (ΔH) by (1):

$$BF = \Delta H * Y_{33}^E * \frac{Area}{H} \qquad (1)$$

Using an average displacement of 15.3 μm at 200 V gives a blocked force at 200 V of 2.3 kN.

The second measurement approach was to subject the stack to a prestress at zero voltage and record the zero-voltage LVDT reading (proportional to stack compression). 200 V was then applied causing stack expansion and a change in LVDT reading. The increase in force required to return the LVDT to its original reading was then measured. This is the blocked force. The values obtained in this way showed significant variation that was likely connected with hysteresis in the displacement vs. voltage characteristics, and for this reason the measurement obtained by the short circuit method above is considered more reliable. Nevertheless the values were in the vicinity of the above noted 2.3 kN value. In one case 1.6 kN blocked force was measured with 0.9 kN prestress and in another, 2.0 kN was measured with 2.1 kN prestress.

Appendix D: **Characterization Of Tubal BM532 PZT Stacks**

Sensor Technology Limited
SENSOR
P O Box 97, 20 Stewart Road
Collingwood, Ontario, Canada L9Y 3Z4
E-Mail:Techsupport@sensortech.ca
World Wide Web: www.sensortech.ca
Tel: 705.444.1440
Fax: 705.444.6787

Characterization of Third Ring Stack for Concordia University

April 5, 2004

WO # 03271, Part # SJ14-00-1WSH-00

1. Zero-load displacement

Zero-load displacement was measured as a function of voltage using a LVDT. The results are shown in Figure 1. The average slope which is equal to (Maximum - Minimum Displacement)/(Voltage range) was 71.6 nm/V.

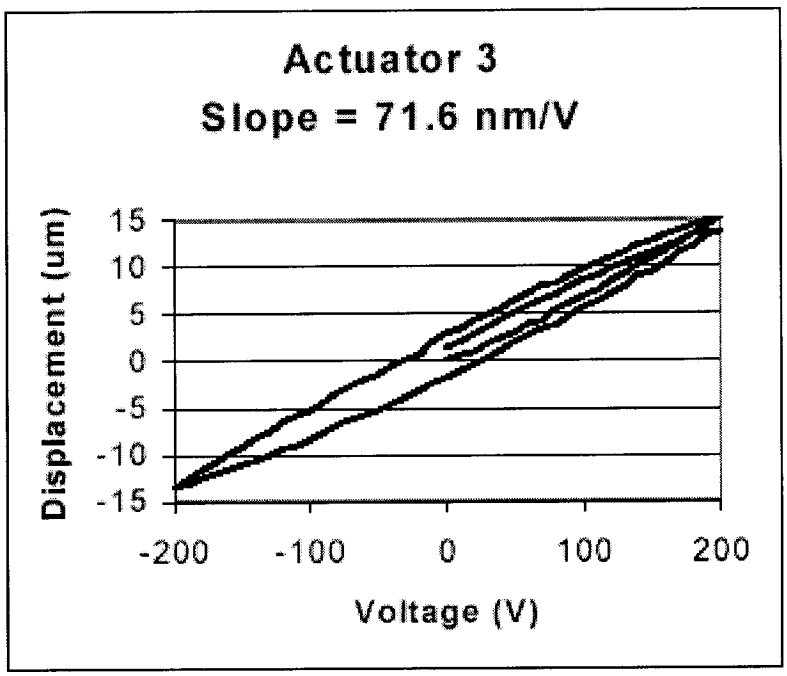

Figure 1. Voltage vs. displacement measured using LVDT

Appendix D: Characterization Of Tubal BM532 PZT Stacks

2. Blocked force measurement:

To determine the blocked force the short circuit Young's modulus was first measured by shorting the stack terminals and measuring the compression vs. force characteristic. These results are shown in Fig. 3. The characteristic was approximately linear and hysteresis-free. The stiffness was 0.23 N/nm. Converting to Young's modulus using area = 0.001049 m^2 and stack height H = 0.072 m, gives the result Y_{33}^{E} = 1.6E10 N/m^2. Note that this calculation uses a larger value of H, since the customer had requested that this stack, which is to be used as the extender actuator in an inchworm motor, be made with 72 mm height.

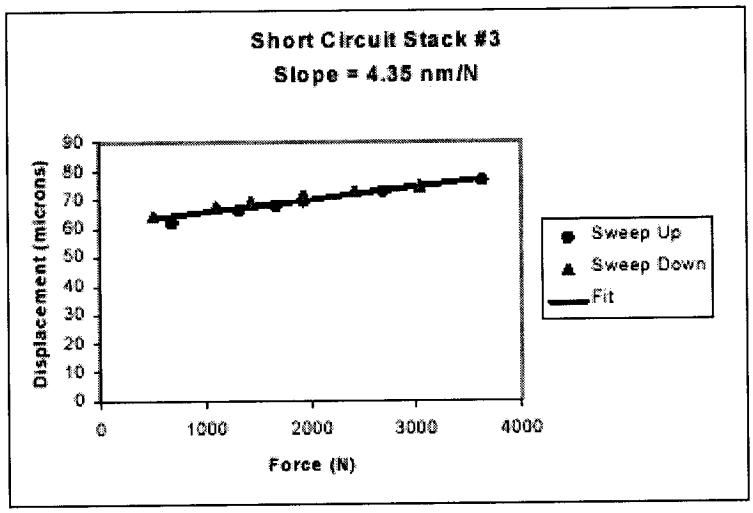

Figure 3.
Compression vs. applied force measured under short circuit conditions.

The blocked force (BF) is related to the zero-load displacement (ΔH) by (1):

$$BF = \Delta H * Y_{33}^{E} * \frac{Area}{H} \qquad (1)$$

Using an average displacement of 14.3 μm at 200 V gives a blocked force at 200 V of 3.3 kN.

Capacitance and Dissipation Summary for The Three Stack Actuators

Stack Actuator	Capacitance (μF)	Dissipation Factor
1	4.4	0.024
2	4.4	0.029
3	4.9	0.015